



**UNIVERSITÀ POLITECNICA DELLE MARCHE**  
**FACOLTÀ DI INGEGNERIA**

---

Corso di Laurea Magistrale in:  
Ingegneria meccanica - Sistemi produttivi e tecnologie  
innovative

**Calibrazione di un sensore a  
triangolazione di linea laser per il  
controllo qualità in linea**

-

**Calibration of a laser line triangulation  
sensor for in-line quality control**

Relatore:  
**Nicola Paone**

Tesi di Laurea di:  
**Guerino Gianfranco Paolini**

A.A. 2022/2023



# Contents

<b>1</b>	<b>Sommario</b>	<b>1</b>
<b>2</b>	<b>Introduction</b>	<b>2</b>
2.1	<i>Project and Objectives</i>	2
2.2	<i>What is a laser line triangulation sensor</i>	4
2.3	<i>Statistic instruments and calibration theory</i>	7
2.3.1	Normal distribution of Gauss	7
2.3.2	Measurement system and calibration	8
2.3.3	Uncertainty of the instrument	9
<b>3</b>	<b>Laser line triangulation system</b>	<b>11</b>
3.1	<i>Laser</i>	11
3.1.1	Initial setup	12
3.2	<i>Camera Characteristics</i>	13
3.2.1	How CMOS sensors work	13
3.2.2	Multi Slope Mode	15
3.2.3	Setting of the camera parameters	16
3.2.4	Subpixel	17
3.2.5	Sensor mode for laser line profile extraction	17
3.2.6	Data Conversion	19
3.3	<i>Lenses and Focus</i>	21
3.4	<i>How to evaluate performance of chosen parameters</i>	23
<b>4</b>	<b>Calibration</b>	<b>24</b>
4.1	<i>Calibration state of art</i>	24
4.2	<i>Zigzag calibration target</i>	26
4.2.1	Geometrical measurement and data analysis of calibration target	27
4.3	<i>Alignment of the laser triangulation sensor</i>	28
4.4	<i>Performing experiments</i>	31
4.4.1	Polynomial model	31
4.4.2	Testing	38
4.5	<i>Effect of FOV – how to establish the number of teeth acquired</i>	40
4.6	<i>Calibration target issues – spatial sampling frequency</i>	42
4.6.1	First solution adopted	43
4.6.2	Second solution: using intersections	45
4.7	<i>Parametric study on the parameter ProfilesPerFrame</i>	50
<b>5</b>	<b>Results</b>	<b>51</b>
<b>6</b>	<b>Further improvements</b>	<b>54</b>
6.1	<i>Improvement N° 1</i>	54
6.2	<i>Improvement N° 2</i>	55
<b>7</b>	<b>Conclusions</b>	<b>56</b>

<b>8</b>	<b>Index of figures.....</b>	<b>57</b>
<b>9</b>	<b>Index of tables.....</b>	<b>60</b>
<b>10</b>	<b>References.....</b>	<b>61</b>

# 1 Sommario

L'obiettivo di questo progetto è misurare la rettilineità delle barre d'acciaio all'ingresso della linea di produzione dell'azienda VDLWEW che dopo vari processi di piegatura a caldo diventano delle sospensioni a braccio longitudinale per mezzi pesanti.

Il tutto è stato svolto per un progetto europeo, openZDM (Zero Defects Manufacturing) che mira ad ottenere il controllo qualità per il 100% dei prodotti, compresi quelli in entrata (come nel caso in questione) e quelli in uscita. Il controllo qualità verrà effettuato tramite un robot industriale che afferra la barra e la punta davanti al sensore a triangolazione laser che stiamo costruendo, tipicamente utilizzato per i sistemi di controllo qualità.

Il sensore a triangolazione laser avendo a che fare con l'ottica porta con se problemi che sono presenti anche nella fotografia classica come ad esempio la messa a fuoco della scena.

Poi avendo a che fare con il laser e con una configurazione particolare presentano altri problemi:

- messa a fuoco e instabilità di posizione della sorgente laser;
- proprietà della superficie dell'oggetto come rumore dato dalla rugosità, riflessi e altri difetti;
- valutazione del segnale (equazioni non lineari);
- condizioni ambientali.

Questi sono problemi nell'ottenere una corretta calibrazione, soprattutto se le lunghezze da misurare sono dell'ordine del metro. La sfida è stata eseguire misurazioni della rettilineità ad una grande distanza di lavoro con un grande fondoscala (entrambi di 1 m): solitamente le accuratezze a una distanza di lavoro di 1 m sono superiori a 1 mm.

I requisiti necessari per una corretta misurazione sono:

- misurare la rettilineità delle barre fino a 0,2 mm;
- campo di misura della lunghezza maggiore di 1 m.

Per soddisfare i requisiti dobbiamo:

- misurare il target di calibrazione con la CMM;
- allineare correttamente il calibratore;
- eseguire più misure contemporaneamente per ridurre la deviazione standard sulla media, senza aumentare troppo il tempo per prendere una decisione (prodotto conforme o non conforme);
- utilizzare i migliori parametri ottici e della camera.

Con questa tesi viene sviluppato un metodo per ottenere una corretta calibrazione ed i risultati finali sono stati i seguenti:

- deviazione standard sull'asse X = 0,022 mm;
- valore massimo dei residui nell'asse X = 0,125 mm;
- deviazione standard nell'asse Z = 0,031 mm;
- valore massimo dei residui nell'asse Z = 0,158 mm.

Infine vengono suggeriti dei miglioramenti per aumentare le prestazioni del sensore.

Considerando l'incertezza espansa come due volte la deviazione standard, otteniamo uno strumento che, seguendo la normativa UNI ISO/TR 14253-6:2017, riesce a misurare efficacemente la non rettilineità delle barre con una risoluzione di 0,3 mm.

## 2 Introduction

### 2.1 PROJECT AND OBJECTIVES

This work is developed in the context of the European project openZDM, the acronym ZDM stands for Zero Defects Manufacturing, which aims to achieve quality control of 100% of products, including incoming products (as in the work of this thesis) and outgoing products.

The VDLWEW company produces air suspensions for trucks and buses; in this project, we address the production of the trailing arm which is shown in Figure 2-1.



Figure 2-1. Trailing-arm suspension produced by VDLWEW [20].

The process begins with the use of a prismatic-shaped steel bar which is bent at high temperatures in several sequential steps, which deform it until it assumes the final shape as shown in Figure 2-2.

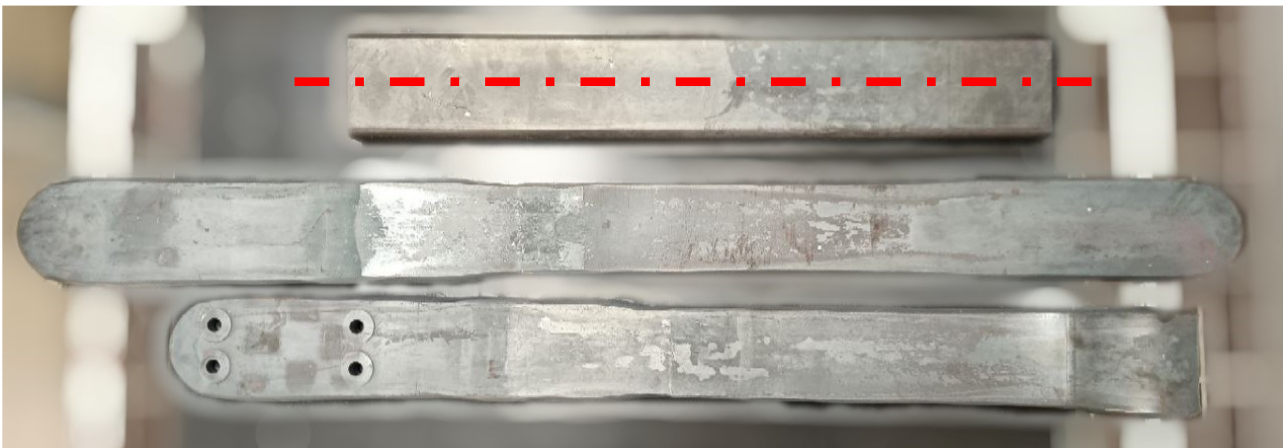


Figure 2-2. A prismatic-shaped bar is placed at the top of the image with its longitudinal axis in red. The bars present under the first are obtained after intermediate bending steps before obtaining the final suspension in Figure 2-1.

There is a problem if the prismatic-shaped bar is already bent at the entrance of the production process: in this case, the bar travels along the entire production line and, after a series of hot forming processes, reaches the end of the production line, but its shape is not in agreement with specifications, becoming a waste because it is a non-conforming product.

In this case, the company pays the costs of the material and all costs related to the process and waste (in the worst case pays warranty costs).

This problem can be avoided by performing quality control at the entrance of the production line.

Citing the ISO 9001, as shown in Figure 2-3, to get quality control we need to ensure quality in each process: "The process approach involves the systematic definition and management of processes, and

their interactions, so as to achieve the intended results in accordance with the quality policy and strategic direction of the organization”.

So, the initial interaction of the product with the production line is certainly a key process to keep under control.

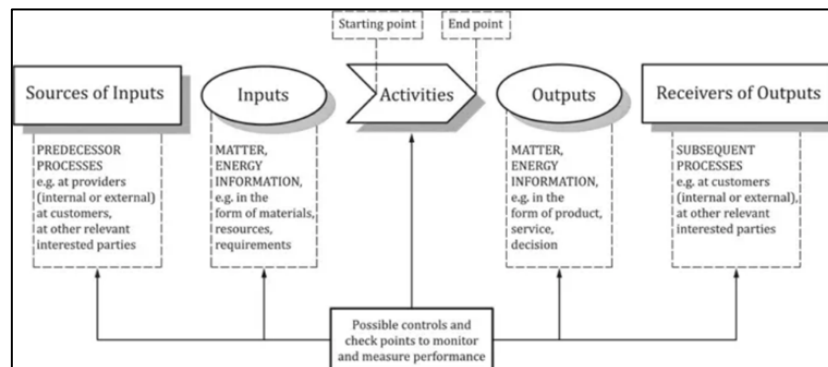


Figure 2-3. Schematic representation of the elements of a single process from ISO 9001 [21].

The objective of this project is to measure the straightness of steel bars at the beginning of the production line.

To perform straightness measures in the line production we need a quality control station that works as described below:

- prismatic shaped bars arrive on a pallet,
- an industrial robot grabs the bar thanks to a magnetic gripper,
- then the robot places the bar in front of a sensor in charge of measuring straightness,
- after the straightness measurement is performed, the bar is put on the conveyor and enters the induction furnace.

Requirements for the sensor that should ensure quality in this step are:

- measure the straightness of bars down to 0.2 mm;
- measure products about 1 m long.

It has been chosen the laser line triangulation technology to measure the straightness of the bar. The main reasons for that choice are:

- it is a non-contact measurement system; therefore, it minimizes interference with the production,
- it is a highly accurate and low-uncertainty sensor,
- it can be designed to withstand harsh environmental industrial conditions,
- it is typically used for quality control systems [7,8],

However, the requirements of this specific application are particularly challenging. It is required to resolve deviation of straightness down to 0.2 mm over a measurement range very large equal to 1000 mm. Moreover, straightness should be measured before the bar enters the induction furnace and after the induction furnace; in this case, the environment is particularly challenging in terms of high temperatures and the presence of dust.

## 2.2 WHAT IS A LASER LINE TRIANGULATION SENSOR

A scheme of how the sensor usually is built is shown in Figure 2-4.

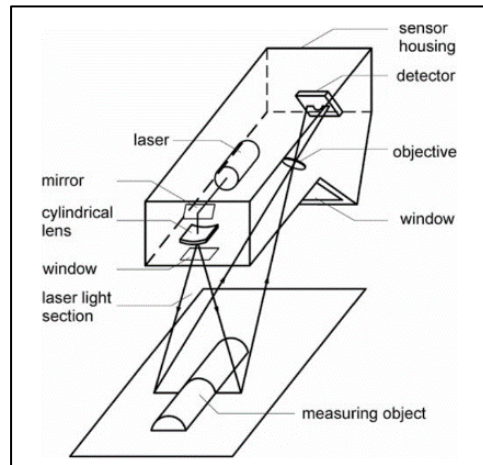


Figure 2-4. Laser line triangulation scheme [7].

A laser line is projected on the object. A camera, mounted with its optical axis inclined with respect to the axis of the laser, detects an image of the laser line; a bandpass optical filter is used to image only the laser line. The image that the sensor capture therefore contains only the laser line. If the target is flat, the line will be straight, if the target is not flat, the line will be deformed.

Referring to Figure 2-5, **this sensor is based on a non-linear principle:**

$$z = \frac{ah'}{b \sin \theta - h' \cos \theta}$$

where:

- $z$  denotes the movement of the surface along the laser axis;
- $h'$ , similarly, denotes the movement of the surface along the vertical axis of the camera sensor;
- $a$  is the distance between the optical axis of the lenses and the incident point;
- $b$  is the distance from the receiving lens behind the main surface to the center of the imaging surface
- $\theta$  denotes the mutual angle between the light plane and the camera's optical axis, which is also known as the triangulation angle [34].

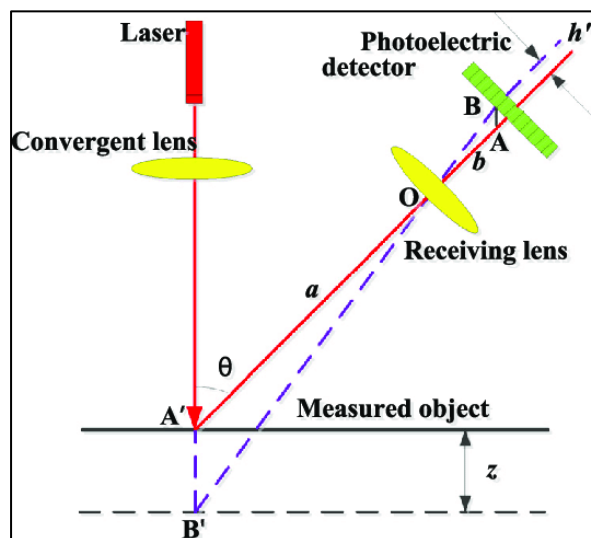


Figure 2-5. Scheme to obtain 1 dimensional measurement [34].

In a laser line triangulation sensor, there are problems related to the lenses (the same problems as in common photography) that are:



- diffraction, which produces a limit of spatial resolution  $r$  due to the diameter of the lens  $D$ , the focal distance  $f$  and the wavelength  $\lambda$  of the light source (Raylight criterion) [26]

$$r = 1.22\lambda \frac{f}{D};$$

- pincushion (or fish-eye) and barrel distortions [23,24] as shown in Figure 2-6;

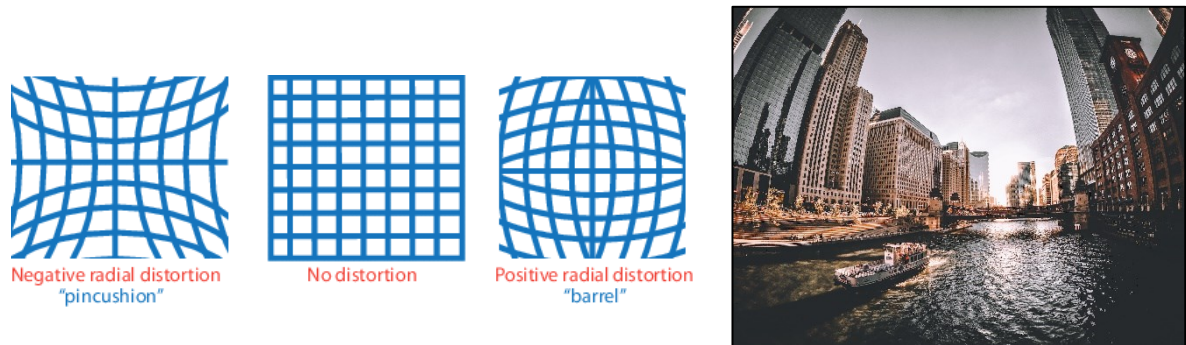


Figure 2-6. Difference between pincushion and barrel distortion on the left [23]. Example of barrel distortion on right, from <https://help.shopmoment.com/article/181-superfish-distortion-correction> [24].

- depth of focus, which defines the tolerance distance around the object such that it is sufficiently in focus (Figure 2-7) which depends on the aperture (usually called F# number).

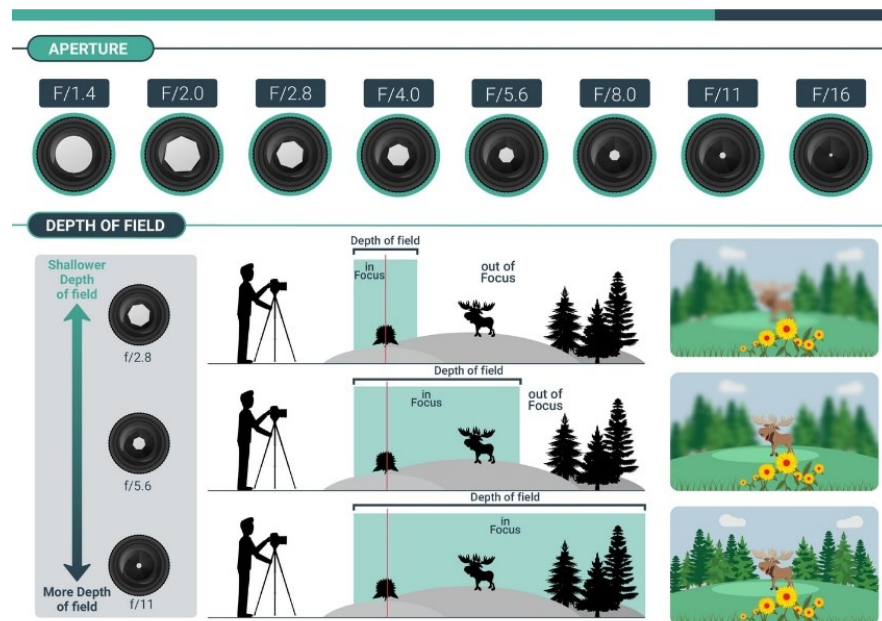


Figure 2-7. Differences in depth of field vs. aperture.

However, laser triangulation sensors present other specific problems:

- focus [9] and laser source line instability [10]; there are methods to correct the laser instability Patrick Kienle et. al. [6] explained, but we want to obtain results using the instruments available in the lab;
- optical properties of the object surface like speckle noise [11], reflections [12] and other defects [13];
- aberrations [14,15];
- signal evaluation (non-linear equations);
- environmental conditions [7].

Consequently, these are problems in achieving the best performance, especially if the lengths to be measured are of the order of 1 m. An accurate calibration is therefore necessary.

To satisfy the requirements set by the application, UNIVPM developed a laser line triangulation system shown in Figure 2-8, which is built with a structure made of a carbon fiber tube to realize a stable and stiff sensor and to reduce the effect of thermal expansion.

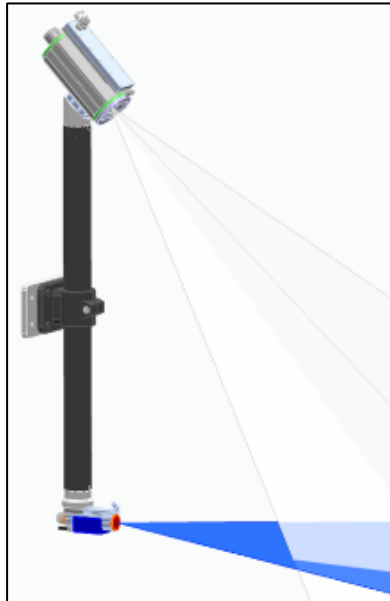


Figure 2-8. Final configuration of the sensor.

With this configuration the domain range becomes the one shown in Figure 2-9.

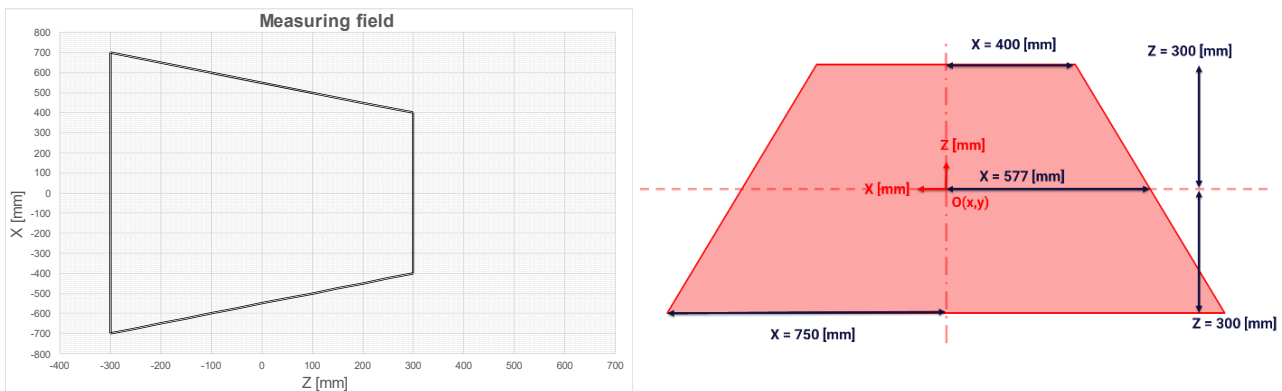


Figure 2-9. Measuring field of designed sensor.  $O(x,y) = (0,0)$  represent the origin of measurement coordinate system.

In the next chapter, Laser line triangulation system, we will describe laser, camera and optics in detail.

As said before, the challenge in this case is to perform straightness measurements over a steel bar 1 m long, with a resolution down to 0.2 mm. The sensor should be positioned at a 1 m working distance from the bar, which is a parameter set during the design of the sensor (design performed before the work carried out for this thesis).

Usually, state of art shows accuracies at 1 m working distance are equal to 1.5 mm [6] for this class of sensors.

In this thesis is developed and executed a method to perform proper calibration for the sensor proposed.

The main steps of the calibration procedure developed are:

- select and build an artifact having known geometry to be used as a reference target for calibration;
- measure the calibration target with the CMM (Coordinate-measuring machine) in order to know its actual geometry;
- align the target correctly [16] in front of the laser triangulation sensor;

- move the target to known positions across the measurement field;
- for each position, perform repeated measurements and apply averaging to reduce the standard deviation on the mean [17], without increasing too much time of evaluation (conforming or nonconforming product);
- use the best optical and camera parameters [7].

In the next section, Statistic instruments and calibration theory, we will talk about the mathematical instruments that are used to evaluate the performance of a calibration.

## 2.3 STATISTIC INSTRUMENTS AND CALIBRATION THEORY

### 2.3.1 Normal distribution of Gauss

We are performing measures to ensure industrial process quality control and, citing Montgomery [17], quality is inversely proportional to variability.

This is more valid in measurement. A measurement is reliable if by always measuring the same object the value obtained varies little.

The best estimate for a quantity that varies randomly is the average  $\bar{x}$ . But we need to evaluate also the variability of this quantity, because the variability of  $\bar{x}$  indicates how reliable  $\bar{x}$  is.

The most common instrument used to evaluate the variability of a quantity  $x$  is the standard deviation obtained from the normal distribution of Gauss.

If  $x$  is a normal random variable, then the probability distribution of  $x$  is as in Figure 2-10.

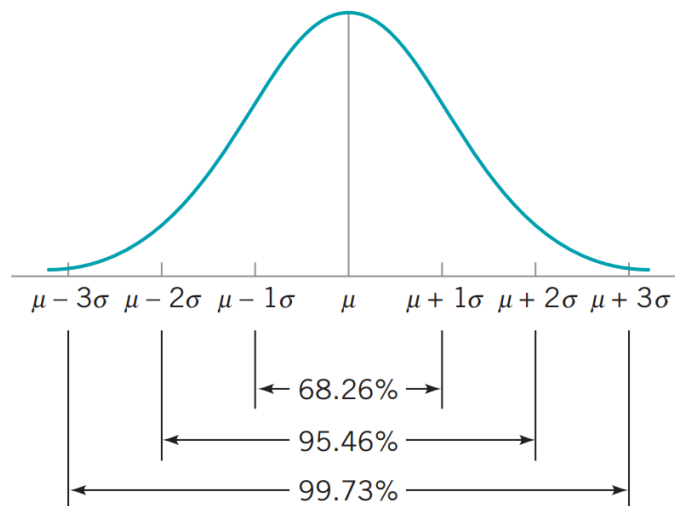


Figure 2-10. Normal distribution of Gauss [17].

In this graph:

- $\mu$  is the mean value of  $x$ ,
- $\sigma$  is the standard deviation of  $x$ .

When dealing with a normal distribution, which is a bell-shaped curve describing how data is spread:

- within  $1\sigma$ : 68.26% of the data falls within one standard deviation from the mean in both directions, this means if you have a lot of data points, about 68.26% of them will be within the range of the average plus or minus one standard deviation;
- within  $2\sigma$ : 95.46% of the data falls within two standard deviations from the mean; so, if you take a wider range, twice the standard deviation in both directions from the average, you'll capture around 95.46% of the data;
- within  $3\sigma$ : an even more extensive range, three times the standard deviation in both directions, encloses roughly 99.73% of the data points in a normal distribution.

The standard deviation uses the following formula:

$$\sigma = \sqrt{\frac{\sum_{i=1}^N (x_i - \bar{x})^2}{N - 1}}$$

where:

- $\bar{x}$  is the average value of the quantity  $x$ ,
- $N$  is the numerosness of the dataset.

### 2.3.2 Measurement system and calibration

A measurement system serves the purpose of quantifying an input parameter, denoted as  $q_i$ , and generating an output,  $q_o$ , corresponding to this input.

The term  $q_i$  represents the measured physical quantity under observation.

In most instances, an analogue sensor's  $q_o$  typically manifests as an electrical analog signal, commonly voltage or current.

However, digital sensors are also prevalent, producing a numerical value as their output. Figure 2-11 illustrates a schematic depiction of this measurement setup.



Figure 2-11. Representation of a measurement system.

The person observing the system intends to derive the input quantity  $q_i$  from the resulting output  $q_o$ .

This feat is made possible by understanding the correlation established between the output quantity  $q_o$  and the input quantity  $q_i$ .

This is usually expressed as an equation:

$$q_o = f(q_i).$$

This equation is a model for the ideal operation of the sensor and is shown in Figure 2-12.

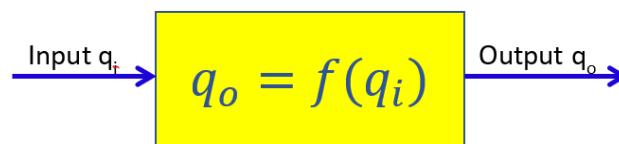


Figure 2-12. The model used in a measurement system.

This model can be determined experimentally by calibrating the sensor.

Therefore, we can see that calibration is a fundamental procedure that allows an instrument to measure unknown input quantities. The relation  $q_o = f(q_i)$  is the calibration function.

When the “observer” uses a sensor, he will read the quantity in output  $q_o$ .

Inverting the equation,  $q_o = f(q_i)$ , the observer can determine the input quantity as follows:

$$q_i = f^{-1}(q_o).$$

In most cases, the output doesn't depend on one quantity, but is determined from  $N$  other quantities [33]:

$$q_o = f(q_{i1}; q_{i2}; \dots; q_{iN}).$$

Considering that we usually are looking for only one or two (as in our case) quantities, all other quantities can be considered as noise. Each noise effect will increase the uncertainty of a measurement system.

*The most common noise effect is done by temperature.*

*Example: with a caliper that doesn't receive the effect of thermal expansion we measure a steel bar. This bar is long and is 100 mm at 20 °C. Utilizing the same instrument at 200 °C, the instrument will measure*

a different length. The difference in length  $\Delta L$  done by thermal expansion is expressed by the formula (UNI ISO 22514:7):

$$\Delta L = \alpha L_0 \Delta T$$

where:

- $\alpha$  is the coefficient of thermal expansion;
- $\Delta T = \text{final temperature} - \text{initial temperature} = T_f - T_0$ ;
- $L_0$  is the length at the temperature  $T_0$ .

### 2.3.3 Uncertainty of the instrument

The result of a measurement is not the certain value of a quantity. It is just an estimation because it must be every time accompanied by a statement of uncertainty.

Citing the ISO Guide to the Expression of Uncertainty in Measurements (GUM) [33]:

*The word “uncertainty” means doubt, and thus in its broadest sense “uncertainty of measurement” means doubt about the validity of the result of a measurement.*

And also:

*uncertainty of measurement parameter, associated with the result of a measurement, characterizes the dispersion of the values that could reasonably be attributed to the measurand [33].*

Considering the average value of a measure  $x$ , the uncertainty  $u_x$  can be expressed in the measure within an interval range:

$$x_{\text{measured}} = x \pm u_x$$

There are two types of evaluation of standard uncertainty.

**Type A of uncertainty considers repeated observations.** This method is rigorous because usually, a quantity  $q_i$  varies randomly.

To evaluate the uncertainty of an instrument statistically it is used the standard deviation. However, a quantity measured with only one standard deviation is correct only in 68% of cases (see Figure 2-10).

In most cases is considered an expanded standard deviation:

$$U = k\sigma,$$

where  $k$  is called the coverage factor and is typically in the range 2 to 3.

GUM suggests using  $U = 2\sigma$  in order to express random uncertainty at a 95% confidence level.

The uncertainty can be determined through calibration, by analysis of the residuals of the calibration data with respect to the regression function.

**Type B of uncertainty evaluation of standard uncertainty consider all other cases that have not been obtained from repeated observations.** It uses “a priori” information as:

- previous measurement data;
- experience with or general knowledge of the behaviour and properties of relevant materials and instruments;
- manufacturer's specifications;
- data provided in calibration and other certificates;
- uncertainties assigned to reference data taken from handbooks.

In the chapter Calibration, we evaluate the performance using type A of uncertainty. When a calibration of an instrument is done is needed to describe how the uncertainty value is determinate [33].

For our sensor, we evaluate uncertainty using standard deviation on residuals  $\varepsilon_i$ , where for the generic quantity  $q$  the residual  $\varepsilon_i$  is

$$\varepsilon_i(q) = q_{i-real} - q_{i-evaluated}$$

So, the evaluation of standard deviation is performed as:

$$\sigma = \sqrt{\frac{\sum_{i=1}^N (\varepsilon_i - \bar{\varepsilon})^2}{N - 1}}$$

Chapter Calibration describes also the calibrator target that was purchased before the work in this thesis. Then in the same chapter, we arrive at the heart of this work, where there is a description of logical choices and methods are described and developed to perform the calibration.

In the end, the performance obtained with this sensor is described with standard deviation in chapter Results.

Then in the last chapter, before Conclusions, are described possible further improvements to reduce the standard deviation.

## 3 Laser line triangulation system

### 3.1 LASER

The laser line source follows the scheme in Figure 3-1 and:

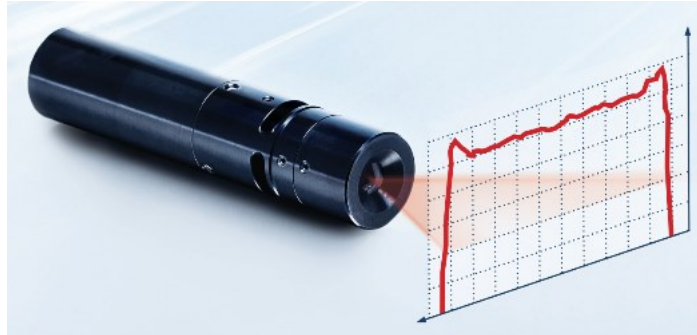


Figure 3-1. Laser plane source [2]. The red graph is a representation of the laser line source intensities along the line perpendicular to the optical axis of the laser.

- project a light plane,
- with a wavelength of 660 nm (red field),
- performs modulation from 0% to 100% of power in less than 5 us, with an external output that ranges from 0 V (0% of power) to 5 V (100% of power - Figure 3-2);
- has an aperture angle of 60°.

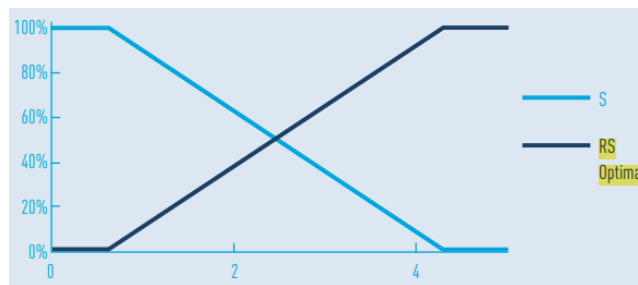


Figure 3-2. Modulation of laser intensities (y-axis) as the voltage (x-axis) increases. The model used is RS. Image taken from datasheet [2].

The intersection between the plane produced by the laser source and the Field Of View (FOV, what the camera sees, decided by the configuration in Figure 2-8) results in a working trapeze as shown in Figure 3-3. The working trapezoid represents the area in which the sensor is able to make the measurement.

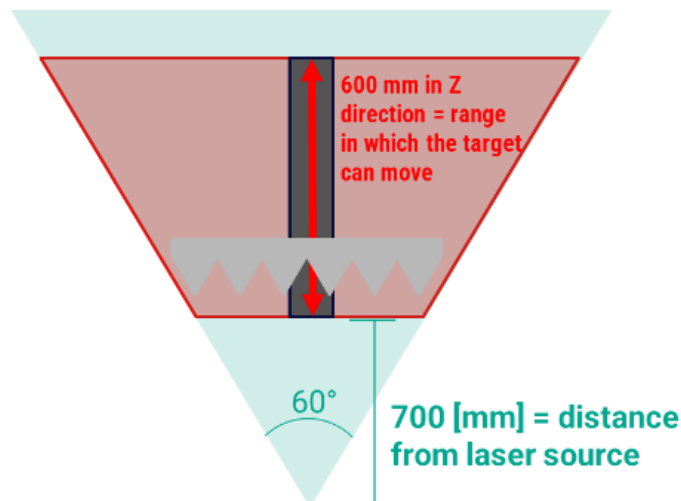


Figure 3-3. In green laser plane produced, in red what the camera can see.

The laser source is known for its high power in a little spot. This energy is usually expressed as Irradiance or flux density of radiant energy, that is the power incident on a unit area [31].

The Irradiance, or intensity profile of the laser line, has a Gaussian form as shown in Figure 3-4 [7].

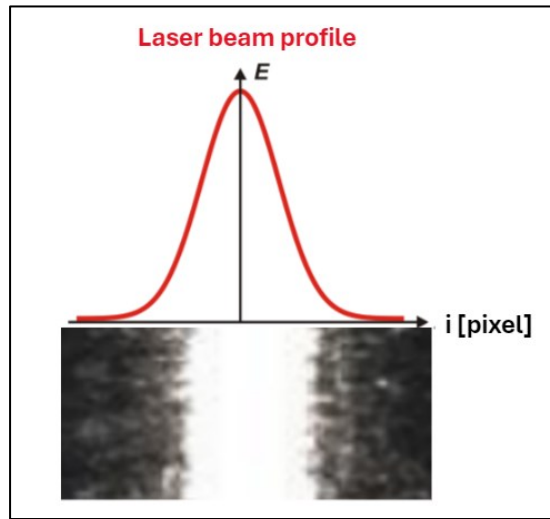


Figure 3-4. Laser profile energy compared to what is shown by the sensor.

It is needed to search the center of the Gaussian profile to understand the true position of the laser line in each column of the sensor and use this position to perform the triangulation.

The device, after the laser source, mounts an optical system on the head. This system, like all optical systems, requires focusing. The discussion regarding focusing is postponed to the section Lenses and Focus.

### 3.1.1 Initial setup

The target, thanks to a motorized linear stage, will move along the Z axis that ranges from  $Z = + 300$  mm to  $Z = - 300$  mm according to what is shown in Figure 3-5 and Figure 2-9.

At the beginning of my thesis, the reference target and the sensor made with carbon fiber tube were not available. Therefore, to perform initial tests and to parallelize activities:

- it is used a 3D printed calibrator (therefore with high machining uncertainties, typically 0.1 mm), long 800 mm and with tooth distance is 50 mm;
- the structure material is aluminium (Figure 3-5).

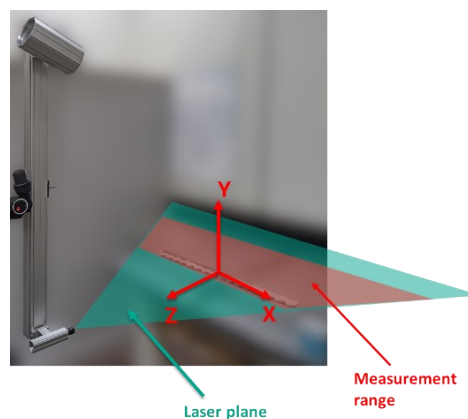


Figure 3-5. Setup of the experiment.

For the final calibration bench, we use a purchased calibration target with greater accuracy (0.025 mm) obtained with CNC, better described in the chapter Zigzag calibration target.



## 3.2 CAMERA CHARACTERISTICS

The camera sensor is a CMOS (Complementary Metal-Oxide Semiconductor) sensor optimized for the acquisition of 3D profiles by the laser line.

The data extraction is performed and processed by the camera while the acquired profile is sent to the PC via a Gigabit Ethernet interface (GigE). This allows the program to achieve high frame rates due to the ability to process data directly on-board of the camera.

### 3.2.1 How CMOS sensors work

This sensor uses the CMOS technology that has the typical architecture shown in Figure 3-6.

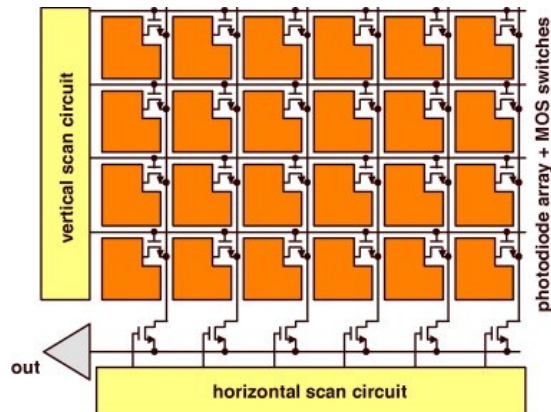


Figure 3-6. The architecture of a two-dimensional CMOS image sensor. Image taken from [28].

In this camera, there are 1088 rows X 2048 columns of pixels.

The pixel (Figure 3-7) is a photodiode that works as a capacitor.

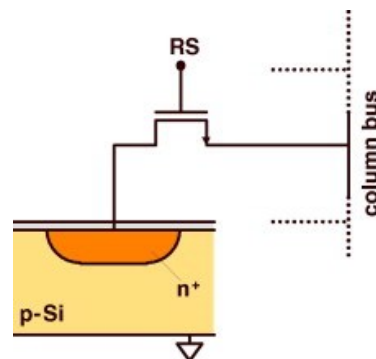


Figure 3-7. A representation of a pixel [28].

The working principle can be understood as follows:

1. when the picture-taking begins, the photodiode starts with a high voltage;
2. during the time in which the camera takes the photo, time called exposure time, the light, which is a flow of photons, decreases the voltage in the photodiode because it has accumulated electrons thanks to the semiconductor material,
3. after the picture's taken, they check how much the voltage dropped; that tells them how much photons hit the photodiode during the picture;
4. then, they get the photodiode ready for the next picture [28].

The photon flux that reaches the pixel depends on the light source and follows the formula:

$$\text{photon density (or photon flux)} = \phi_p \frac{1}{m^2s} \propto I = \text{Irradiance of light source} \frac{W}{m^2}.$$

The number of photons gained by the pixel in the exposure time  $t$  is expressed by the number of electrons that the capacitor gained [29].

A linear simplified formula that evaluates the number of electrons that the pixel gained is:

$$N_p = \phi_p * t * A_{pixel}$$

where  $A_{pixel}$  is the pixel area.

So, the intensities shown in an image are proportional to the number of electrons that the pixel gains. For a grayscale image, the pixel intensity varies between  $I = 0 \div 255$ .

But also, the CMOS capacitor has a  $N_p$  limit caused by material limitations.

This means that for  $\phi_{p1} > \phi_{p2} > \phi_{p3}$  can be obtained  $N_{p1} = N_{p2} = N_{p3}$  if exposure time is enough high. An example is shown in Figure 3-8.

**This produces the common effect called saturation, which is needed to avoid because a high number of saturated pixels causes problems while the sensor is searching for the center of the laser line (in the same column of pixels we need to get different intensity values).**

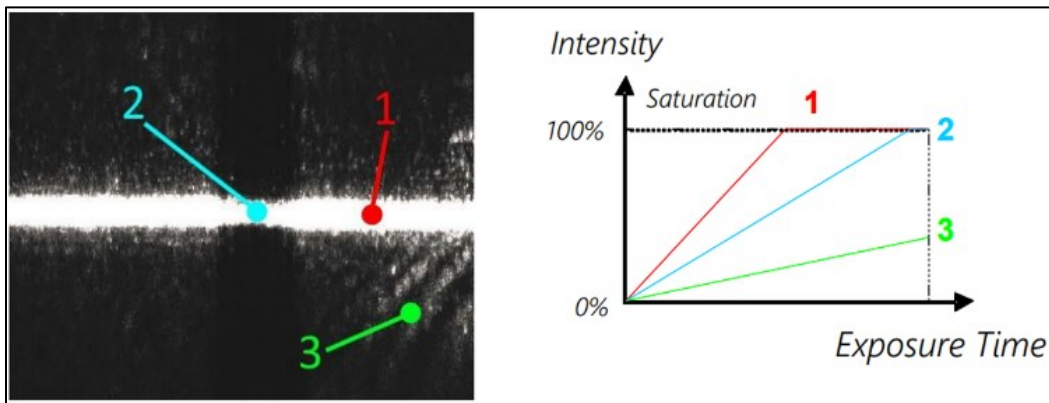


Figure 3-8. The point 1 in the image, which has saturation, has the highest  $\phi_p$ , in fact it has the highest angular coefficient in the graph that shows the Intensity vs Exposure time. In this example we have  $\phi_{p1} > \phi_{p2} > \phi_{p3}$ .

We need to say another thing: the laser produces light of one wavelength, the red one. However, the CMOS sensor typically has a spectral response for a big range of the spectrum with different efficiencies. Figure 3-9 shows how much efficiency the sensor in use has in signal gain vs the wavelength. For a wavelength produced by our laser, 660 nm, the efficiency is 50%.

To reduce the gain produced by light sources of other wavelengths, a filter is mounted on the optics which allows only red wavelength light to pass through.

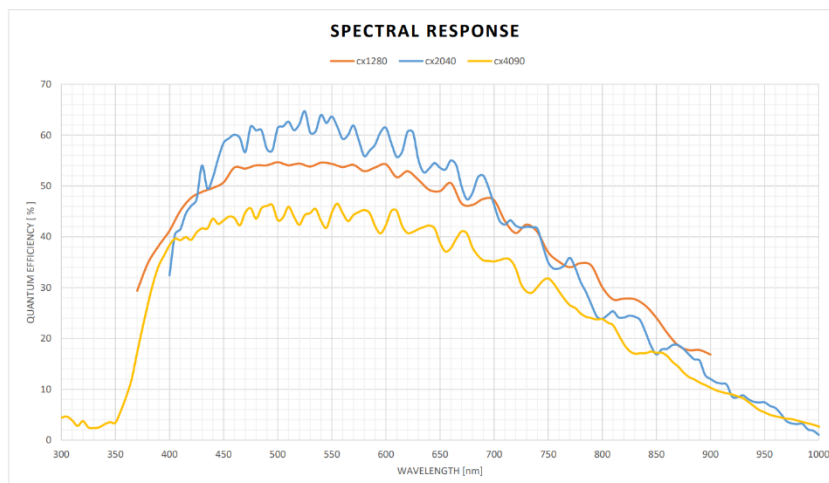


Figure 3-9. Sensor spectral response (image from camera datasheet cited in [1]).

### 3.2.2 Multi Slope Mode

Multi-slope mode is a particular mode that can be performed by the purchased sensor and **is used during calibration and acquisition because it can avoid pixel saturation.**

The user can choose from 1 to 2 knee points to control.

Each knee point can be set as follows:

- It is chosen as a percentage value of the exposure time that corresponds to a time value,
- until the end of this time, the pixel can gain electrons while adhering to a chosen intensity threshold, which represents a percentage of the pixel's capacity in intensities.

A scheme of what can be obtained using a knee point with multi-slope mode is shown in Figure 3-10.

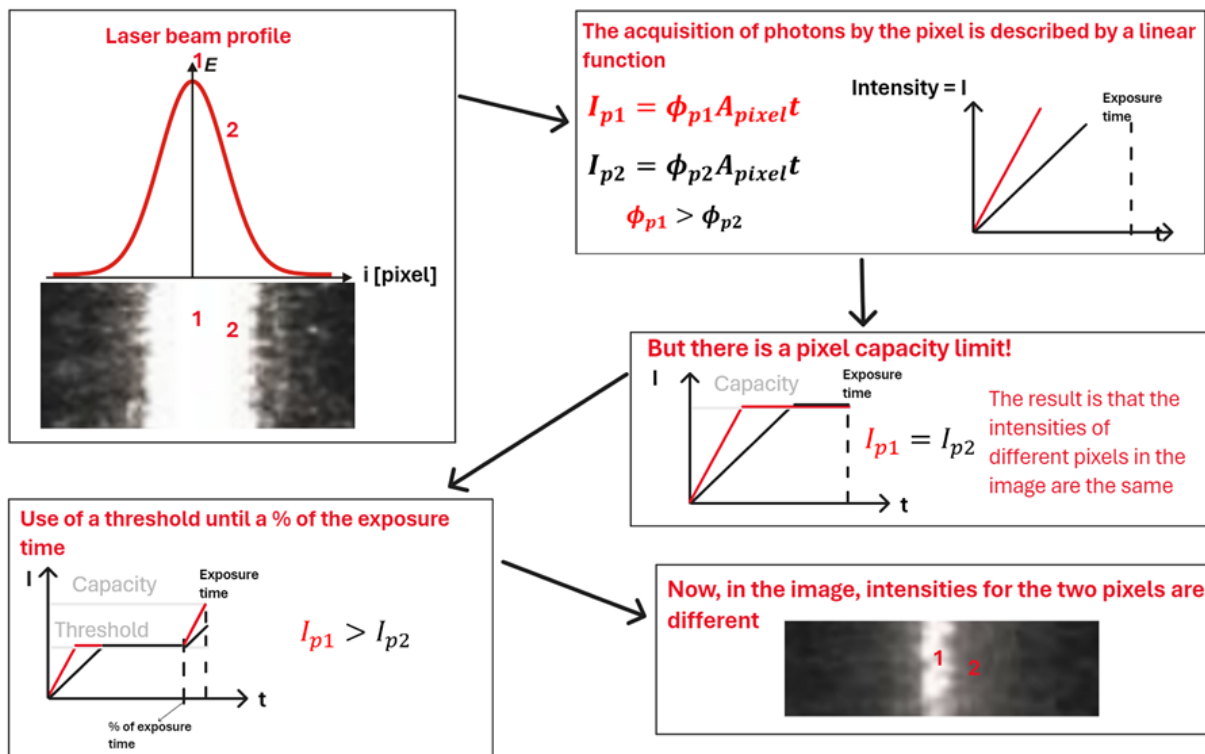


Figure 3-10. Scheme that explains utilization objective of multi slope mode.

This will avoid saturation in pixels that receive a lot of light, reducing laser center width while pixels that receive fewer photons continue to capture.

This mode also reduces the visibility of points enlightened with red environmental light which is a noise for laser line extraction.

For example (Figure 3-11), using two threshold limits is shown that:

- until 500  $\mu$ s each pixel cannot achieve more than 35% of its saturation value;
- until 850  $\mu$ s each pixel cannot achieve more than 67% of its saturation value.

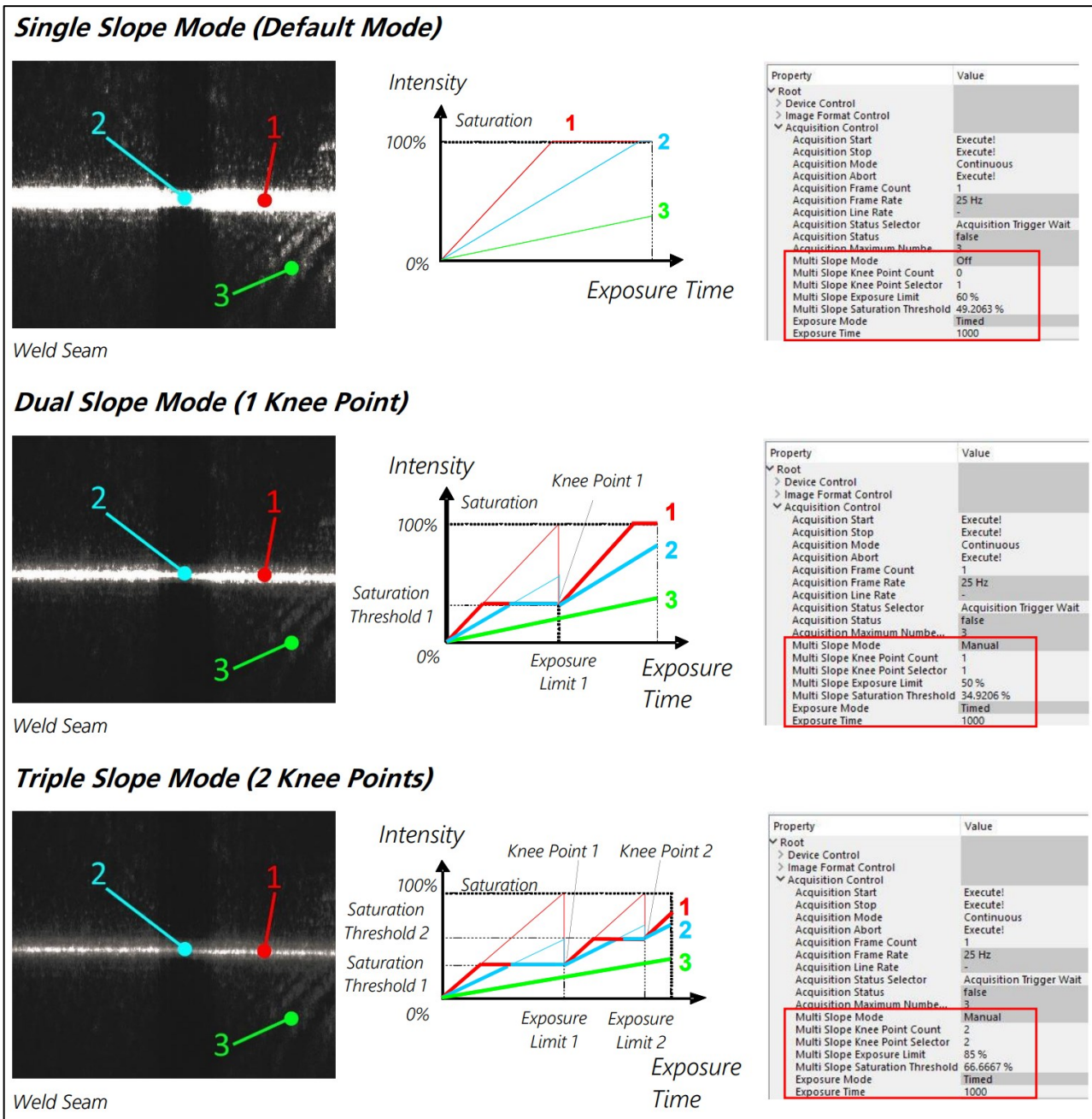


Figure 3-11. Example of using knee points for multi slope mode (image from camera datasheet [1]).

In this section, we talked about light capture mode that involves the performance in signal gain. At this point, we will talk about the camera settings, lens and algorithm to perform the best laser line profile extraction.

### 3.2.3 Setting of the camera parameters

When the camera is initialized, in the code, the user selects the acquisition mode and the program proceeds with setting the parameters loaded directly from a JSON file. This file can be easily edited by the user.

There are many parameters which the user can change, but to avoid serious malfunctions, only the most important parameters are accessible.

So, when switched on, the camera sets many parameters, the main ones are:

- *CameraMode* → sets the data acquisition mode (Image mode, FIR...);
- *ProfilesPerFrame* → is the number of profiles (so the number of frames) acquired in a single acquisition (an array of profiles is given);
- *Exposure time* → is the time that the sensor uses to capture photons and acquire a signal;
- *MultiSlopeMode* → helps avoid saturation by setting limits during exposure time;
- *ReverseY* or *ReverseX* → used to reverse the image that may have been inverted by the optics
- *Subpixel* → n° of bits used to obtain subpixel resolution (see following section 3.2.4).

The camera returns position number formatted with the standard mono16: this type of formatting is in 16 bits and constraints the number to a representation in natural numbers.

With 16 bits the maximum natural number that can be represented is:

$$\text{Available output} = 2^{16} = 65536.$$

### 3.2.4 Subpixel

The camera can find center values ranging up to a maximum of 6 subpixels.

Using the following formula:

$$\text{fraction of pixels} = \frac{1}{2^{\text{sub pixel value}}};$$

this value goes up to 1/64 of a pixel (subpixel value = 6). The value of the subpixel is therefore the number of bits dedicated to quantizing the single pixel.

Considering that instrument resolution is the minimum amount that changes appreciably during a measurement, then using sub-pixels provides better resolution than using full pixels.

The sensor used is composed of a matrix of 1088 X 2048 pixels: if is used subpixel value of 6, it is not possible to use the entire sensor:

$$\text{Available output} = 2^{16} < 1088 * 64 = \text{number of rows} * 2^6.$$

Therefore, a subpixel value of 5 is the maximum to raise resolution. The values obtained are in the possible range:

$$\text{Available output} = 2^{16} > 1088 * 32 = \text{number of rows} * 2^5.$$

### 3.2.5 Sensor mode for laser line profile extraction

This section describes available algorithms in the camera to acquire and extract the center of the laser line beam for each column of pixels [1].

#### The Maximum Intensity Profile Mode (MAX)

In this mode, the position of the maximum value of the light intensity is calculated (Figure 3-12).

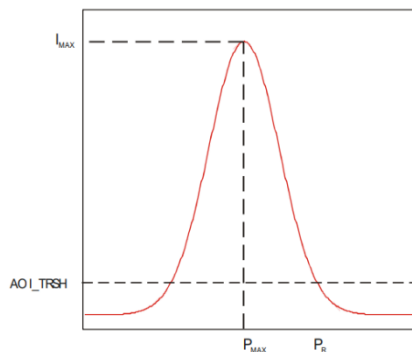


Figure 3-12. Maximum Intensity Profile Mode.

The calculation of the position is therefore given by the position of the maximum pixel: evaluating 1088 rows, which results in a position from 0 to 1087 pixels (11 bits).

When the intensity is saturated in multiple pixels, the first maximum position of the center of the laser line is then considered.

### The Threshold (TRSH) Mode

In this mode is evaluated the center of the laser line that as the average value between the left (PL) and right (PR) positions of all intensities that exceed a threshold (Figure 3-13).

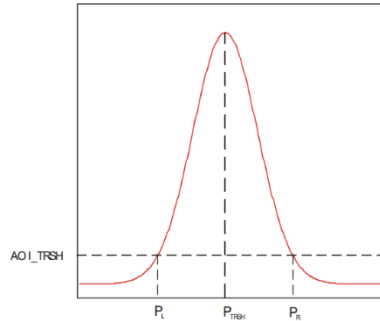


Figure 3-13. The Threshold Mode (TRSH).

$$P_{TRSH} = \frac{P_L + P_R}{2}.$$

To simplify the digital representation and reduce the conversion of floating-point numbers, division by two is not done but an integer representation with only one subpixel is used.

The evaluation of 1088 rows returns a position from 0 to 2174 pixels (11 bits).

### Center Of Gravity (COG) Mode

In this mode, the center of gravity of the laser beam profile is calculated (Figure 3-15). For this purpose, the following parameters are calculated:

- Position value of the left edge of the laser beam profile for a given threshold value of the intensity  $P_L = P_{TRSH}$ ;
- Sum of intensity values  $I_s = \sum I_p$ ;
- Sum of first-order moments  $M_s = \sum I_p * P$ .

The position value of the laser line is therefore obtained from:

$$P_{COG} = P_L + \frac{M_s}{I_s}.$$

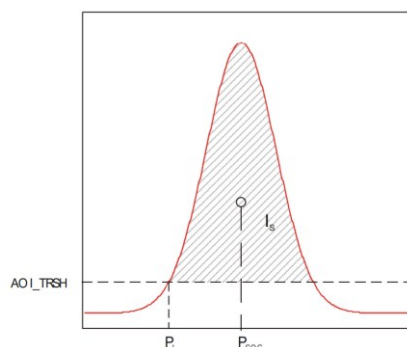


Figure 3-14. The Center Of Gravity Mode (COG).

It can also return the width of the laser line.

### FIR (Finite Impulse Response) Peak Mode

Position evaluation can be improved by using the FIR filter in smoothing mode.

In this mode, the first derivative of the Gauss curve of the intensity (obtained with the FIR filter) of the laser beam profile is calculated. The FIR filter is a signal processing function that aims to increase the

accuracy of laser line detection in the sensor image. It consists of a digital FIR filter and can be used in attenuation or differentiation mode.

Predefined templates with 5, 7 or 9 coefficients allow you to customize the FIR filter to suit the size and shape of your application's Gauss.

The center of the laser beam is the position where the first derivative touches zero and is detected with subpixel accuracy (Figure 3-15).

In this case, the AOI\_TRSH threshold is used to detect the first rising edge of the derived intensity signal. Valid values of the AOI\_TRSH range are from 0 to 1023 (Mono16).

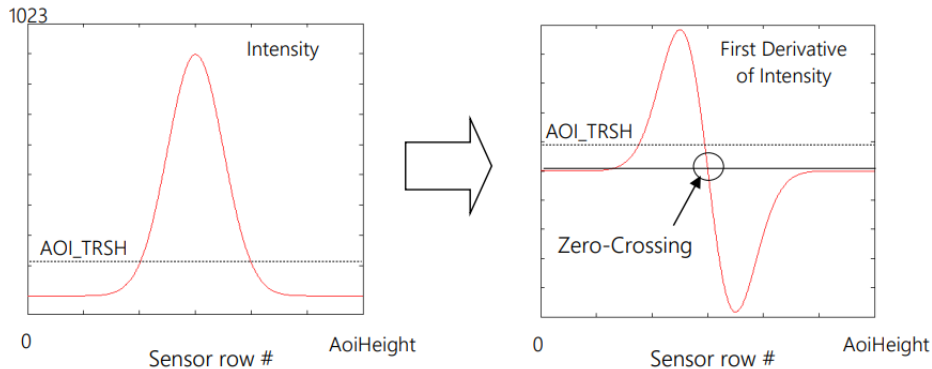


Figure 3-15. Transformation from Gaussian intensities to first derivative.

This mode is used because, unlike COG mode, it prevents the extension of the thickness of the laser line caused by noise or other light sources, because it finds the center choosing the zero crossing in the first derivative of intensity where the intensity is higher.

Instead, the COG algorithm finds the center of the laser line by considering each pixel that is taller than the threshold given.

### 3.2.6 Data Conversion

Consider the pixel frame of reference with the following representation (Figure 3-16).

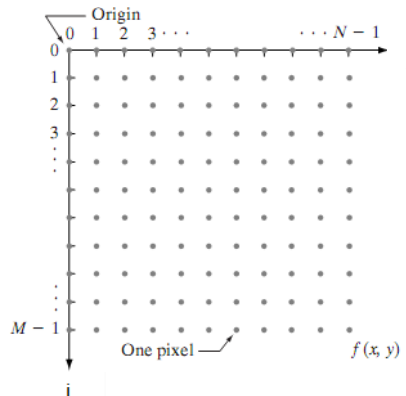


Figure 3-16. Reference system considered.  $j$  facing right and  $i$  facing down

For each  $j$  column, the camera finds the  $i$  row which is situated the center of the laser line, using one of the algorithms of the camera. As we can see in Figure 3-17, this will result in only one vector that represents the profile:

$$\boxed{v11 \quad v12 \quad \dots \quad v1N}$$

Figure 3-17. Vector extracted from the algorithm.

The sensor measures multiple profiles and inserts them into a single frame, based on the ProfilesPerFrame value set (Figure 3-18).

v11	v12	...	v1N
v21	v22	...	v2N
...	...	vmn	...
vM1	vM2	...	vMN

Figure 3-18. Final frame after acquisition. Every single row is equivalent to a profile identified with one of the algorithms seen above.

Explanation of terms:

- $m \in [0 : M]$  depends on parameter  $M = ProfilesPerFrame$  chosen the by the user,
- $j \in [0 : N]$  is the number of columns in the sensor matrix ( $N + 1 = 2048$ );
- $v_{mn} = i_{mn} \in [0 : 2^{16}]$  is the  $i$  value of the  $n$  column during the acquisition of the  $m$  profile by algorithm, considering what we saw in as seen in "Subpixel".

From this frame, the program can get the average value of the positions along the i-axis in the generic n-position:

$$i_{n_{mean}} = \frac{1}{M} \sum_{m=0; n=n}^M v_{mn}; \forall n \in [0:1087];$$

This results in a vector of the type in Figure 3-19.

i0	i1	...	iN
----	----	-----	----

Figure 3-19. Average Profile Final Vector.

The values of  $n \in [0:1087]$  in which the laser line is not detected are placed by the sensor  $i_n = 0$ .

There is a problem: for example, one of the profiles M could be longer than the others. If a single profile on acquisition is longer than a single column  $n$  so that  $i_{mn} \neq 0$ , the value  $i_n$  obtained by averaging  $i_{mn}$  with  $i_{ln}$  values such that  $l \in [0 : M]$  with  $l \neq m$  with gives a result near to zero (example in Figure 3-20). This result is obviously distorted.

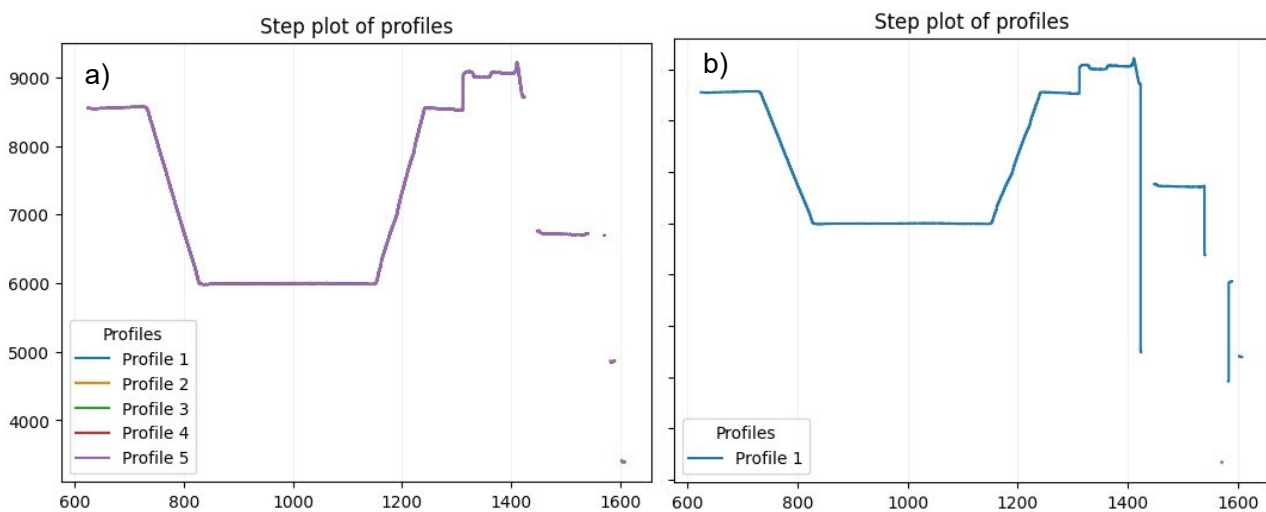


Figure 3-20. Image showing 5 profiles (a) and their average value (b). The downward lines in (b) are produced by averaging between one or more high values and a few zeros.

So, before averaging values it's necessary to convert each 0 to a value that is not calculated in the average value.



This is done by converting the array from 16-bit integers to 64-bit float values and converting all zeros to NaN (Not a Number). This value is then not considered in the calculation of the average value.

### 3.3 LENSES AND FOCUS

When the human eye focuses on a specific object, it uses its lens to sharply define that object on the retina, enabling a clear and detailed image to be perceived.

However, objects situated at different distances from the point of focus might appear less distinct or grainy. This blurriness or graininess occurs because the eye's lens is adjusted to concentrate specifically on the focused object, causing light rays from other nearby or distant objects to not converge perfectly on the retina.

As a result, these out-of-focus objects aren't as sharply defined, leading to a grainy or blurred appearance. This selective focusing mechanism allows us to concentrate on specific details while perceiving other elements in our field of vision as less clear or defined.

The principle of selective focus in human vision has parallels in how camera lenses operate, particularly in the context of adjusting focus.

Camera lenses, like the human eye, can adjust focus to capture clear and sharp images of specific subjects. When a camera lens is focused on a particular object, it precisely aligns its optics to ensure that the light rays from that object converge precisely onto the camera's sensor or film, creating a sharp image.

However, objects located at different distances from the focused subject might appear blurred or out of focus in the resulting image. This blurriness occurs because the camera lens, like the eye, has a limited depth of field. Objects outside this focused range won't be in sharp focus and will appear less defined or blurry.

Just as the human eye selects a specific object to focus on, camera lenses can selectively focus on a particular subject while causing surrounding objects to appear less sharp or grainy. This similarity between human vision and camera lenses in terms of selective focus demonstrates how both systems prioritize clarity for specific subjects while other elements in the scene might appear less defined.

A draft of the camera objective that we utilized is shown in Figure 3-21.

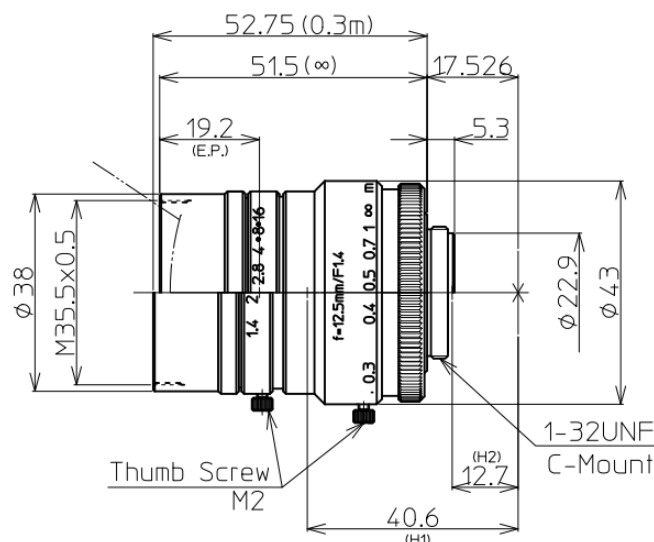


Figure 3-21. Objective mounted on the camera. The screw on the left is used to change the focus, and the screw on the right is used to change the aperture [32].

We performed the focus by placing the target in the origin of our reference system (Figure 2-9).

To get the best focus in a system that uses a laser beam, it is needed to change the focal length until the width of the Gaussian produced by laser nature is reduced as shown in Figure 3-22.

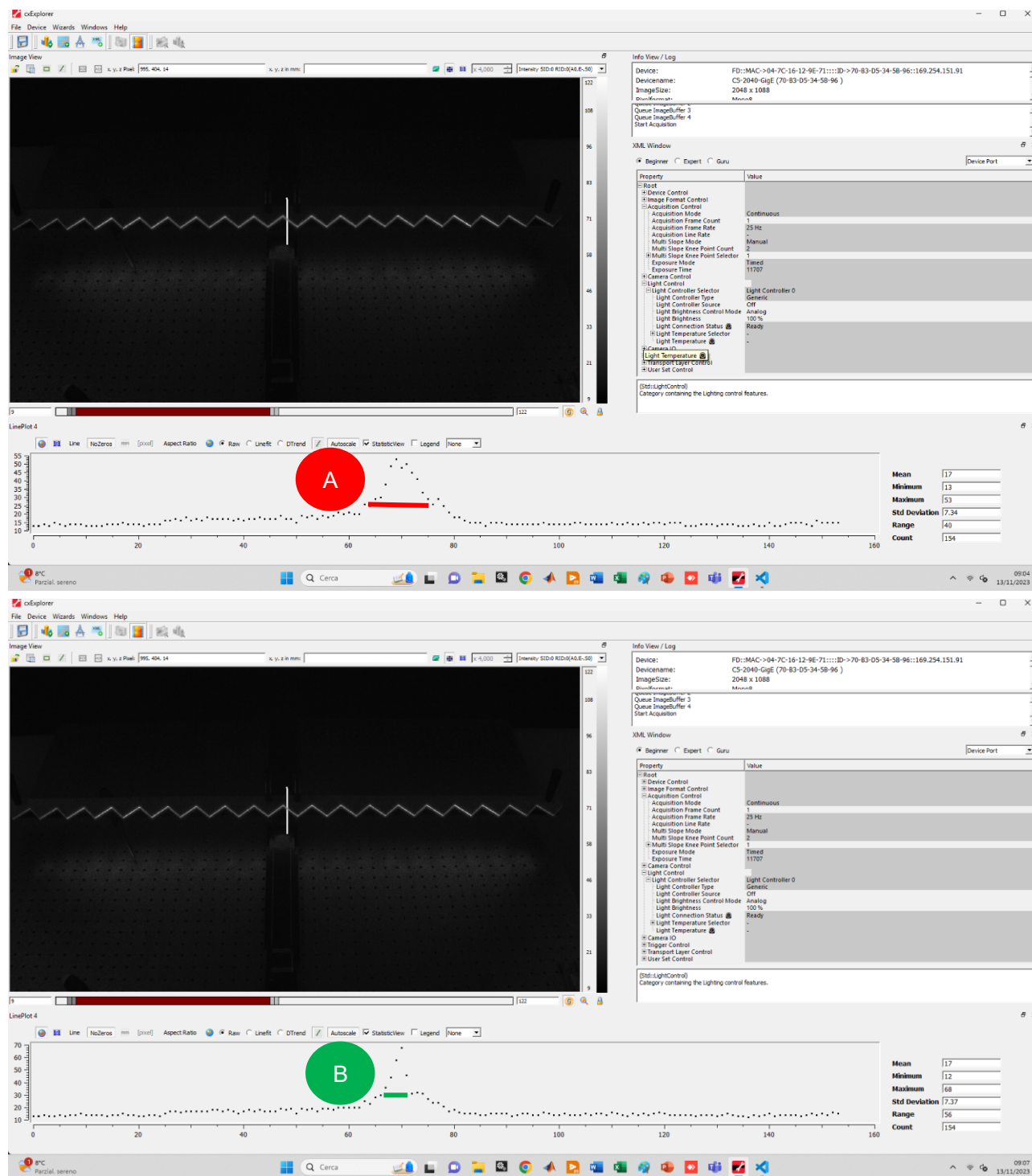


Figure 3-22. Evaluation of the intensity of pixels on a vertical line to obtain the best focus. In image (A) it can be seen a large width in the Gaussian of the laser Beam. It is also possible to see a bimodal intensity effect indicating the divergence of the laser beam (the focus point has been passed). In the second image (B) is shown the effect of the good focus. During this procedure other parameters must not change.

The laser also has an optic that requires focusing. The reasoning is completely similar. After focusing the camera objective, we modify the focus of the laser until we find the minimum width of the Gaussian bell.

### 3.4 HOW TO EVALUATE PERFORMANCE OF CHOSEN PARAMETERS

Pixel intensities  $I$  must be high where is situated the laser line beam to guarantee the correct gain of the signal even under the most unfavourable conditions, as the products that will be measured on the production line have a lower diffusivity material than the calibrator.

Other important parameter is the contrast, that is defined as:

$$\%contrast = \left( \frac{I_{max} - I_{min}}{I_{max} + I_{min}} \right) * 100.$$

When the contrast between the intensities of the laser line and the background noise (which can be assumed as the minimum intensity value in the image) is sufficiently high, the laser line is seen distinctly from the environment. Figure 3-23 shows an example of an image obtained with the following parameters:

- exposure time = 8000 [us].
- multi slope point 1 → 60% Exposure time - 20% saturation of pixel;
- multi slope point 2 → 95% Exposure time - 42% saturation of pixel.

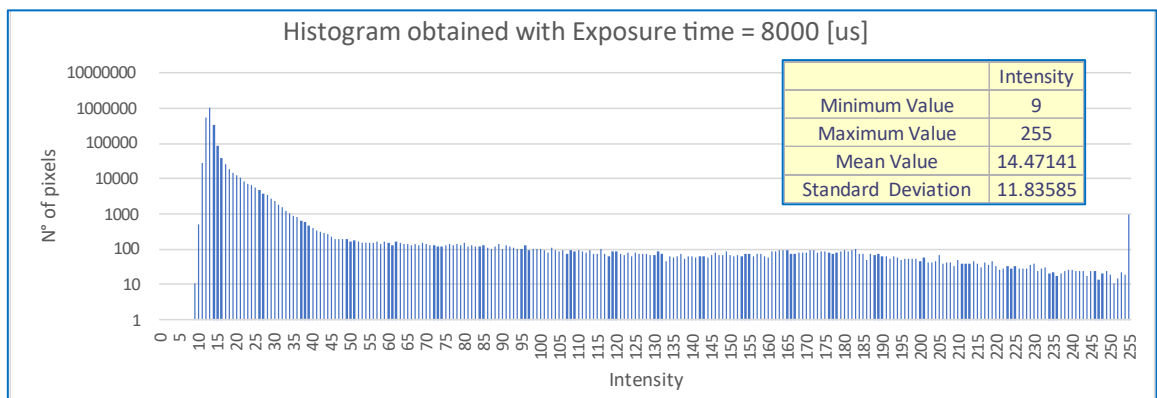
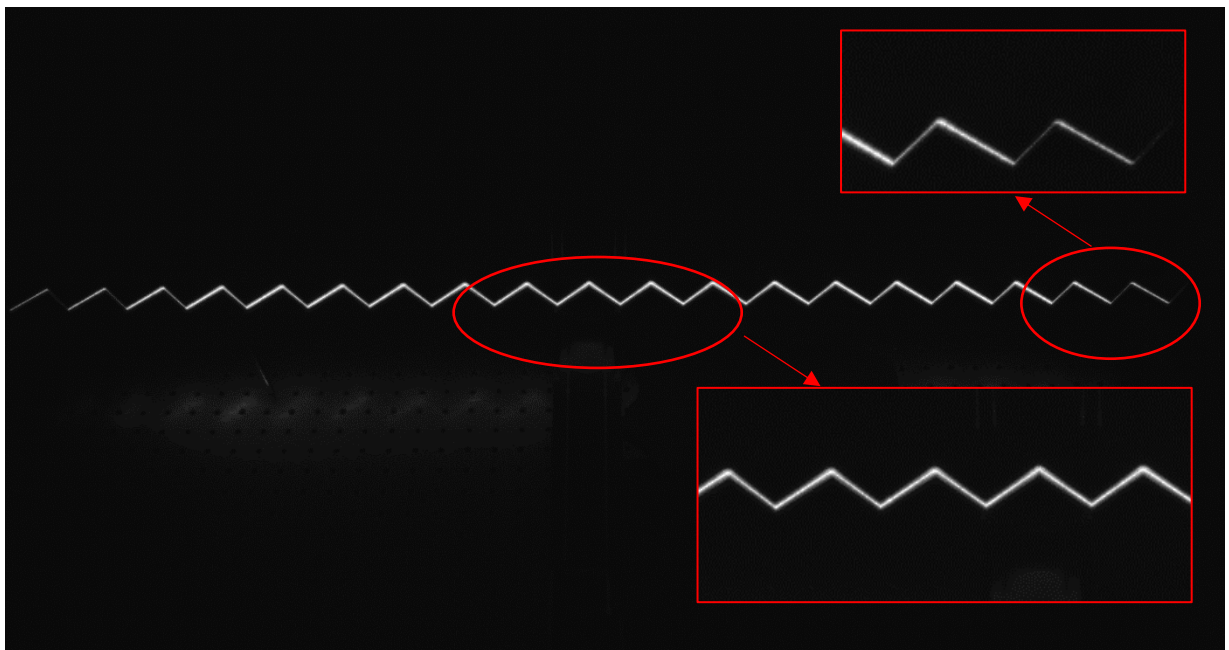


Figure 3-23. Image acquired with chosen parameters on the top. On left the histogram that shows intensity frequency to the entire acquired image.

In this image there is a high contrast between the laser line and the background, especially in the central area of the image where contrast values are reached  $contrast = \frac{246}{264} 100 = 93\%$ . Only a low number of pixels, 2648 (0.1% of the total number of pixels), have a high intensity value (we are considering any intensity value  $I \geq 200$  as high). This indicates that the image has little noise due to reflections and other sources of noise.

## 4 Calibration

### 4.1 CALIBRATION STATE OF ART

Calibration of a laser line triangulation sensor can be done by providing a set of known positions  $(x, z)$  across the measurement range and acquiring their corresponding position  $(i, j)$  on the image.

Calibration of laser line instruments can be performed using one of two main methods:

1. the indirect method, where the formulation of the geometric problem is developed, where intrinsic parameters of the camera are used, such as the focus, the size of the pixel, or extrinsic, such as the relative position between the camera and the laser;
2. the direct method, on the other hand, uses regression analysis to obtain the best parameters to fit a function, through least square interpolation, which correlates the reference input data  $(x, z)$  to the sensor output  $(i, j)$ .

The direct calibration method allows us to obtain better results as the calibration does not bring with it errors due to the incorrect insertion of intrinsic or extrinsic parameters [30]. The calibration function will then be determined by performing a two-dimensional polynomial regression of the sensor outputs  $(i, j)$  versus the reference inputs  $(x, z)$ .

Direct calibration could be achieved by aiming the laser light plane at a three-dimensional target (for example a sphere of known diameter) and acquiring a single image: the image obtained in this way has known coordinates along the entire measurement range.

However, due to the challenges in crafting an accurate three-dimensional target and acquiring a high number of data, simpler two-dimensional and one-dimensional targets are employed and moved with linear stage guide in front of the sensor at known positions.

The target constitutes the geometric reference input necessary for the calibration. Therefore, its geometry must be accurately known.

To ensure precision in the calibration process, the quality of manufacturing for these targets is crucial. Presently, there are four primary manufacturing methods in use: CNC cutting, photo etching, printing, and grinding.

In this project, it has been chosen a commercially available target, manufactured by CNC with a typical accuracy of 0.02 mm.

The target is a slender beam, with a zig-zag-toothed pattern, 600 mm long. Its geometry is reported in Figure 4-1. It has 10 triangular teeth, whose tip provides ten known reference points in the  $(x, z)$  space.

Being the lateral measurement range (along X) larger than 600 mm, a single target is not sufficient; therefore, we decided to use two targets, equal to each other, aligned along the same straight line, to form a unique calibration target of 1200 mm long.

However, the alignment of the two targets cannot be perfect, therefore the actual geometry of the assembled artifact must be measured, to consider it as a good reference for the calibration process.

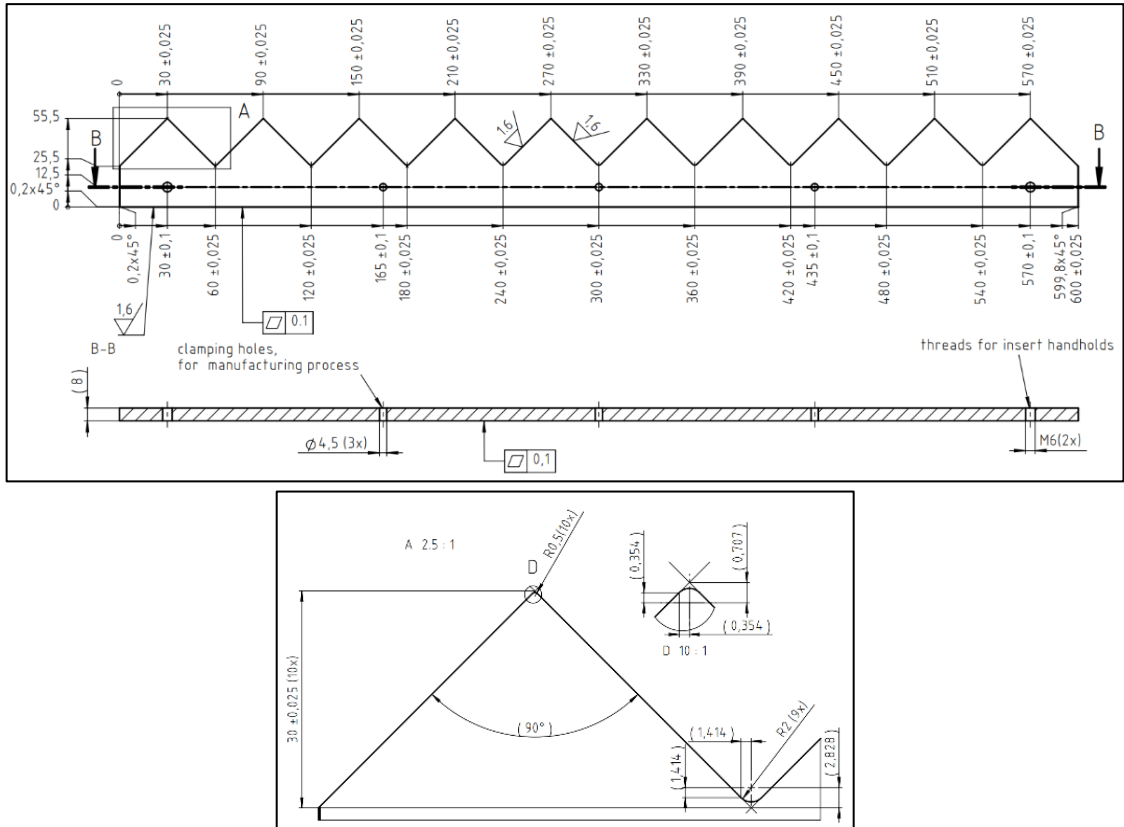


Figure 4-1. Geometry of commercial target.

Calibration with toothed targets can achieve accuracies of 0.048 mm as shown in Figure 4-2 [3]. It is not specified at what working distance this value is obtained. As said in [6] which is a more recent article than [3], state of art shows accuracies at 1 m working distance are equal to 1.5 mm for this class of sensors. However, Figure 4-2 shows a review of the most used calibration targets and their characteristics.

Calibration target	Thumbnail	Type	Manufacturing method	Calibration characteristics
1 2000, zigzag block <sup>[19]</sup>		3D	CNC cutting	High-precision auxiliary servo device is required. Measuring coordinate system is set along the light plane. Using (direct linear transform )DLT method to complete the calibration. Calibration accuracy is 0.048mm.
2 1999, target with two perpendicular planes <sup>[20][21]</sup>				Customized three-dimensional target, high manufacturing costs. Occlusion existing in imaging process. Use principle of cross ratio of invariance for calibration. Calibration accuracy is 0.145mm.
3 2014, gauge block <sup>[13]</sup>			grinding	Gauge block are standard parts with high precision. But calibration process requires high precision auxiliary servo device. Calibration accuracy is 0.0279mm.
4 2015, ball target <sup>[24]</sup>				Ball target are standard parts with high precision. Space cone fitting and space sphere fitting is used for calibration. Calibration accuracy is 0.04mm.
7 2016, chessboard <sup>[25]</sup>		2D	photoetching /printing	Easy for feature extraction. Camera and light plane could be calibrated simultaneously with only one target. But it's difficult to manufacture a large scale target. Calibration accuracy is 0.09mm.
8 2006, array target with circles <sup>[26]</sup>				Easy for feature extraction. Camera and light plane could be calibrated simultaneously with only one target. but it's difficult to manufacture a large scale target. Calibration accuracy is 0.107mm.
9 2014, parallel straight lines <sup>[27]</sup>				Use parallel straight lines constraints for calibration. The calibration method is novel. Calibration accuracy is 0.134mm.
11 2012, single circular ring target <sup>[28]</sup>				Camera and light plane could be calibrated simultaneously. Operation is flexible and easy for site calibration. Calibration accuracy is 0.0368mm.
12 2010, one-dimensional target <sup>[29]</sup>				Easy for manufacturing large size target, and fit for site calibration in target FOV. Use principle of vanishing point for calibration. Calibration accuracy is 0.102mm.
13 2016, linear scale <sup>[30]</sup>		1D	Calibration accuracy is high, but it needs high-precision auxiliary device. The target is particularly fit for applications of small FOV and high accuracy. Calibration accuracy is 0.013mm.	

Figure 4-2. Review of most used calibration targets (image taken from [3]).

## 4.2 ZIGZAG CALIBRATION TARGET

As already said above, to realize the full calibration, it is necessary a target larger than 1000 mm: it is realized by joining the two zig-zag calibration targets, which are aligned and mounted on an aluminium bar with a high moment of inertia to prevent bending and form a unique calibration artifact having 20 triangular teeth equally spaced along X direction.

The full target is then mounted on a linear traversing stage, as shown in Figure 4-3.



Figure 4-3. Target built with FDM process with laser beam projected.

This allows to traverse of the full calibration target along the z-axis, at known positions.

Figure 4-4 shows the calibration artifact, a detail of the tips of each tooth and a photo of the artifact during geometrical characterization by a Coordinate Measuring Machine (CMM). In fact, to assure the accuracy of the calibration, the coordinates of the tip of the teeth are measured at the CMM, to have reference data (x, z) with sufficient accuracy.

The tip of each triangle is not sharp, its actual shape is shown in Figure 4-4 . Therefore, it is necessary to define a “virtual reference point”, derived from the geometry of the tooth. The strategy is to define the X and Z coordinates of the “virtual reference point” associated to the top of the tooth as the intercepts of the two planes representing the two sides of each triangular tooth. These planes are obtained by measuring at least three points on the sides of the tooth with the CMM.

The coordinates of the upper point are obtained with the following method:

1. by measuring several (more than three) points on each side of each tooth,
2. performing their linear regression with a plane for each side of each tooth,
3. the intercept between two planes forms a line, whose center point represents the “virtual reference point” associated to the tooth tip. By this procedure, of that point we know accurately the coordinates X and Z.

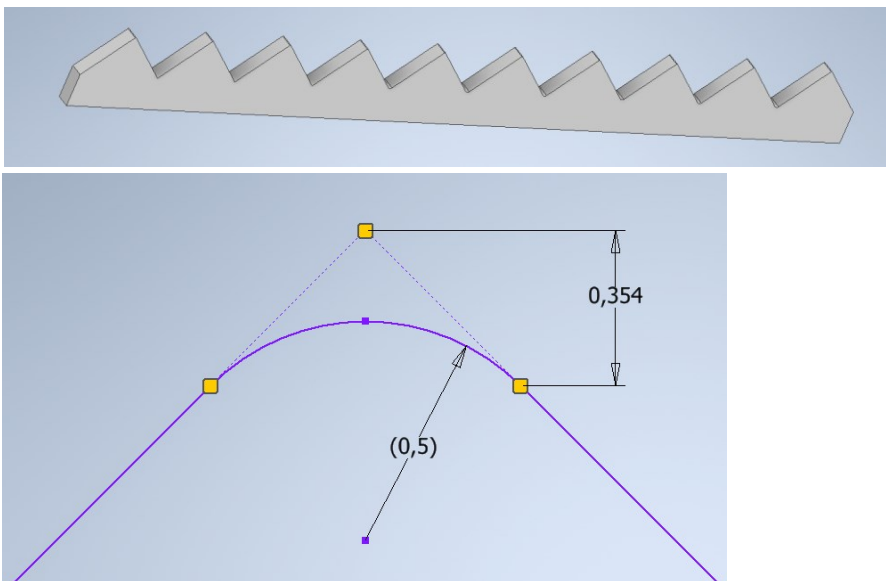


Figure 4-4. On the top, there is a 3D representation of a single calibration target. Dimensions of the single tooth of the target on the left, where there is the point obtained as the intersection given by the lines obtained from the sides of the tooth. On the right, there is a photo of the targets coupled to the CMM.

At the beginning of my thesis, the reference target described above was not available, therefore, to perform initial tests, develop the calibration procedure and parallelize activities, it has been used a target built with the FDM process as shown in Figure 4-3, that is 800 mm long .

Its accuracy is not fit for calibration, however, it allowed the development of the method, that later has been implemented on the real calibration target, when assembled.

**4.2.1 Geometrical measurement and data analysis of calibration target**

The procedure to measure the “virtual reference points” has been performed on the calibration artifact for all the 20 teeth. The results obtained are shown in Table 4-1.

*Table 4-1. CMM virtual coordinates of the upper part of teeth.*

X [mm]	Z [mm]
30.028	55.484
90.034	55.482
150.036	55.484
210.039	55.492
270.048	55.492
330.061	55.485
390.062	55.480
450.064	55.470
510.078	55.465
570.083	55.443
630.066	55.500
690.068	55.670
750.067	55.841
810.076	56.009
870.081	56.177
930.082	56.342
990.088	56.502
1050.096	56.667
1110.098	56.830
1170.105	56.998

The calibration artifact is composed by joining two zig-zag reference targets; even if their alignment has been carefully done, they cannot be perfectly aligned. This is evident from the plot of the 20 acquired "virtual points"; they are clearly two groups of data, each group of 10 data is aligned along a straight line, but the two straight lines are not perfectly aligned.

We have found the two straight lines by linear regression. Then the target can be rotated, so to have the two tips at the left and right side aligned to each other as shown in Figure 4-5.

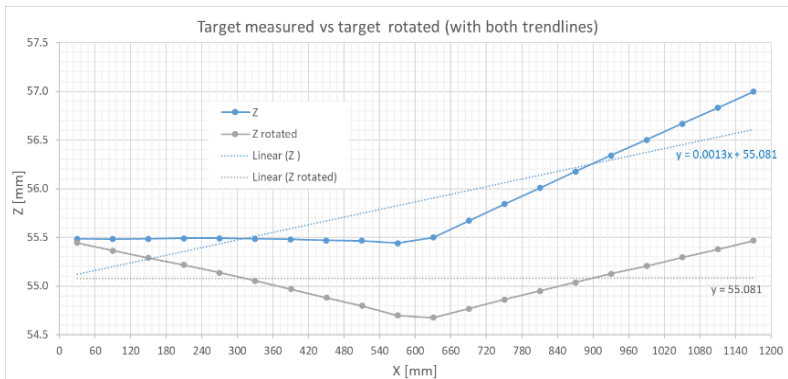


*Figure 4-5. The measured target vs rotated target.*

By checking the results of measurement there is an effect of coupling that added an angle between the two targets.

The final data used as reference for calibration is obtained from centering the coordinates in the X and Z axes (roto-translation until the average value of each axes is set to zero, Figure 4-6).

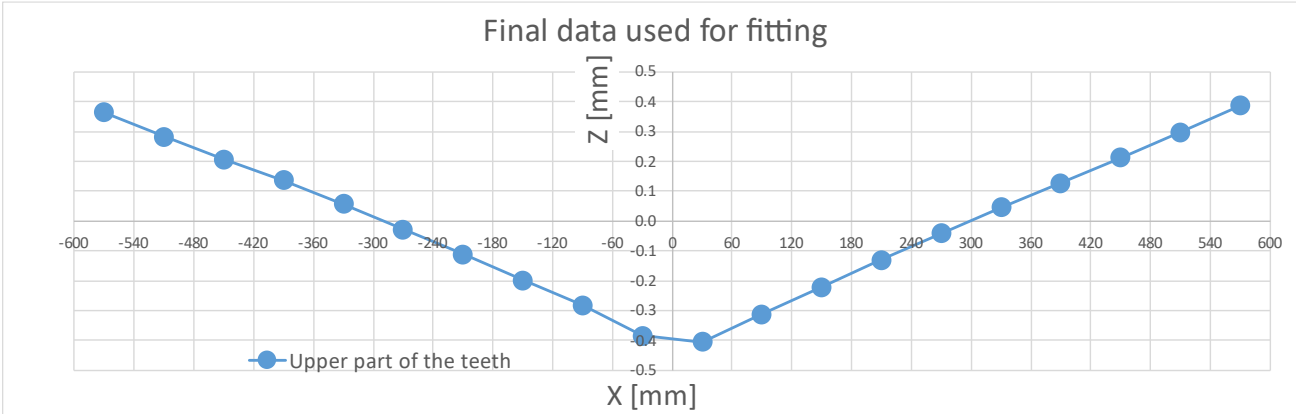


Figure 4-6. Coordinates used for fitting.

### 4.3 ALIGNMENT OF THE LASER TRIANGULATION SENSOR

It is needed to align the laser triangulation sensor orthogonal to the calibration artifact; an accurate alignment is required along all axes, to ensure that the calibration procedure is correct.

At first the calibration artifact is mounted on the translation stage: the axis of motion of the translation stage represents the Z axis, while the x axis is represented by the straight line passing through the first and last tooth.

Once the calibration artifact is mounted and aligned, then the laser line triangulation sensor needs to be aligned to it.

The alignment is done by rotating and translating the laser line sensor; this is possible because the support has the necessary degrees of freedom to allow motion. The alignment steps are iterative, slowly converging towards the aligned target and sensor.

Referring to Figure 4-7, we call  $O'(X',Y',Z')$  the origin of sensor coordinate system and  $O(X,Y,Z)$  target coordinate system when it is placed at 1 m working distance (check Figure 3-5 and Figure 2-9).

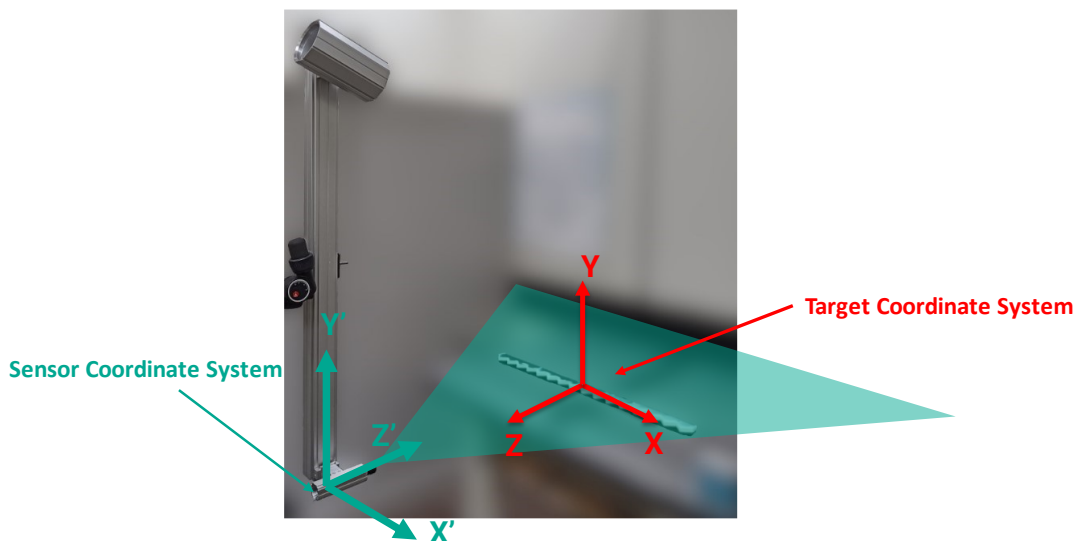


Figure 4-7. Reference coordinates.



The steps necessary to align are:

1. Control with a meter that the minimum working distance between the center of the calibration artifact and the laser, in order to obtain, the correct distance; in our case we must check from the sensor as  $Z'$  ( $Z = 300 \text{ mm}$ ;  $X = 0 \text{ mm}$ ) =  $700 \text{ mm}$ ;
2. Laser line described with  $X'$  axis and  $X$  axis of the target  $\rightarrow$  it can be done easily by eye observing the laser line over the target and assuring that  $X'$  is parallel to the target  $X$ ;
3. Laser line  $X'$  in  $YZ$  plane  $\rightarrow$  it is performed just by checking the position of the projected laser line on the target; this position in  $Y$  direction must be the same when the target is at  $Z = 300 \text{ mm}$  and when it is at  $Z = -300 \text{ mm}$  and for each  $X$ ;
4. Sensor matrix in  $YZ$  plane  $\rightarrow$  it is performed by projecting the laser line to a plane perpendicular to the  $Z$  axis (Figure 4-8); for final tests, we will scan the bar;

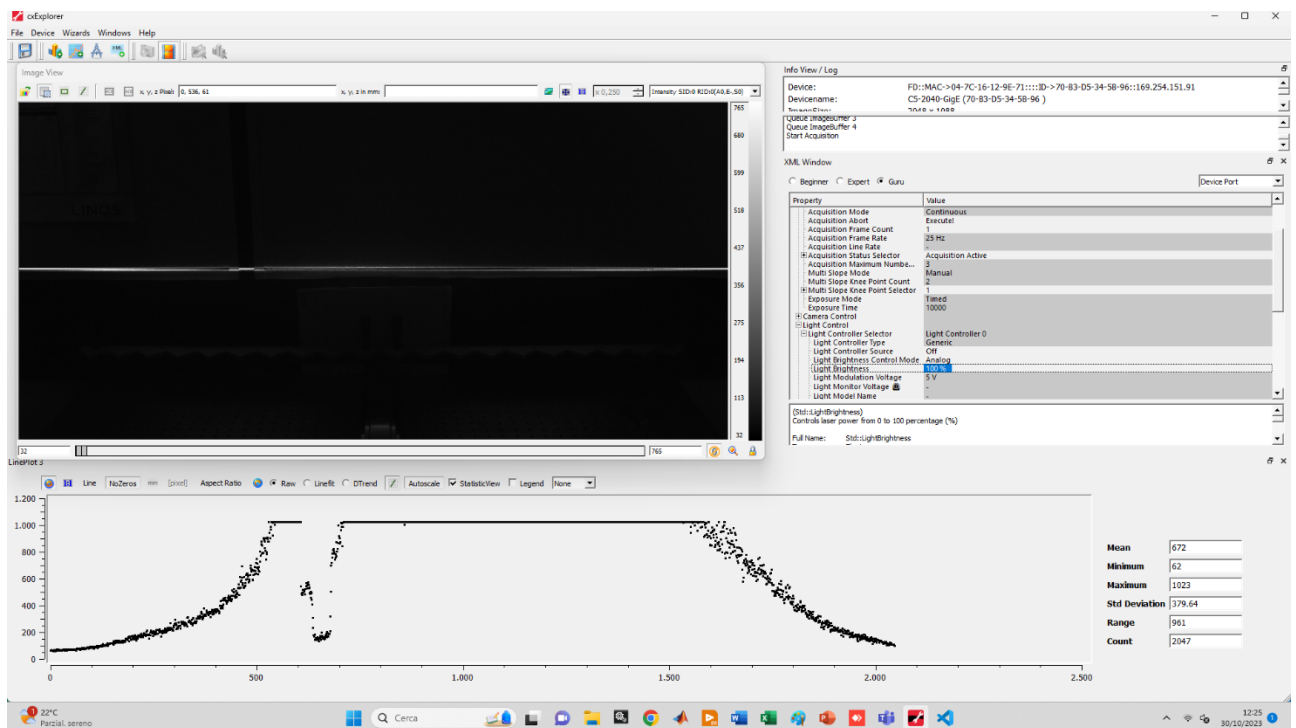
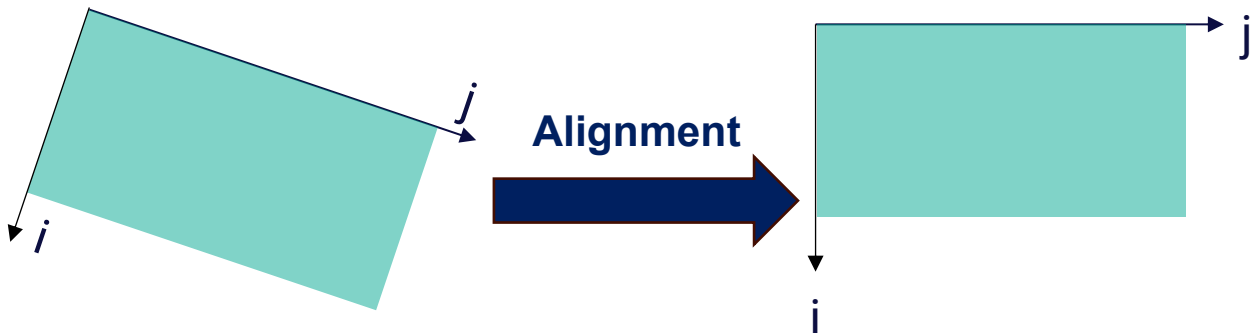


Figure 4-8. In top sensor matrix rotated (not aligned) vs aligned matrix. Below there is an image taken in the base program of the sensor. In this case we performed alignment shooting laser to the wall. For the following test we will use a bar that olds the target.

5. Target difference in  $X$  and  $X'$  position (Figure 4-9) $\rightarrow$  performed by checking the center of the acquired profile;

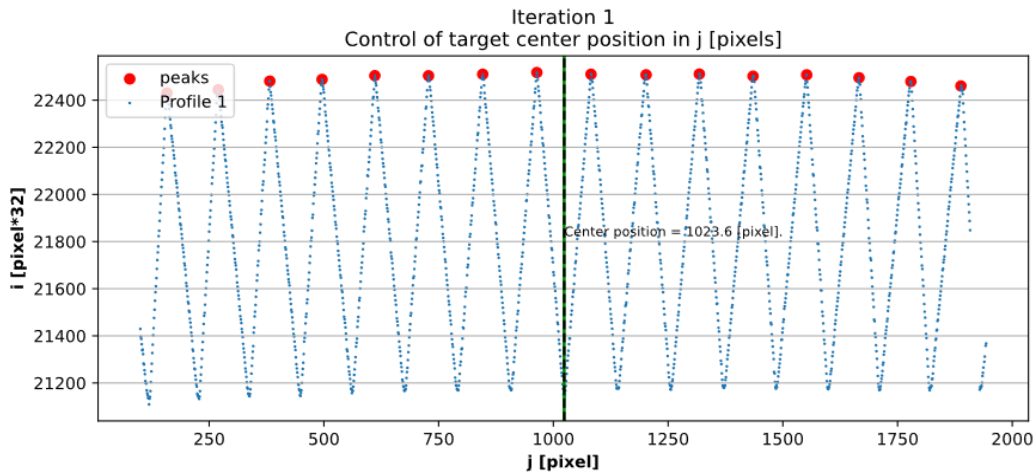


Figure 4-9. Checking the center in X axis.

- target angle between X and Z axes → performed by checking angle in the matrix of pixels given with line regression of peaks positions (Figure 4-10);

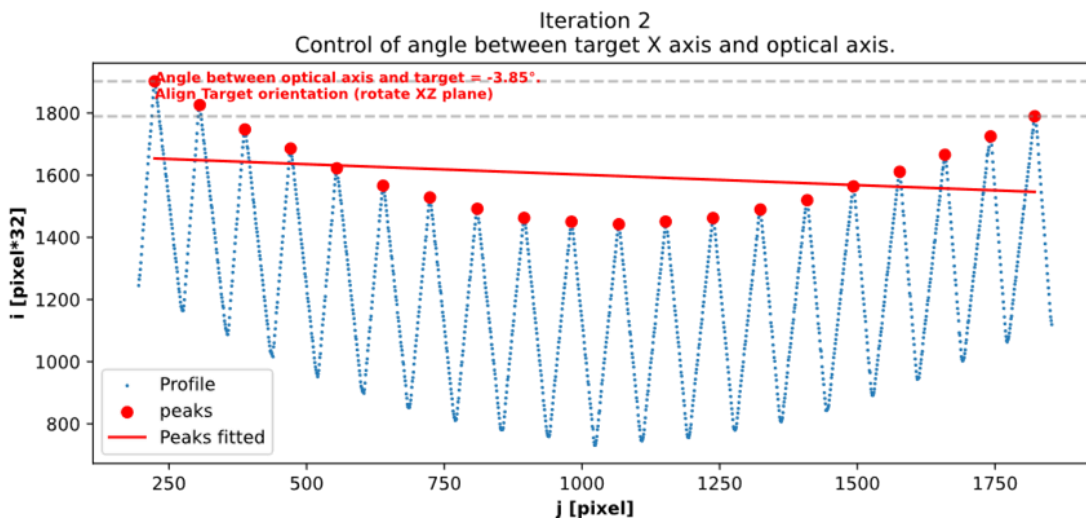


Figure 4-10. Checking the angle between X and Z axes (b). In this case the angle (in pixels) is too high.

- the angle between the optical axis and linear stage axis → performed by checking the difference between the central pixel when the linear stage is at the initial position ( $Z = 300$  mm) and when the stage is at the end position ( $Z = -300$  mm).

To perform alignment along the z axis, it was useful to use the thin gap which forms between the two adjacent targets. It defines a z axis, therefore if the laser beam passes through it, it means that the laser axis is along z axis (Figure 4-11).

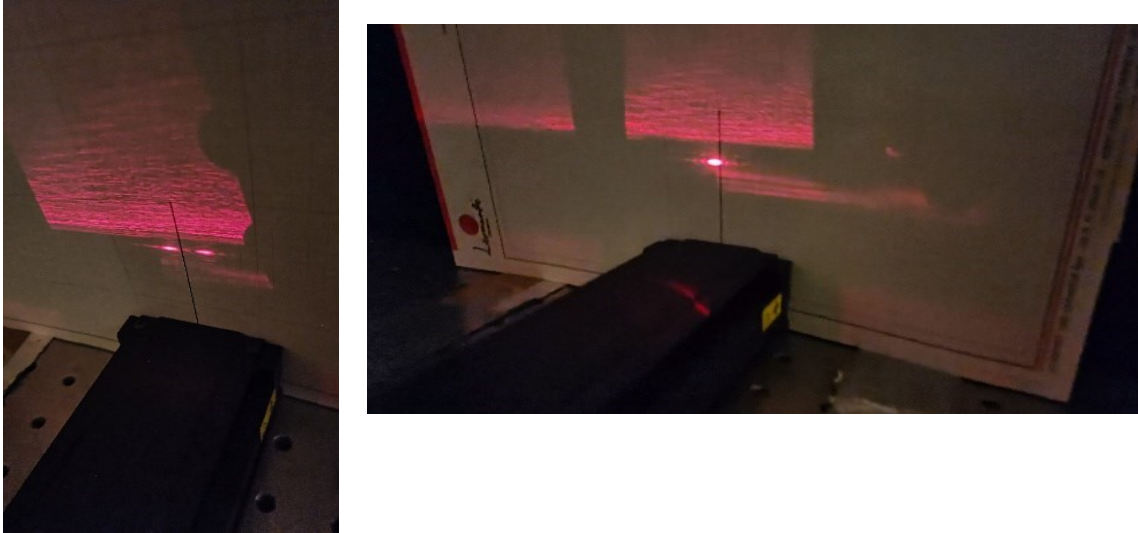


Figure 4-11. At the left photo we can see that laser beam diverges after passing through the joint point. In the right photo the beam doesn't diverge.

When the laser beam doesn't diverge the laser passes through the center and is aligned parallel to the linear stage. In further applications, good practice could be to install a perforated cylinder/prism to facilitate this effect.

#### 4.4 PERFORMING EXPERIMENTS

To calibrate a sensor must be used a function that correctly represents the transfer function that gives real-world coordinates from pixel coordinates, such that:

$$X = f(j, i); \quad Z = f(j, i)$$

##### 4.4.1 Polynomial model

To calibrate a triangulation sensor is a good method the utilize of a polynomial function [27].

The polynomials used are of the type  $pol_{ab}$ , where  $\underline{a}$  is the maximum exponent used for the  $j$  term while  $\underline{b}$  is the maximum exponent used for the  $i$  term.

Some examples below

$$pol_{11} = p_{00} + p_{10} \cdot x + p_{01} \cdot y;$$

$$pol_{22} = p_{00} + p_{10} \cdot x + p_{01} \cdot y + p_{20} \cdot x^2 + p_{11} \cdot x \cdot y + p_{02} \cdot y^2.$$

In these examples, we used  $x$  to substitute the  $j$  column and  $y$  to substitute the  $i$  column for greater readability. Each subscript refers to the exponent of the axis.  $pol_{21}$  means that we use the exponential  $J$ -axis up to order 2 and the for the exponential  $I$ -axis of order 1.

##### Testing the forward and backward movement of the calibrator along the linear stage

We started testing  $pol_{26}$  polynomial model because  $j$  is physically less influenced than  $i$  by movements of the calibrator along the linear stage:

$$\begin{aligned} pol_{26} = & a_{00} + \\ & a_{10}x + a_{01}y + \\ & a_{20}x^2 + a_{11}xy + a_{01}y^2 + \\ & a_{21}x^2y + a_{22}x^2y^2 + a_{12}xy^2 + a_{03}y^3 + \\ & a_{23}x^2y^2 + a_{13}xy^3 + a_{04}y^4 + \\ & a_{24}x^2y^4 + a_{14}xy^4 + a_{05}y^5 + \\ & a_{06}y^6. \end{aligned}$$

Forward and backward movement details (Figure 4-12):

- N° of steps forward = N° of steps backward = 61;
- Total steps = 122;
- Z Range of measure = 600 mm;
- Step length Z = 10 mm;
- N° of teeth in X direction = 16;
- X tooth step = 50 mm (we are using FDM target);
- F# = 4;
- Accepted angle between first and last tooth  $\leq 4^\circ$ ;
- Subpixel bits = 4.

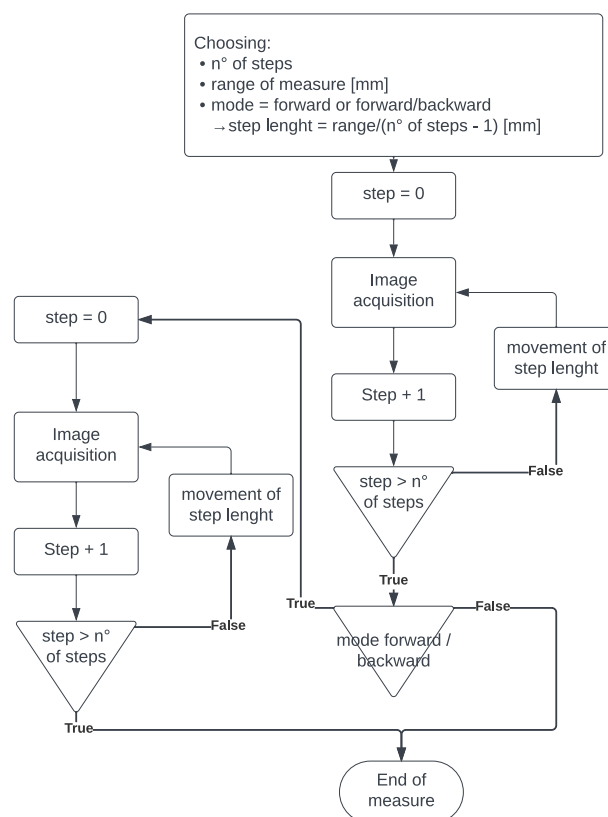


Figure 4-12. Calibration sequence.

It searches for the upper part of teeth (peaks of signal in the image). There is an example of the acquired image in Figure 4-13.

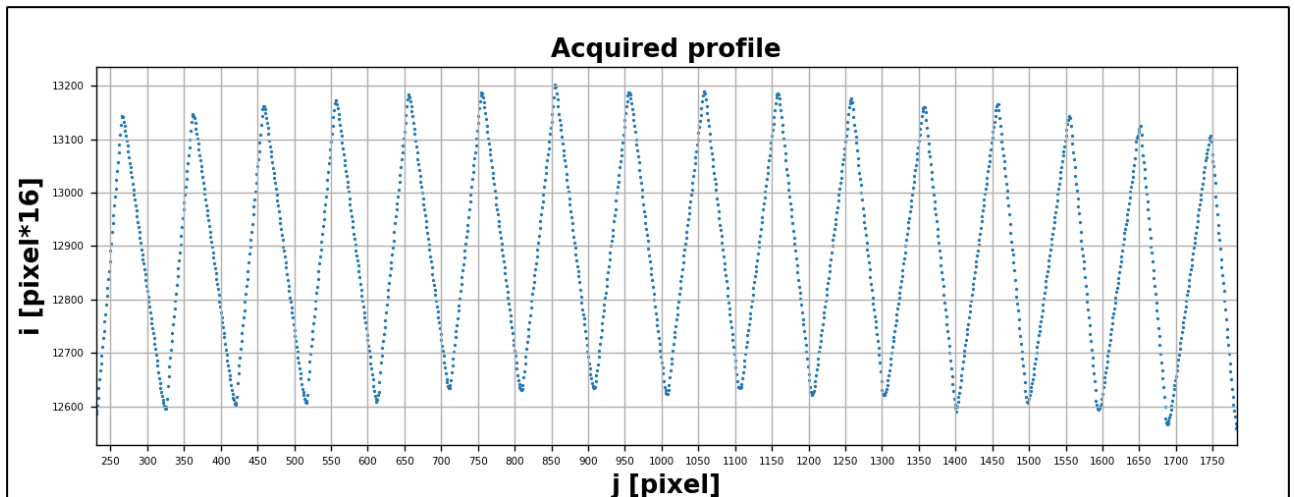


Figure 4-13. Acquired image of the first profile at Z = 300 [mm] using a target with length.

The fitting algorithm (coloured green in Figure 4-14) looks for the value of parameters ( $a_{ij}$ ) to use in the equation to fit the data obtained to the real data and obtain the sum of squares of the residuals equal to 0:

$$\sum_{i=0}^n [\varepsilon_i(z)]^2 = 0;$$

$$\varepsilon_i(z) = z_{i-real} - z_{i-evaluated};$$

where  $z_{i-evaluated}$  is the result of applying the polynomial function.

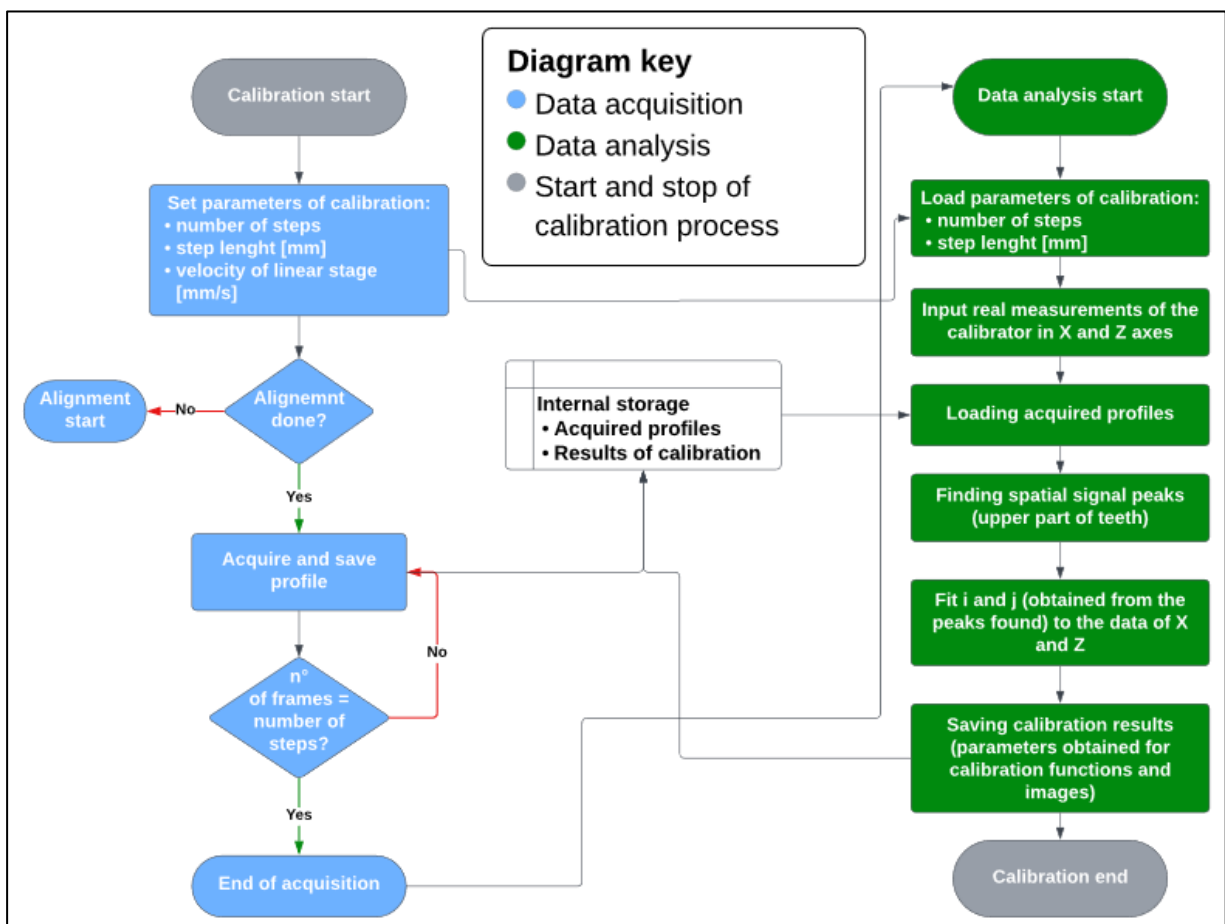


Figure 4-14. Calibration process diagram block.

The calibration surfaces are shown in Figure 4-15. The surface represents the transfer function which transforms the inputs (i and j pixels) to the output in a real coordinate (X or Z). X and Z are described with the same polynomial but with different parameters.

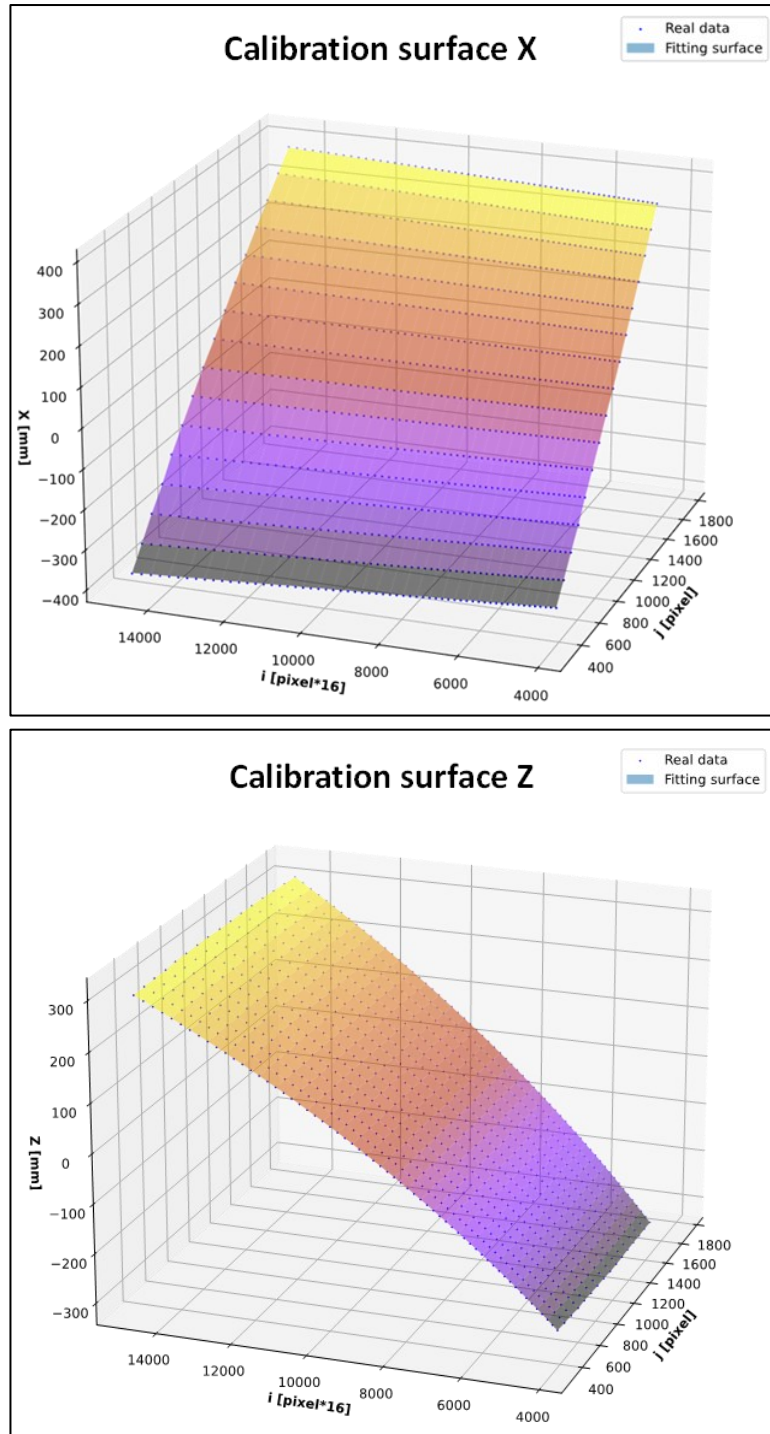


Figure 4-15. Calibration surface and real data points.

The fit is performed correctly if the resulting surface is close enough to the real data point (blue dots).

There is an effect done by backlash as shown in Figure 4-16. Explanation of how the graph in Figure 4-16 is built is below and shown in Figure 4-17.

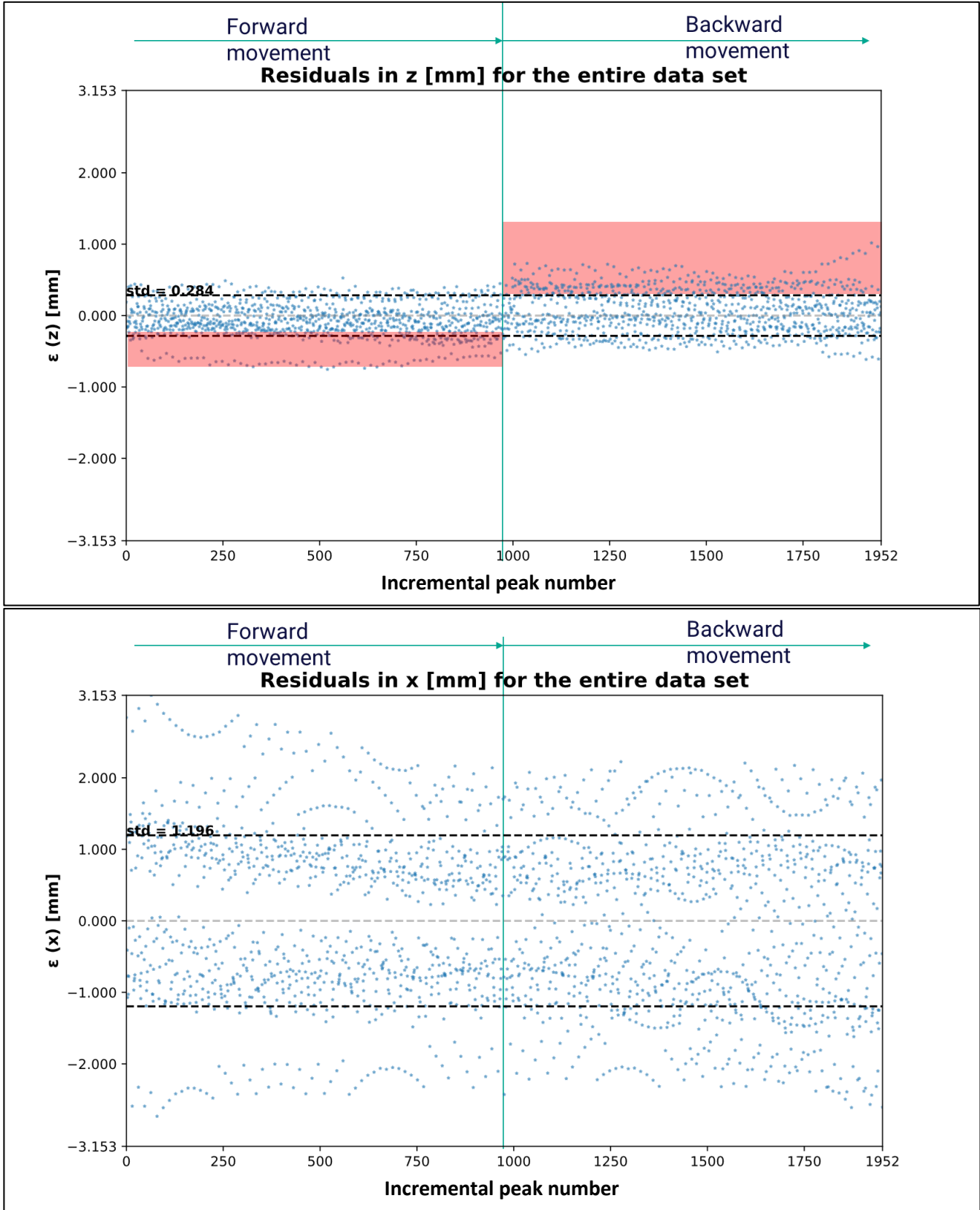


Figure 4-16. Residuals in Z axis (upper graph) and X axis (lower graph).

For example:

- in the first step of the linear stage, there are 16 residual values, from 1 to 16;
- in the second step are acquired other 16 residual values, from 17 to 32;
- this succession of residuals for each peak represents the abscissa axis, while ordinate axis represents their value.

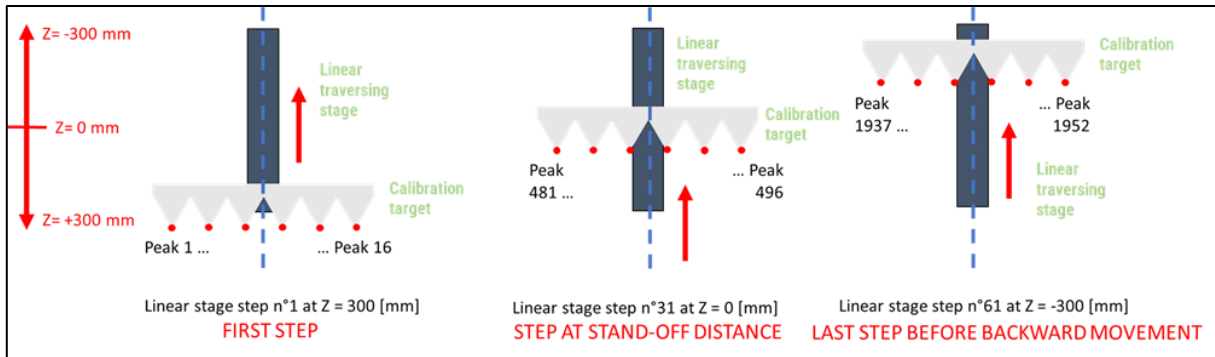


Figure 4-17. Explanation of how is built the graph of residuals using incremental peak number.

This is demonstrated by evaluating residuals only in one direction as shown in Figure 4-18: forward movements have different average values than backward movements.

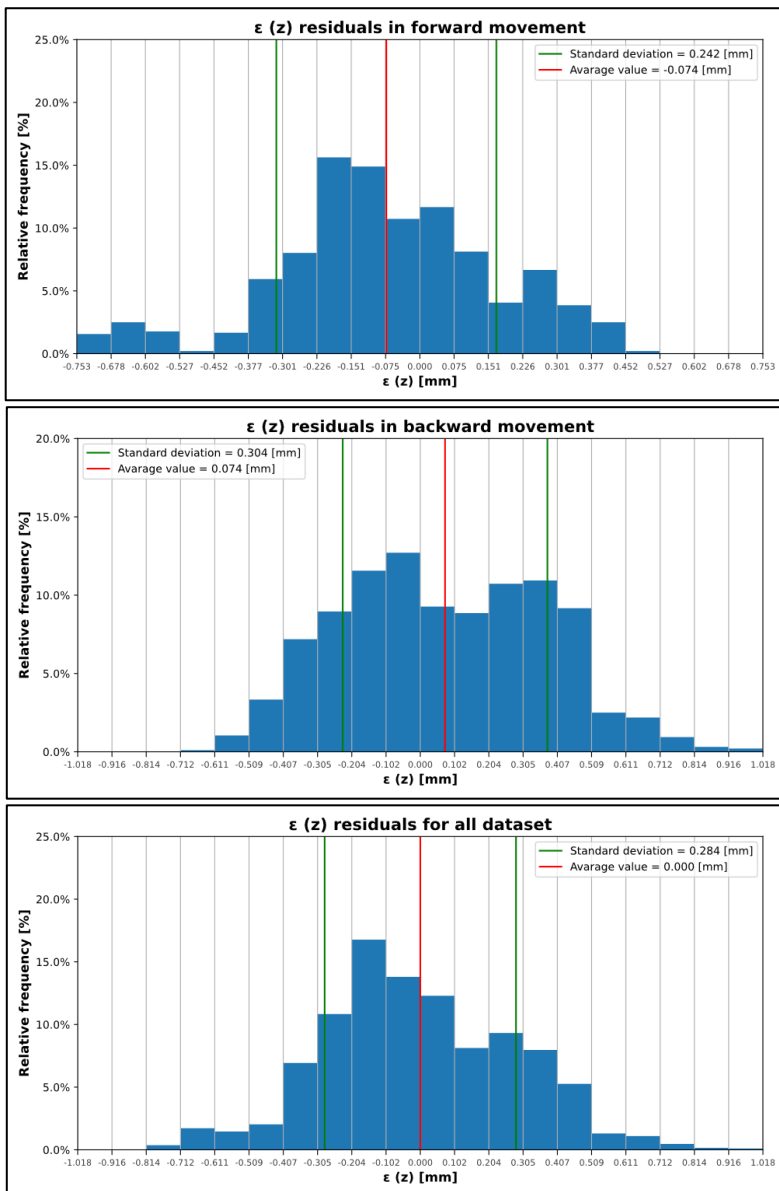


Figure 4-18. Histograms of residuals for forward movement, backward movement and all movement considered simultaneously.



In view of this, only movements in the direction of forward motion are performed for the following tests.

It is possible to see that in each histogram there is not a Gaussian distribution of residuals but a bimodal distribution. So, we need to use a better-performing function for calibration.

### *pol<sub>66</sub>* with optical axis position center

By considering the same dataset a better-performing function is used.

The polynomial model follows the previous one with just two differences:

- now it considers polynomials with exponentials at the sixth also for  $j$ ;
- now the fitting model searches the center of the optical axis to evaluate  $Z$  and  $X$ .

The results are shown in Figure 4-19.

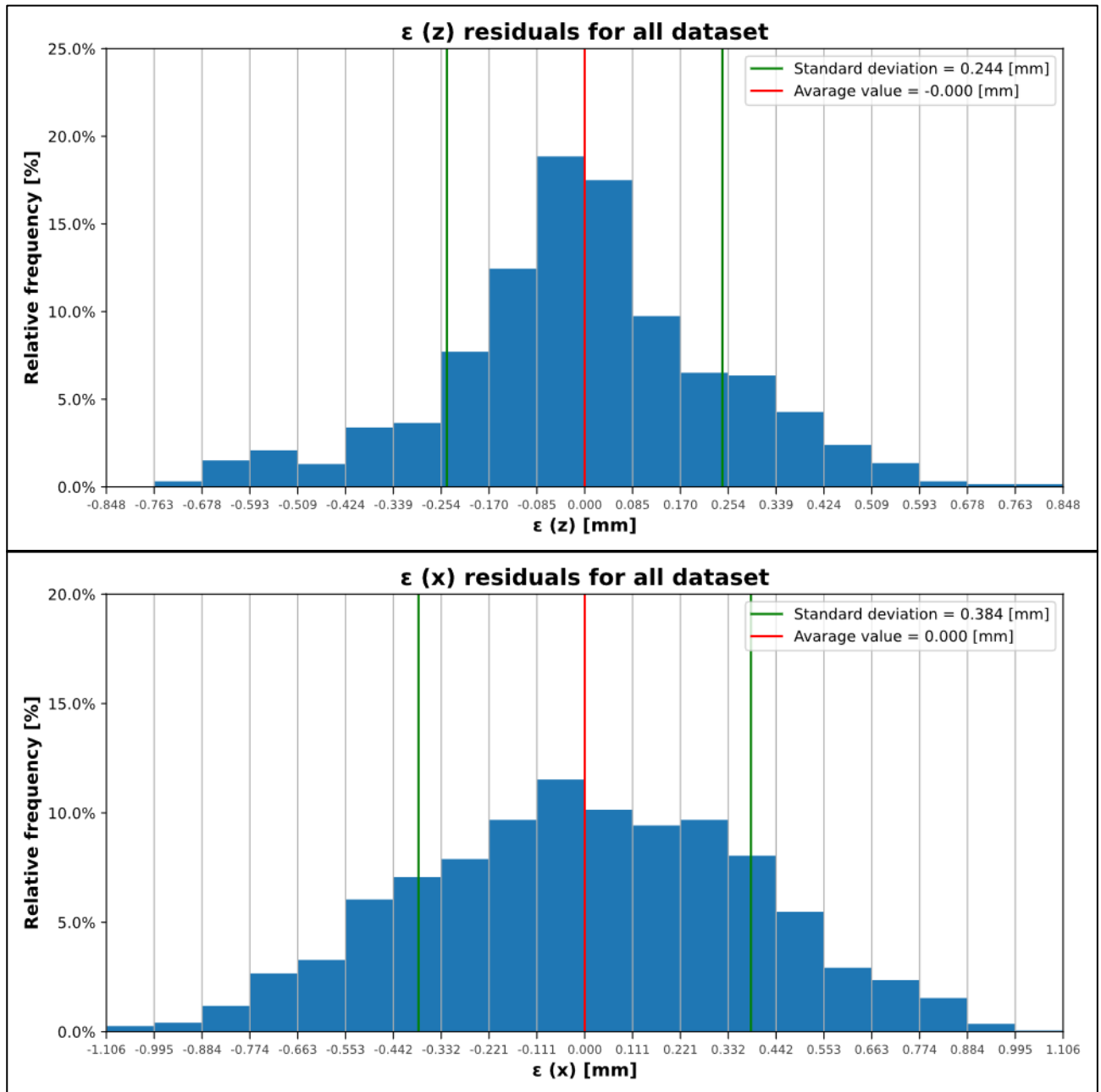


Figure 4-19. New results with a new polynomial model.

This histogram has now a Gaussian distribution than the histogram in Figure 4-18. The standard deviation is reduced for both coordinates.

### 4.4.2 Testing

In this section, we will investigate different camera and optical parameters to evaluate the best combination of parameters to perform measurement.

From now on we will start performing the calibration using the target measured on the CMM which has a greater number of teeth and greater length than the previous one.

#### Combination 0 of parameters

The setting of the test parameters to find peaks are the following:

- N° of steps = 4804;
- F# = 4;
- Accepted angle between first and last tooth  $\leq 0.4^\circ$ ;
- ProfilesPerFrame = 110;
- Exposure time = 10000  $\mu\text{s}$ ;
- nsubpixel = 5.

Figure 4-20 represents the last profile acquired with peaks found.

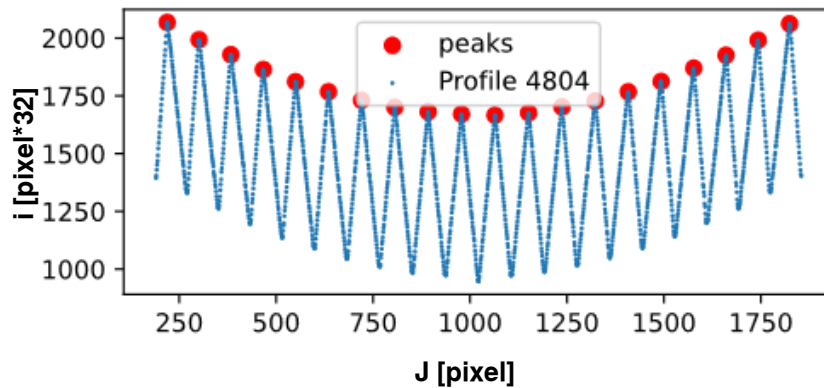


Figure 4-20. Image acquired for the last profile (at Z = -300 mm) and the found peaks.

Looking at Figure 4-20, referring to Figure 2-6, you can also see that the optical system in use produces barrel distortion.

The results of fitting using  $pol_{66}$  are shown in Figure 4-21.

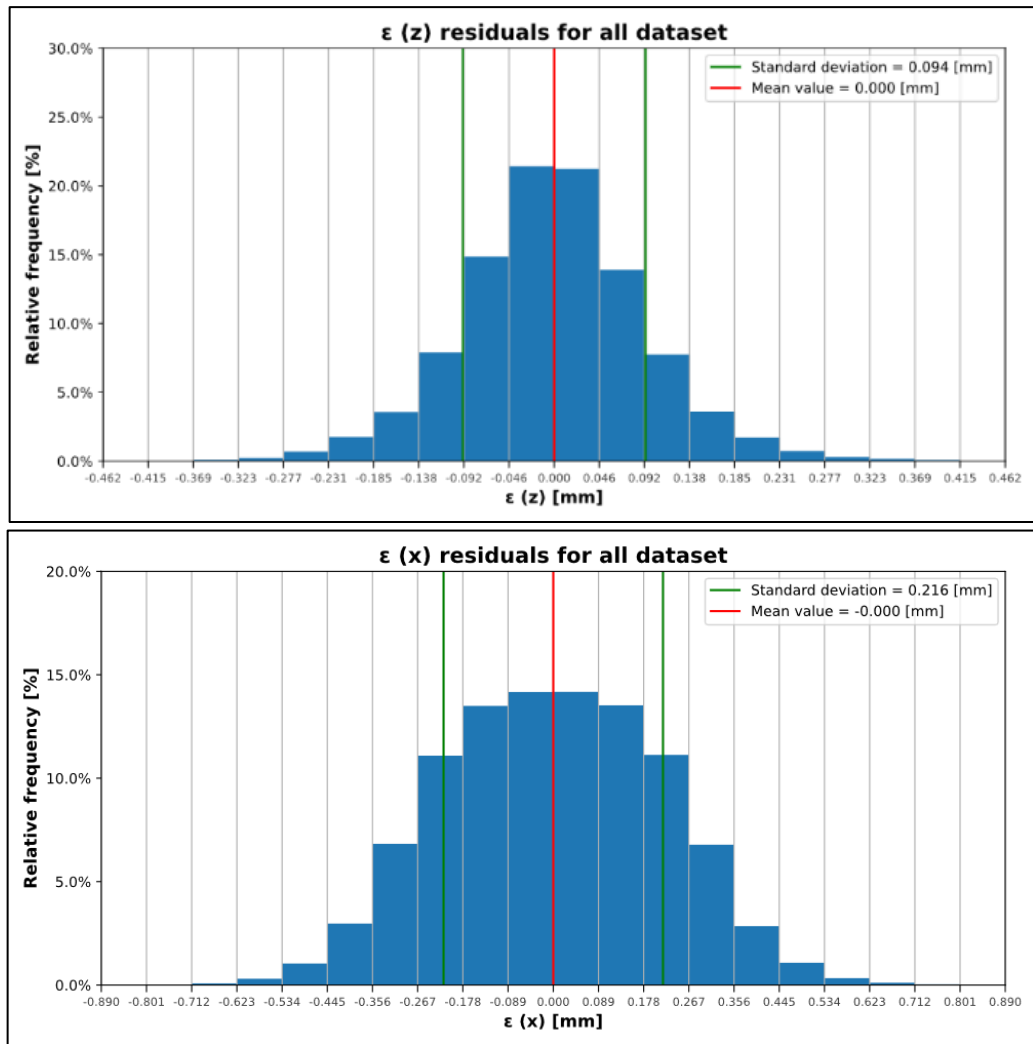


Figure 4-21. Results of finding peaks with CNC machined target.

### Combination 1

Results in Figure 4-22:

- N° of steps = 4801;
- F# = 1.4;
- Accepted angle between first and last tooth  $\leq 0.4^\circ$ ;
- ProfilesPerFrame = 70;
- Exposure time = 6000  $\mu\text{s}$ ;
- nsubpixel = 5.

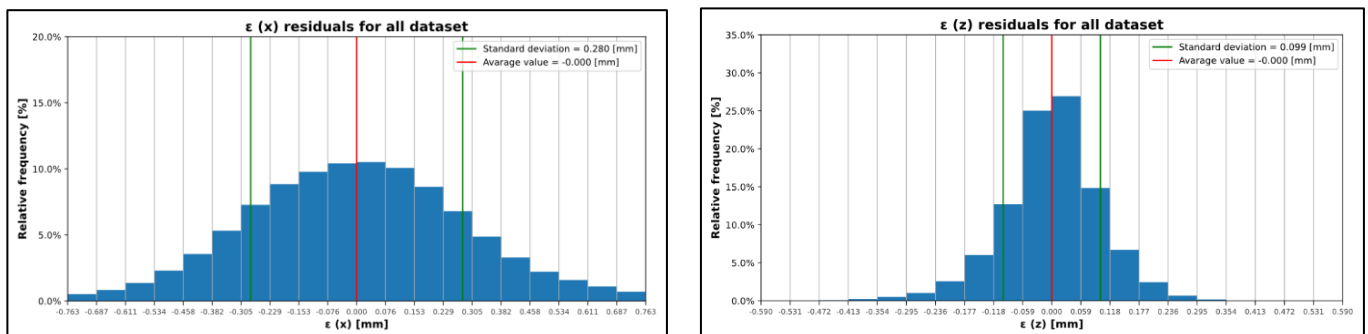


Figure 4-22. Results for combination 1.

## Combination 2

Results in Figure 4-23. This combination of parameters is like combination 0:

- N° of steps = 4801;
- F# = 4;
- Accepted angle between first and last tooth  $\leq 0.4^\circ$ ;
- ProfilesPerFrame = 50;
- Exposure time = 6000  $\mu\text{s}$
- nsubpixel = 5.

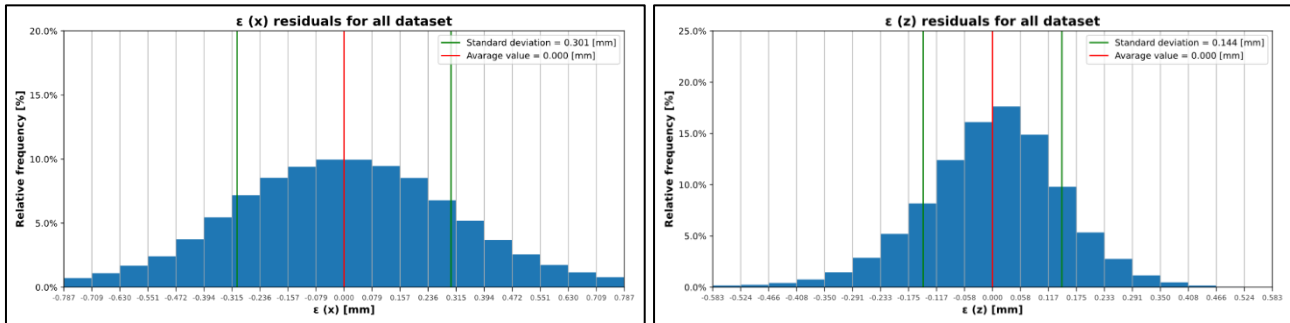


Figure 4-23. Results for combination 2.

The parameter that surely increases accuracy is n° of ProfilesPerFrame (this combination got less n° of profiles than the previous one and the first one).

Also, other parameters not shown in the previous list (because the list would become too long) include MultiSlopeMode (2 points are chosen) and FIR PEAK threshold parameters as shown in Table 4-2.

Table 4-2. Multislope parameters changed.

Parameters changed	Initial test	Other tests
MultiSlopeExposureLimit (1)	60.5 %	80.5 %
MultiSlopeSaturationThreshold (1)	26 %	22 %
MultiSlopeExposureLimit (2)	90.5 %	97.5 %
MultiSlopeSaturationThreshold (2)	20 %	20 %

## 4.5 EFFECT OF FOV – HOW TO ESTABLISH THE NUMBER OF TEETH ACQUIRED

Considering that we are now calibrating using the longest target (1200 mm), when the linear guide is positioned at Z = 300 mm the camera fails to acquire the target completely.

Referring to the Figure 2-9, in the X direction when the target is placed at Z = 300 mm,

$$\text{measuring range length} = 800 \text{ mm} < 1200 \text{ mm} = \text{length of the target.}$$

For this reason, the target we are using now (as mentioned before, the one measured on the CMM) in the initial stages of linear guidance does not entirely enter the camera's field of view.

In Figure 4-24 can be noted that the calibration surfaces consider 20 teeth only after a certain value of the i-th pixel.

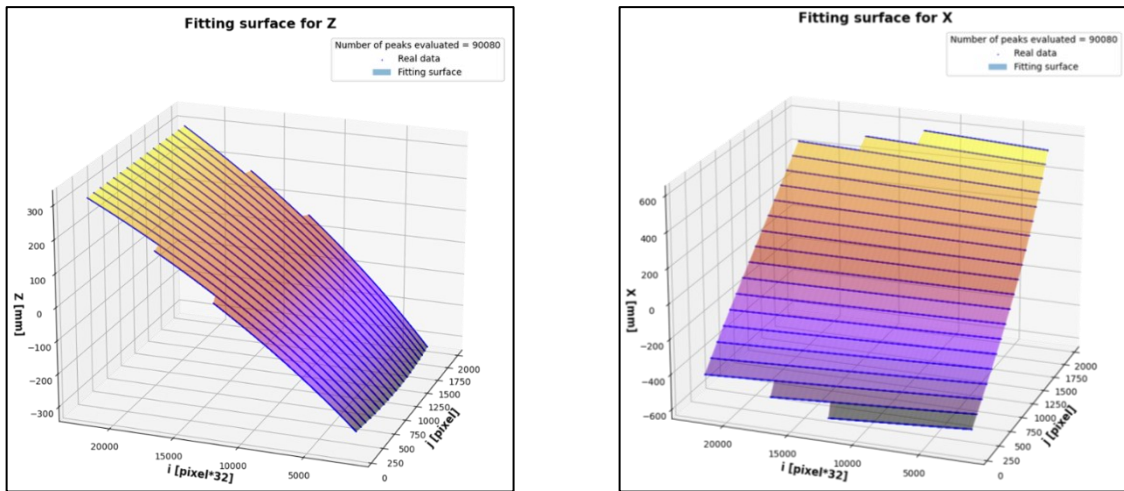


Figure 4-24. Fitting surfaces obtained by gradually increasing the number of teeth.

To obtain these calibration surfaces, first of all we checked in which step of the linear guide the camera was able to acquire all 20 tooth tips and we set all previous profiles as if the camera acquires 18 teeth.

Analogue logic is chosen to find in which step the camera was able to acquire only 16 teeth.

An example. The human eye-based logic chosen is as follows:

1. looking at the profiles obtained during calibration, you can check from which step of the linear guide, the tips of the 20 teeth are acquired entirely (see differences between Figure 4-25 and Figure 4-26);
2. the step found is considered as reference (Figure 4-26);
3. all the previous steps use only 16 teeth for fitting (profile in Figure 4-25 and all profiles before);
4. all steps greater or equal to reference steps use 20 teeth for fitting (Figure 4-26);
5. now we can start checking from which step of the linear guide the tips of the 18 teeth are acquired entirely.

To perform this human eye-based check are required about 5 minutes.

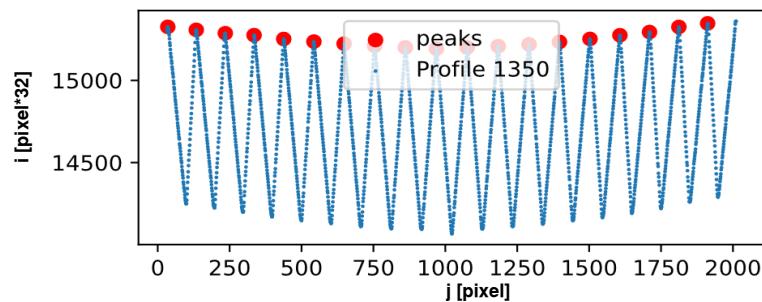


Figure 4-25. Last profile in which all 20 peaks are not acquired.

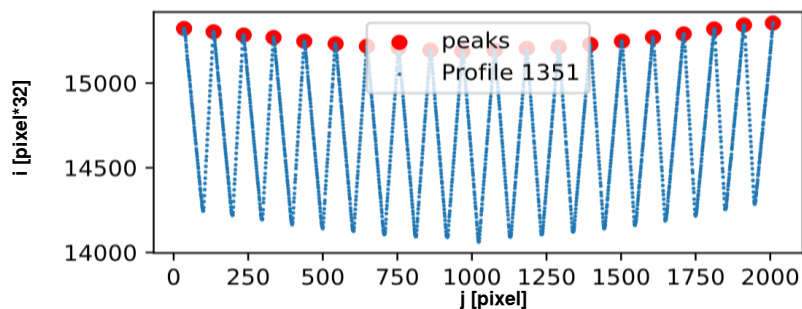


Figure 4-26. First profile in which all 20 peaks are acquired.

### 4.6 CALIBRATION TARGET ISSUES – SPATIAL SAMPLING FREQUENCY

In each graph where there is an evaluation of X residuals, the presence of some pattern that does not have random behaviour (Figure 4-27 and X residual graph in Figure 4-16).

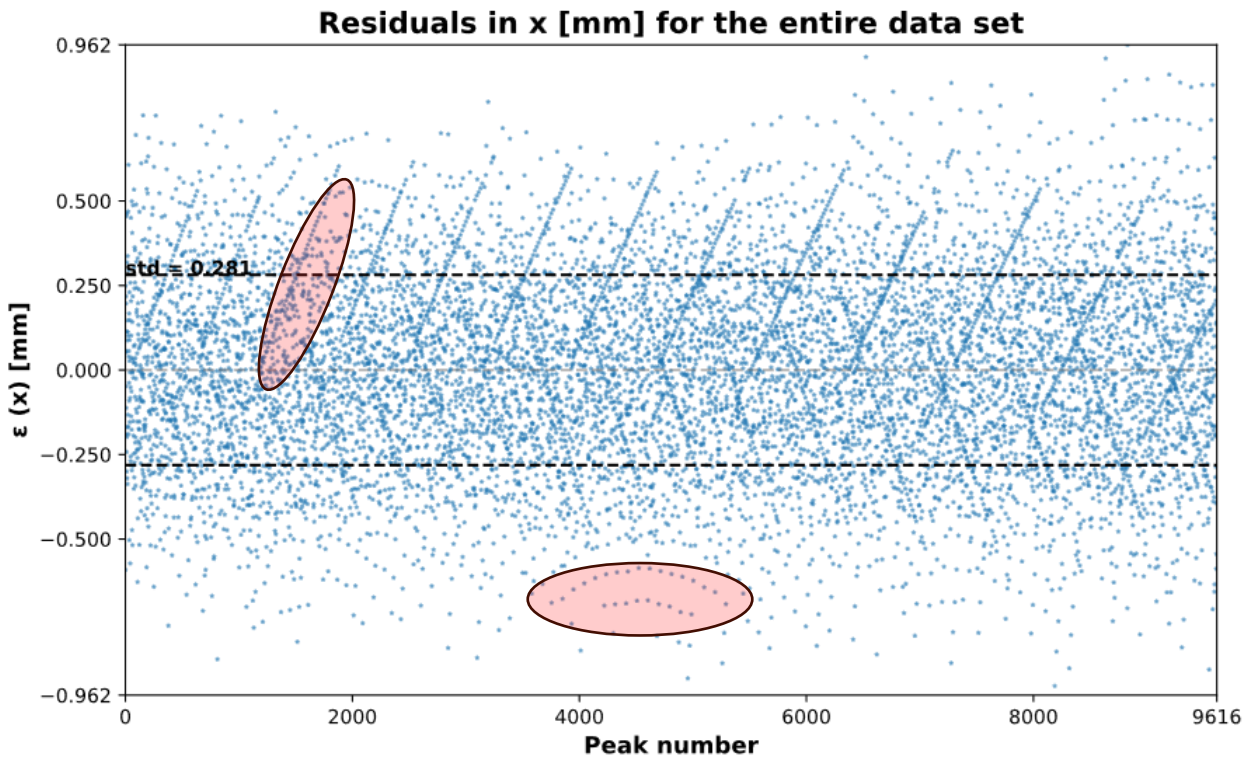


Figure 4-27. Non-random behaviour in X-axis residuals. In this case there are residuals that grow respecting a straight line and other that have parabolic pattern as enlightened in red.

The problem could be the sampling frequency because the tooth has a curvature (Figure 4-4).

Is needed to evaluate the sampling frequency for the sensor when the target is at position Z = 300 mm:

$$\text{Target length} \approx 2048 - (230 * 2) = 1588 \text{ pixels};$$

$$\text{Sampling frequency} = \frac{\text{Target length [mm]}}{\text{Target length [pixels]}} = \frac{800}{1588} \approx 0.5 \frac{\text{mm}}{\text{pixel}}$$

For Z = -300 mm the sampling frequency is reduced.

$$\text{Target length} \approx 2048 - (440 * 2) = 1168 \text{ pixels};$$

$$\text{Sampling frequency} = \frac{\text{Target length [mm]}}{\text{Target length [pixels]}} = \frac{800}{1168} \approx 0.7 \frac{\text{mm}}{\text{pixel}}$$

So, the curvature introduces a possible error in evaluating peaks that can arrive at 0.067 mm when the target is at Z = 300 mm position.

The error can occur at 0.143 mm at the end position of the stage (Z = -300 mm).

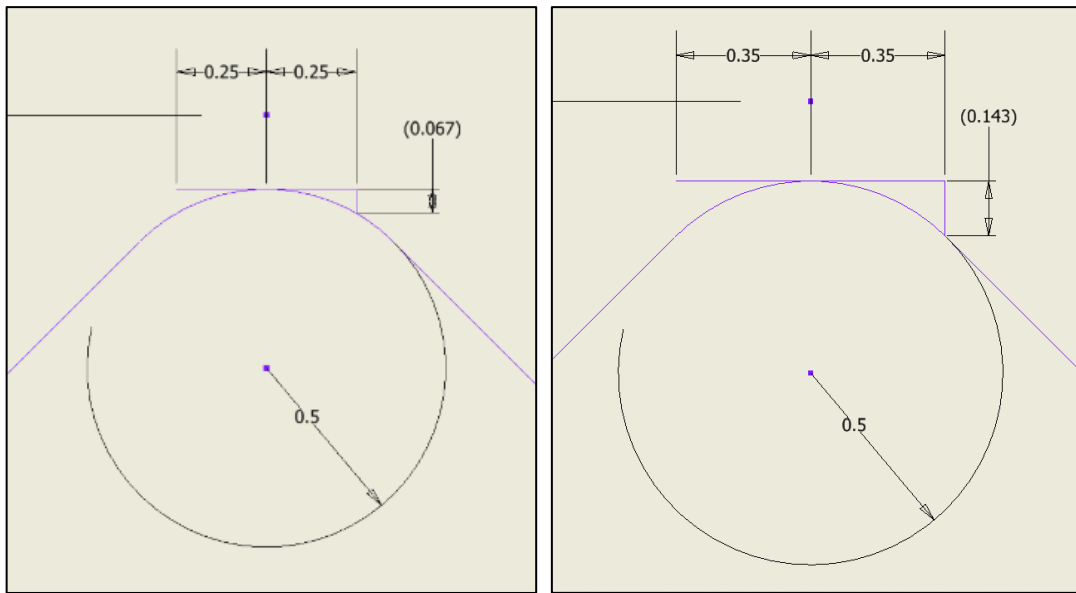


Figure 4-28. Possible error in Z direction given by sampling frequency. If the frequency of sampling is each time the same, this wouldn't be an error. But with the presence of the distortion effects as seen in Figure 4-13, acquiring the upper part considering that sampling frequency is the same in X axis is surely an error.

#### 4.6.1 First solution adopted.

A more robust method should be evaluating the lower part of the tooth because has more radius as shown in Figure 4-4 (the radius raises from 0.5 to 2 mm). The error introduced (Figure 4-29) is now in the range of  $0.008 \div 0.016$  mm.

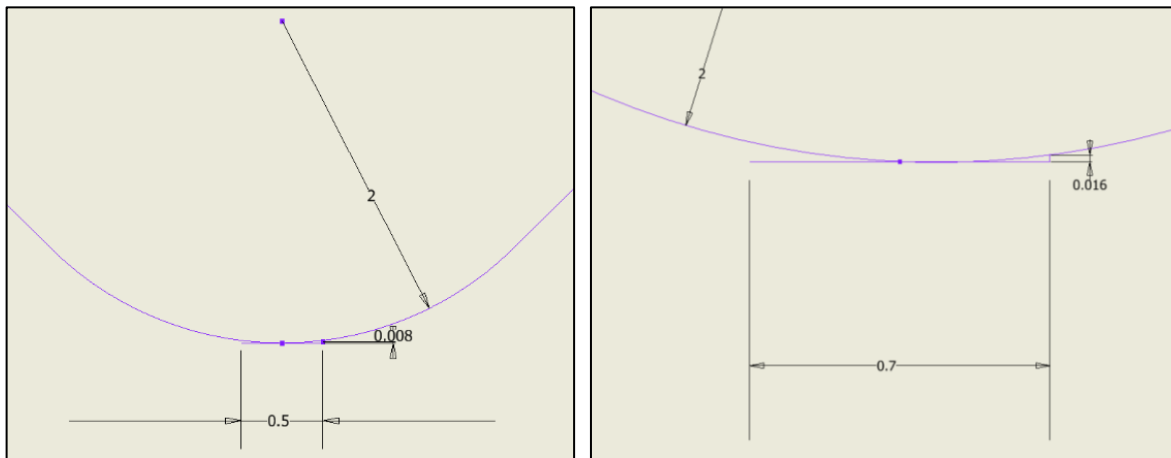


Figure 4-29. Error introduced considering lower part of teeth.

The new dataset for the real-world coordinate of the Z axis is obtained as an average distance between each tooth as in Figure 4-30.

The point  $X = 0$  mm is ignored because the measure has more uncertainty being the junction point.

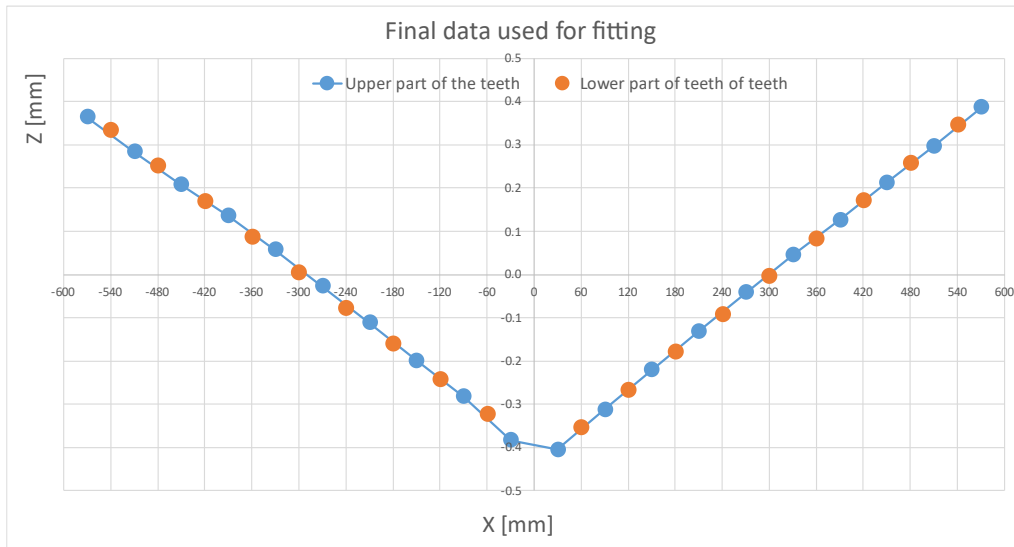


Figure 4-30. The new dataset for Z axis compared to previous one.

By comparing the results between Figure 4-21 and Figure 4-31, the reduction in standard deviation is about 30%.

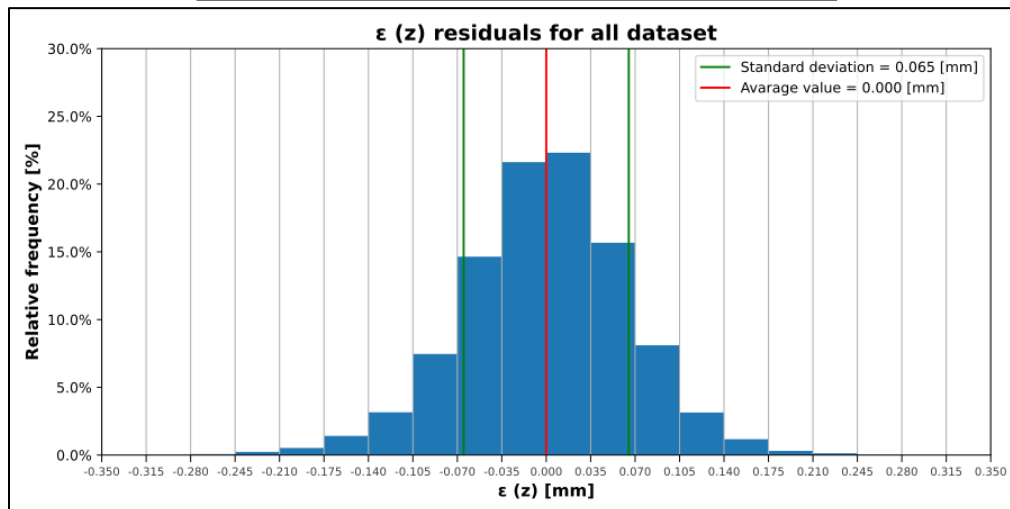
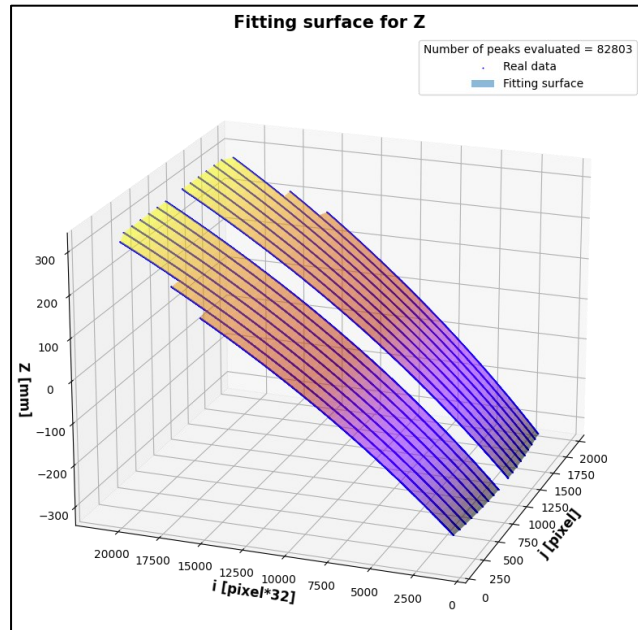


Figure 4-31. New fitting results using lower part of teeth.



It is not the best procedure because:

- the underside of the tooth has a high noise;
- we don't resolve the problem in X direction.

#### 4.6.2 Second solution: using intersections

To follow the strategy chosen at CMM, we can achieve the fitting by ignoring peaks of the signal and using the intersection given by the lines obtained by fitting the points on the sides of the tooth as shown in Figure 4-32.

We can perform a parametric study for the following parameters:

- starting point → point around peak that the algorithm begins to consider for the extraction of the line, ignoring the previous points;
- ending point → point that the algorithm ends to consider;
- X standard deviation;
- Z standard deviation;
- max residuals → max residual found in all the datasets for both axes.

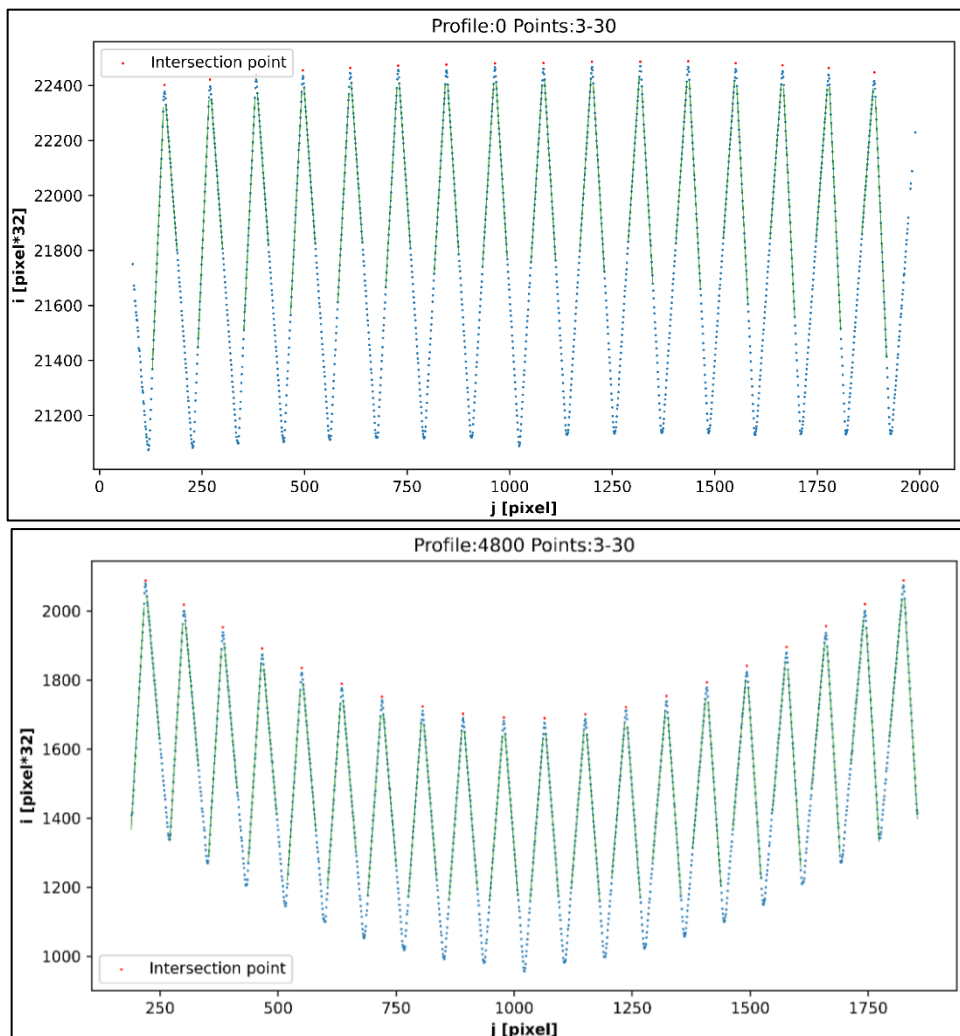


Figure 4-32. Images of interceptions point at the beginning of the linear stage and at the end. For this example, we ignored two points around previous peak and get fitted straight line with points ranged to 3th to 30th for left side and ranged to 3th to 30th for right side.

We ignore points around the found peak and begin the fit to a straight line by setting a start point and an end point, in between which we use the points for the fit to a straight line. The new peak considered is the intersection of the two straight lines obtained from the tooth sides.

Table 4-3 shows how the best results are proportional to the number of points chosen. It's because fitting in straight lines is better with a high number of points.

Table 4-3. Results of calibration using points obtained as interceptions with straightened lines. When solution is not found the cell is left blank.

Start point	End point	X Standard deviation of residuals [mm]	Max X residual [mm]	Z Standard deviation of residuals [mm]	Max Z residual [mm]
2	8	0.079	0.460	0.091	0.916
2	9	0.072	0.447		
2	10	0.066	0.396		
2	11	0.061	0.345		
2	12	0.057	0.273	0.068	0.765
2	13	0.053	0.256		
2	14	0.050	0.253		
2	15	0.048	0.276		
2	16	0.045	0.276	0.055	0.744
2	17	0.043	0.255	0.053	0.751
2	18	0.041	0.244		
2	19	0.040	0.219		
2	20	0.039	0.222	0.048	0.776
2	21	0.037	0.233	0.047	0.786
2	22	0.036	0.244		
2	23	0.035	0.224		
2	24	0.034	0.214		
2	25	0.033	0.197		
2	26	0.032	0.185		
2	27	0.032	0.176	0.041	0.718
2	28	0.031	0.192		
2	29	0.031	0.190	0.040	0.720
2	30	0.030	0.172		
3	8				
3	9	0.089	0.517		
3	10	0.080	0.420	0.090	0.774
3	11	0.073	0.369		
3	12	0.067	0.319		
3	13	0.062	0.303		
3	14	0.058	0.279		
3	15	0.054	0.294		
3	16	0.051	0.279	0.059	0.753
3	17	0.048	0.253		
3	18	0.046	0.239	0.054	0.756
3	19	0.044	0.245	0.053	0.749
3	20	0.042	0.241		
3	21	0.041	0.232		
3	22	0.039	0.241	0.047	0.785
3	23	0.038	0.217	0.046	0.774
3	24	0.036	0.206	0.045	0.762
3	25	0.035	0.187		
3	26	0.034	0.192	0.043	0.731
3	27	0.034	0.184	0.042	0.710
3	28	0.033	0.197	0.041	0.716
3	29	0.033	0.195	0.041	0.715
3	30	0.032	0.174	0.041	0.702

This can be confirmed with the max residual found in X and Z: after the 27<sup>th</sup> point, the max residual grows independently by the chosen starting point. Therefore, by the 28<sup>th</sup> point, the effect of noise starts to grow.

Is shown another effect in Figure 4-32: using the same number of points for the left and right sides of a tooth to perform different lengths of straight line.

This effect is most noticeable in the teeth at the edges of the assembled calibrator.

It is possible to introduce a hybrid procedure: while the difference in length of fitted straight lines between the left and right sides in a tooth is more than 5%, the algorithm must take more points for the straight line that fits in the lateral position where the line has a shorter length.

Figure 4-33 shows the difference in the extraction of straightened lines between the standard and hybrid methods.

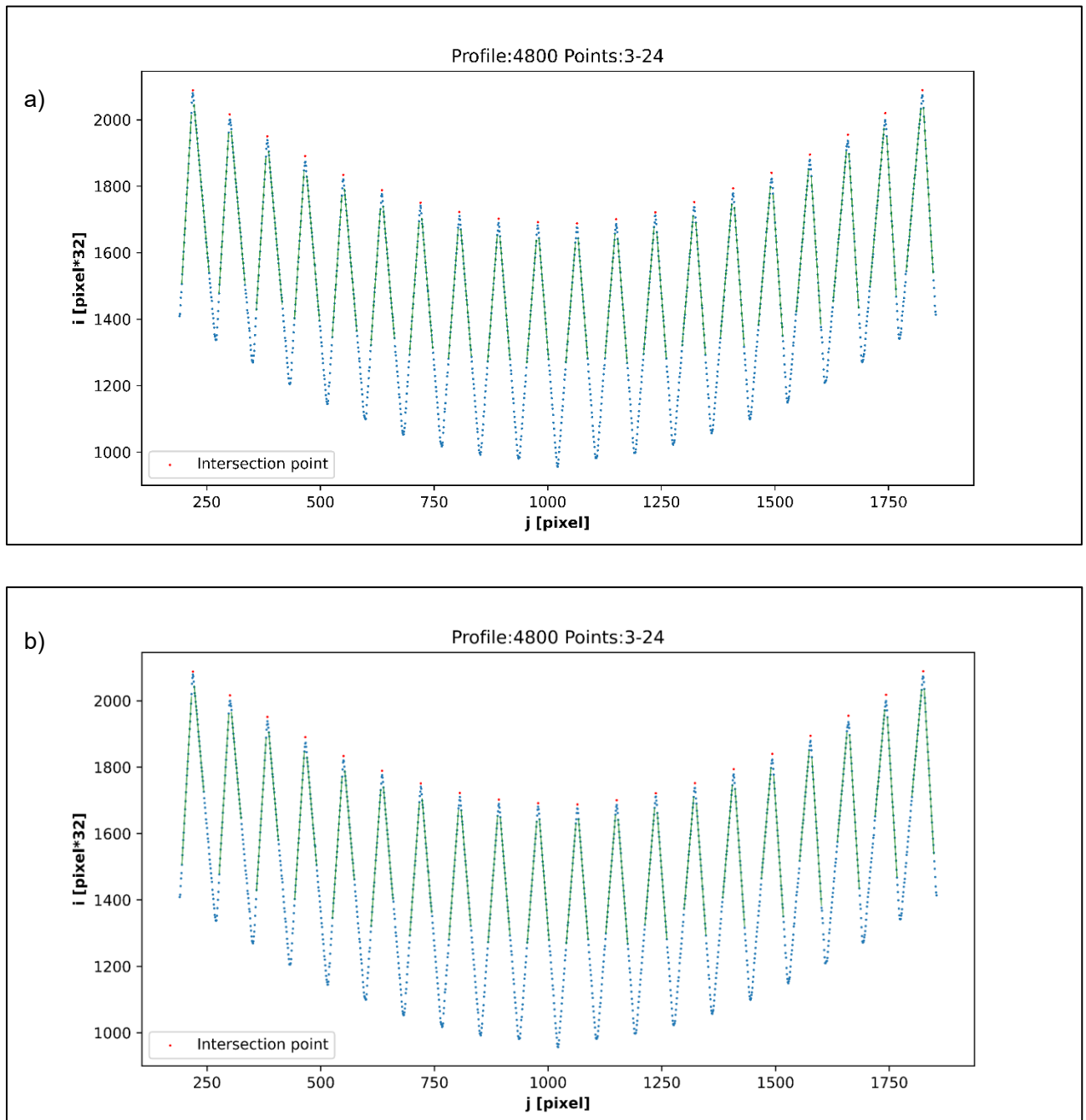


Figure 4-33. In a) we can see the effect for straight lines length with of hybrid method: that lines are longer than lines in b) (normal method with same number of points chosen for both sides of the tooth).

Table 4-4 shows the results of the proposed hybrid method, which performs better accuracy in residuals than results in Table 4-3.

Table 4-4. Results with the hybrid method.

Starting point	Ending point	X Standard deviation of residuals [mm]	Max X residual [mm]	Z Standard deviation of residuals [mm]	Max Z residual [mm]
2	6	0.085	0.541	0.097	0.852
2	7	0.075	0.393	0.087	0.768
2	8	0.067	0.339		
2	9	0.061	0.281		
2	10	0.056	0.278	0.068	0.764
2	11	0.052	0.281		
2	12	0.048	0.244		
2	13	0.046	0.227		
2	14	0.043	0.211	0.054	0.761
2	15	0.041	0.221	0.051	0.780
2	16	0.039	0.203		
2	17	0.037	0.199		
2	18	0.036	0.193		
2	19	0.035	0.189	0.044	0.742
2	20	0.034	0.180	0.043	0.730
2	21	0.033	0.166	0.042	0.729
2	22	0.032	0.161		
2	23	0.031	0.172		
2	24	0.030	0.167	0.039	0.707
2	25	0.029	0.149	0.039	0.704
2	26	0.029	0.154	0.038	0.699
2	27	0.028	0.154	0.038	0.700
2	28	0.028	0.144		
2	29	0.027	0.141		
2	30	0.027	0.163		
3	8	0.084	0.379		
3	9	0.075	0.373		
3	10	0.067	0.314		
3	11	0.061	0.309	0.070	0.744
3	12	0.056	0.320	0.065	0.748
3	13	0.052	0.306		
3	14	0.049	0.258	0.057	0.763
3	15	0.046	0.215		
3	16	0.043	0.238		
3	17	0.041	0.231	0.050	0.769
3	18	0.040	0.217		
3	19	0.038	0.215		
3	20	0.037	0.178	0.045	0.722
3	21	0.035	0.185		
3	22	0.034	0.184		
3	23	0.033	0.166		
3	24	0.032	0.161		
3	25	0.031	0.151		
3	26	0.030	0.151		
3	27	0.030	0.156		
3	28	0.029	0.142		
3	29	0.029	0.140		
3	30	0.028	0.159		

This method removes all patterns as shown in the figure below.

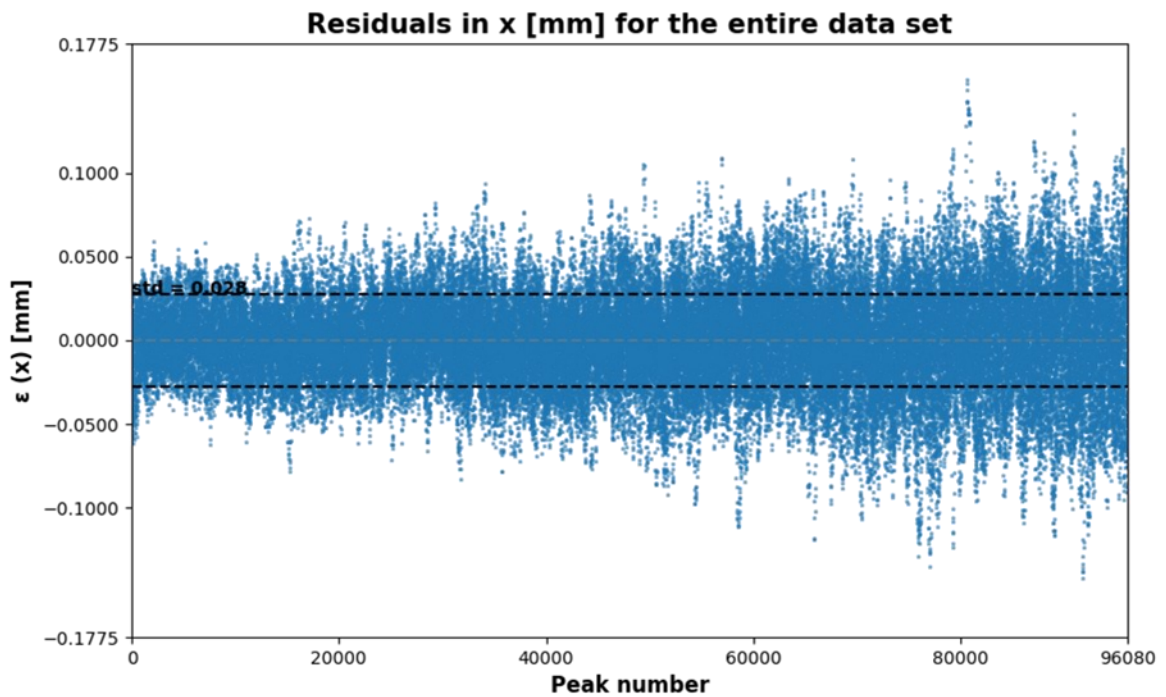


Figure 4-34. Final graph for X residuals. In this graph there aren't patterns.

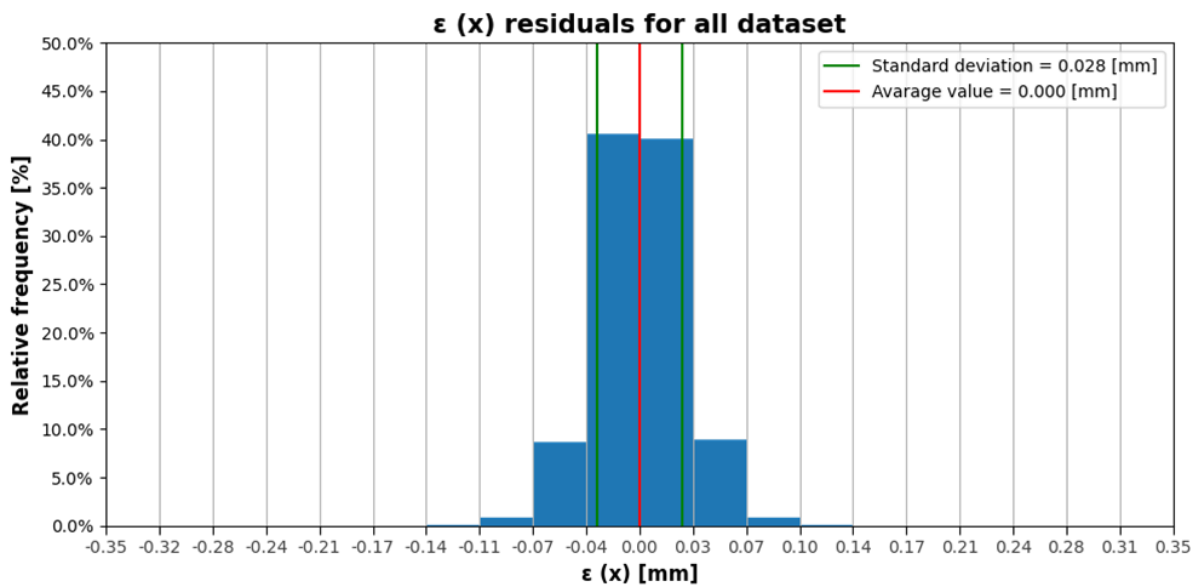


Figure 4-35. Histogram for X residuals.

#### 4.7 PARAMETRIC STUDY ON THE PARAMETER *PROFILES PER FRAME*

In order to choose the optimum number of profiles to be acquired and averaged for each measurement (named ProfilePerFrame), we performed experiments varying this parameter between 1 and 300 (Figure 4-36).

For each value of  $n^\circ$  of profile considered (1-10-20-50-100-300), we computed the standard deviation of the residuals of the regression function for X and Z. In fact, averaging is a statistic approach that tends to eliminate random noise.

We can observe that the residuals decrease with the increase of the number of averaged profiles, however the value of residuals tends to remain constant when the number of profiles per frame overcomes 100.

This means that increasing further the number of profiles does not produce any more advantage. This is why we fixed the number of profiles to 100.

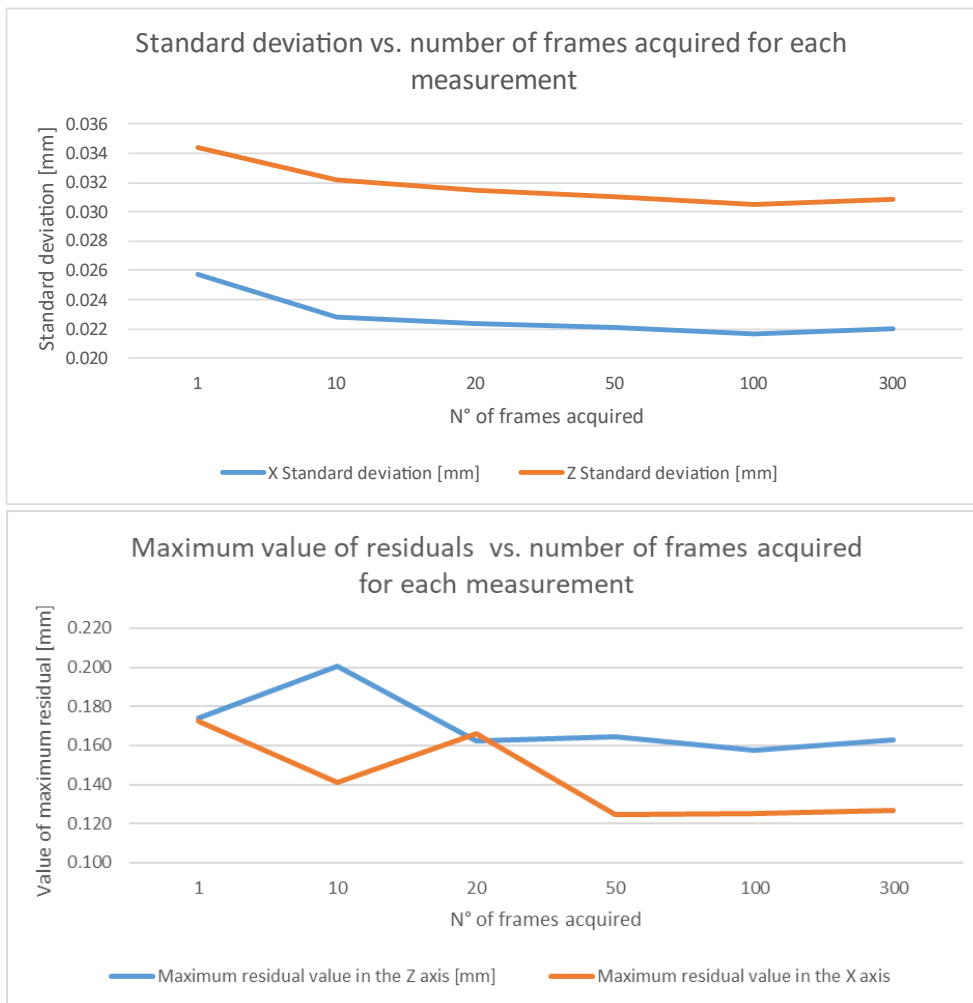


Figure 4-36. Evaluation of the influence of number of frames acquired to extract the profile.

## 5 Results

The methodologies described in the previous chapters were developed and tested for a laser line triangulation sensor realized as a laboratory prototype by assembling laser and camera on an aluminium profile.

Then we have realized the final laser line triangulation sensor, with a support structure made in fiber carbon, that will be used in the project. This new sensor was available only in the last part of my work. However, all the experience made on the laboratory prototype can be used to calibrate this new sensor.

In the following figures we present the results obtained by applying the methodologies for calibration presented above to the final sensor.

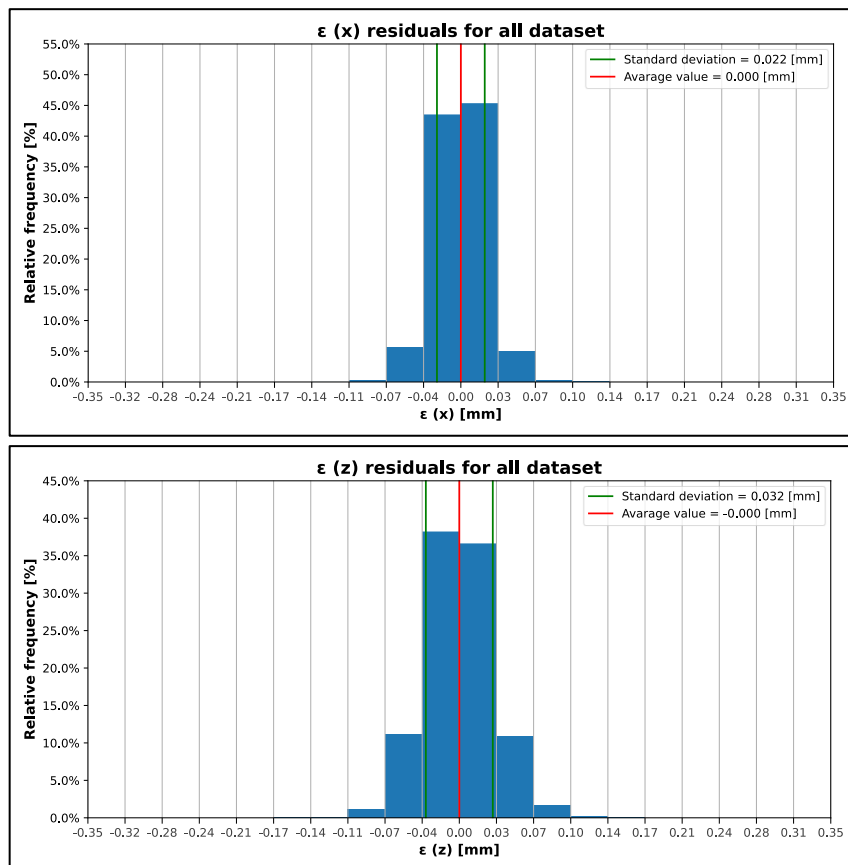


Figure 5-1. Histograms of residuals.

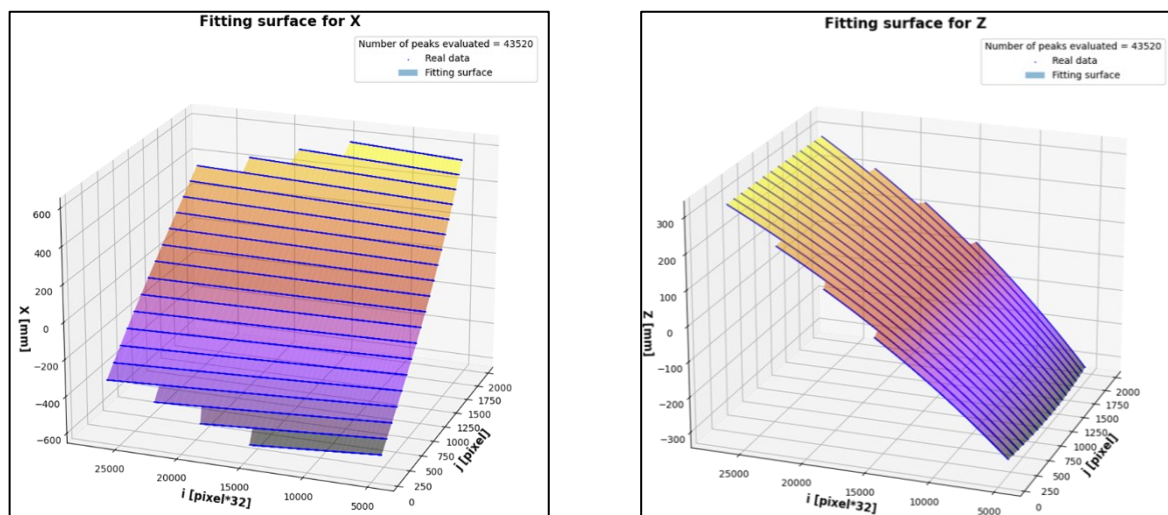


Figure 5-2. Fitting surfaces.

The calibration has been performed with the zig-zag reference artifact and the acquired data have been processed by fitting polynomials and evaluating the quality of the fitting by analysing the residuals, in particular the shape of their distribution and their standard deviation.

The results reached are:

- residuals (Figure 5-1) show a symmetric distribution around the mean, similar to a gaussian distribution – this means that the linear fit has a good quality and only random dispersion is left uncorrected;
- standard deviation in X axis = 0.022 mm – this value means an expanded uncertainty  $U_x = 0.044 \text{ mm}$ , which is more than adequate to the scope;
- maximum value of residuals in X axis = 0.125 mm;
- standard deviation in Z axis = 0.032 mm – this means an expanded uncertainty  $U_z = 0.064 \text{ mm}$ , which is fit for the purpose of resolving deviations from straightness of the order of 0.3 mm, slightly larger than the requirement from the industrial application to resolve deviations of straightness down to 0.2 mm;
- maximum value of residuals in Z axis = 0.158 mm.

**Each measure of a profile is performed in less than 2 seconds.**

The expanded uncertainties  $U_x$  and  $U_z$  that have been computed are the estimate of the calibration uncertainty of the laser line triangulation sensor that has been developed and characterized.

Of course, since the sensor will take measurements on a real industrial environment, on a real steel bar, the uncertainties performance will be larger.

The industrial requirements aim to measure deviations from straightness of the order of 1-2 mm; these values can be certainly measured accurately.

However, the minimum resolution of 0.2 mm cannot be attained. The sensor appears to be able to resolve 0.3 mm, slightly more than what desired.

Considering that the sensor measurement range is very large, in the order of 1000 mm along X and Z directions, such a performance is considered sufficiently good.

An example of a measure on the zig-zag profile is shown in Figure 5-3. With this measure we can see that:

- the distance in the X direction between each tooth is equal to 60 mm, the same distance indicated in its technical drawing;
- the total length of calibration artifact is confirmed to be 1200 mm;
- there is a small corner in the compound calibration artifact, due to both targets not being perfectly aligned as seen at the CMM;
- the height of each tooth corresponds to the height designed in technical drawings.



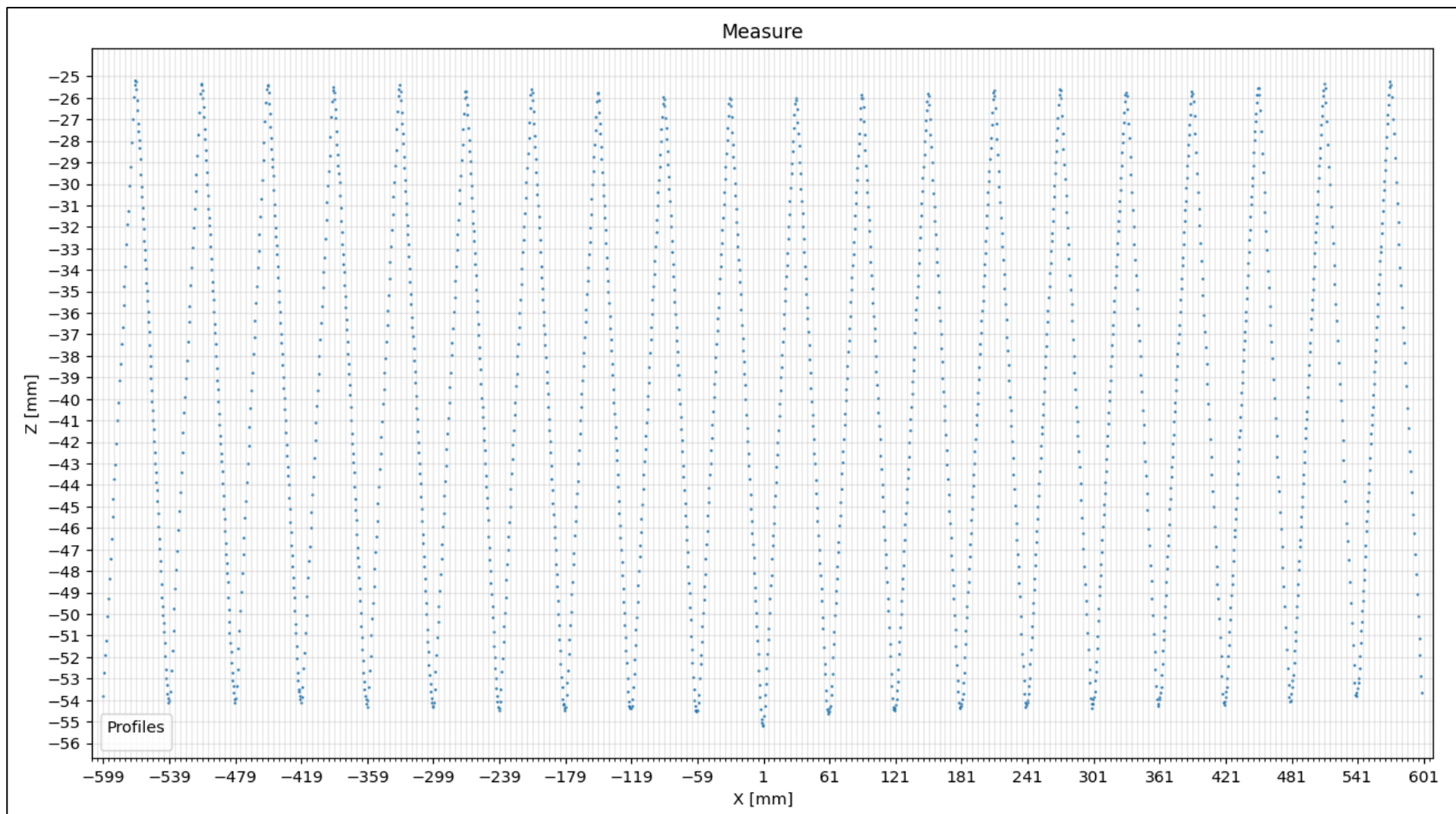


Figure 5-3. Example of measure obtained.

## 6 Further improvements

To build a more precise sensor, further studies are needed on:

- methods that compensate for the non-straightness of the laser line,
- studying a construction and assembly method of optics and laser to guarantee the “*Scheimpflug condition*” which allows to extend the depth of field to the full range of the sensor [7]; applying this condition we obtain that the entire measurement range is in focus regardless of the F#; this condition therefore allows a greater opening of the diaphragm which corresponds to a greater acquired signal.

Such improvements would require the redesign of the sensor, which is not feasible at this point of the project.

However, two improvements are listed below that can be made without increasing the costs of the sensor considerably and which do not require further studies.

### 6.1 IMPROVEMENT N° 1

To perform a complete alignment, **there must be a degree of freedom in a joint (camera or laser) to achieve relative rotation around the Y-axis between the camera and laser.**

This makes it possible to align the optical axis of the camera and the optical axis of the laser (in the Z direction) to make both lie in the same Y-Z plane.

The joint can be found on the market as in Figure 6-1.

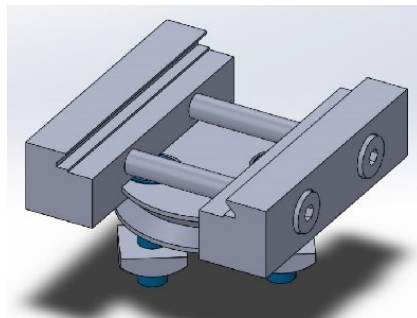


Figure 6-1. Example of joint needed [19].

Currently, however, there isn't this degree of freedom. There is an angle between the two optical axes, and this develops intensity differences between the left and right areas of the optical axis in the pixel array as shown in Figure 6-2.

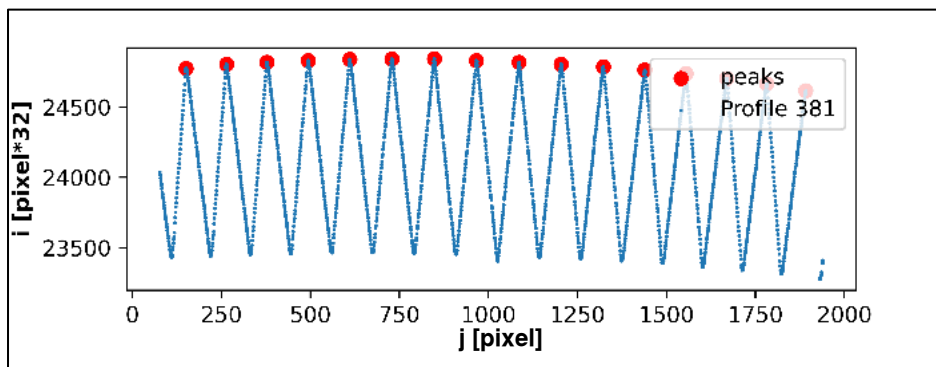


Figure 6-2. Difference in data acquisition between left and right part of the optical axes (there is more light in the left part) caused by the existing angle between camera and laser orientation.

## 6.2 IMPROVEMENT N° 2

To remove the uncertainty in the Z direction introduced by the radius of curvature in the upper part of the teeth, this curvature should be eliminated (Figure 6-3). The tooth tip, instead of being a rounded curve, should be manufactured as a trapezoid.

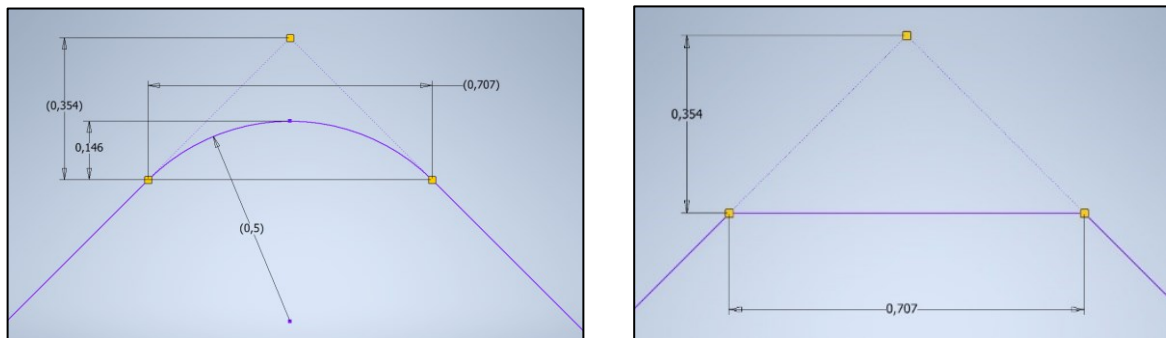


Figure 6-3. Actual calibrator measures on the left and proposed change on the right.

Eliminating the curvature does not change anything for the X-axis because this one can still be obtained as the intersection of the straight lines obtained from the sides of the teeth.

## 7 Conclusions

Quality control for prismatic bars at the entrance of the production line is necessary to ensure that at the end of the line, there are suspensions conformal with specifications. This quality control reduces process costs, material costs and warranty costs.

Carrying out quality control for 100% of the bars entering the production line is possible only with a sensor that takes measurements fast, precise and for a wide range of lengths.

The characteristics and the purpose of the measurement are perfectly suited to the use of a laser triangulation sensor.

Initially, it was necessary to find the best parameters, both optical and CMOS, to see the center of the laser line without errors and non-uniqueness.

Subsequently, we moved on to preparing the calibration which led us to make some considerations.

The first consideration regarding the toothed target is that to obtain a correct calibration, correct alignment is required. Afterwards, some tests were performed to evaluate the best polynomial to use for the fitting.

At this point, we realized the presence of uncertainty due to the sampling frequency which is not high enough to correctly acquire data on the top of the tooth, where there is a radius of curvature.

The most performing method turned out is to fit output data as the intersections of the lines obtained from line regression of the points acquired on the sides of the tooth.

The result was the achievement of a sensor that has much better accuracy than similar instruments already present in the literature. In fact, with our expanded uncertainty  $U = 2\sigma = 0.06 \text{ mm}$ , we can confirm this sentence:

$$0.06 \text{ mm} \ll 1.5 \text{ mm} = \text{accuracy at 1 m working distance in literature [6]}.$$

From the standard UNI ISO/TR 14253-6:2017, the recommendation for the instrument in a quality control station is a minimum TUR (Tolerance Uncertainty Ratio)  $\geq 4$ :

$$TUR \geq 4 = \frac{T}{U} = \frac{T}{0.06}$$

Therefore, the non-straightness tolerance interval accepted in the design by VDLWEW should be:

$$T = U * TUR = 0.24 \text{ mm}$$

that approximated at first decimal, will result in a tolerance interval zone of 0.2 mm, as VDLWEW required to measure non straightness of the bar. If we desire more confidence, better is to impose TUR should reach TUR=5; this means that the sensor, in its actual realization, has an uncertainty of 0.3 mm; slightly larger than required.

The best performance for the measure is obtained when TUR = 10 (UNI ISO/TR 14253-7:2021). Probably, by combining the process obtained during the work of this thesis with further improvements, the accuracy of laser line triangulation technology can be better and reach TUR = 10.

This technology, being accurate and performing rapid measurements, has the potential to become the leading technology for inline quality control for objects of all sizes.

## 8 Index of figures

FIGURE 2-1. TRAILING-ARM SUSPENSION PRODUCED BY VDLWEW [20].	2
FIGURE 2-2. A PRISMATIC-SHAPED BAR IS PLACED AT THE TOP OF THE IMAGE WITH ITS LONGITUDINAL AXIS IN RED. THE BARS PRESENT UNDER THE FIRST ARE OBTAINED AFTER INTERMEDIATE BENDING STEPS BEFORE OBTAINING THE FINAL SUSPENSION IN FIGURE 2-1.	2
FIGURE 2-3. SCHEMATIC REPRESENTATION OF THE ELEMENTS OF A SINGLE PROCESS FROM ISO 9001 [21].	3
FIGURE 2-4. LASER LINE TRIANGULATION SCHEME [7].	4
FIGURE 2-5. SCHEME TO OBTAIN 1 DIMENSIONAL MEASUREMENT [34].	4
FIGURE 2-6. DIFFERENCE BETWEEN PINCUSHION AND BARREL DISTORTION ON THE LEFT [23]. EXAMPLE OF BARREL DISTORTION ON RIGHT, FROM <a href="https://help.shopmoment.com/article/181-superfish-distortion-correction">HTTPS://HELP.SHOPMOMENT.COM/ARTICLE/181-SUPERFISH-DISTORTION- CORRECTION</a> [24].	5
FIGURE 2-7. DIFFERENCES IN DEPTH OF FIELD VS. APERTURE.	5
FIGURE 2-8. FINAL CONFIGURATION OF THE SENSOR.	6
FIGURE 2-9. MEASURING FIELD OF DESIGNED SENSOR. O(X,Y) = (0,0) REPRESENT THE ORIGIN OF MEASUREMENT COORDINATE SYSTEM.	6
FIGURE 2-10. NORMAL DISTRIBUTION OF GAUSS [17].	7
FIGURE 2-11. REPRESENTATION OF A MEASUREMENT SYSTEM.	8
FIGURE 2-12. THE MODEL USED IN A MEASUREMENT SYSTEM.	8
FIGURE 3-1. LASER PLANE SOURCE [2]. THE RED GRAPH IS A REPRESENTATION OF THE LASER LINE SOURCE INTENSITIES ALONG THE LINE PERPENDICULAR TO THE OPTICAL AXIS OF THE LASER.	11
FIGURE 3-2. MODULATION OF LASER INTENSITIES (Y-AXIS) AS THE VOLTAGE (X-AXIS) INCREASES. THE MODEL USED IS RS. IMAGE TAKEN FROM DATASHEET [2].	11
FIGURE 3-3. IN GREEN LASER PLANE PRODUCED, IN RED WHAT THE CAMERA CAN SEE.	11
FIGURE 3-4. LASER PROFILE ENERGY COMPARED TO WHAT IS SHOWN BY THE SENSOR.	12
FIGURE 3-5. SETUP OF THE EXPERIMENT.	12
FIGURE 3-6. THE ARCHITECTURE OF A TWO-DIMENSIONAL CMOS IMAGE SENSOR. IMAGE TAKEN FROM [28].	13
FIGURE 3-7. A REPRESENTATION OF A PIXEL [28].	13
FIGURE 3-8. THE POINT 1 IN THE IMAGE, WHICH HAS SATURATION, HAS THE HIGHEST $\phi_p$ , IN FACT IT HAS THE HIGHEST ANGULAR COEFFICIENT IN THE GRAPH THAT SHOWS THE INTENSITY VS EXPOSURE TIME. IN THIS EXAMPLE WE HAVE $\phi_{p1} > \phi_{p2} > \phi_{p3}$ .	14
FIGURE 3-9. SENSOR SPECTRAL RESPONSE (IMAGE FROM CAMERA DATASHEET CITED IN [1]).	14
FIGURE 3-10. SCHEME THAT EXPLAINS UTILIZATION OBJECTIVE OF MULTI SLOPE MODE.	15
FIGURE 3-11. EXAMPLE OF USING KNEE POINTS FOR MULTI SLOPE MODE (IMAGE FROM CAMERA DATASHEET [1]).	16
FIGURE 3-12. MAXIMUM INTENSITY PROFILE MODE.	17
FIGURE 3-13. THE THRESHOLD MODE (TRSH).	18
FIGURE 3-14. THE CENTER OF GRAVITY MODE (COG).	18
FIGURE 3-15. TRANSFORMATION FROM GAUSSIAN INTENSITIES TO FIRST DERIVATIVE.	19
FIGURE 3-16. REFERENCE SYSTEM CONSIDERED. J FACING RIGHT AND I FACING DOWN	19
FIGURE 3-17. VECTOR EXTRACTED FROM THE ALGORITHM.	19
FIGURE 3-18. FINAL FRAME AFTER ACQUISITION. EVERY SINGLE ROW IS EQUIVALENT TO A PROFILE IDENTIFIED WITH ONE OF THE ALGORITHMS SEEN ABOVE.	20
FIGURE 3-19. AVERAGE PROFILE FINAL VECTOR.	20
FIGURE 3-20. IMAGE SHOWING 5 PROFILES (A) AND THEIR AVERAGE VALUE (B). THE DOWNWARD LINES IN (B) ARE PRODUCED BY AVERAGING BETWEEN ONE OR MORE HIGH VALUES AND A FEW ZEROS.	20
FIGURE 3-21. OBJECTIVE MOUNTED ON THE CAMERA. THE SCREW ON THE LEFT IS USED TO CHANGE THE FOCUS, AND THE SCREW ON THE RIGHT IS USED TO CHANGE THE APERTURE [32].	21
FIGURE 3-22. EVALUATION OF THE INTENSITY OF PIXELS ON A VERTICAL LINE TO OBTAIN THE BEST FOCUS. IN IMAGE (A) IT CAN BE SEEN A LARGE WIDTH IN THE GAUSSIAN OF THE LASER BEAM. IT IS ALSO POSSIBLE TO SEE A BIMODAL INTENSITY EFFECT INDICATING THE DIVERGENCE OF THE LASER BEAM (THE FOCUS POINT HAS BEEN PASSED). IN THE SECOND IMAGE (B) IS SHOWN THE EFFECT OF THE GOOD FOCUS. DURING THIS PROCEDURE OTHER PARAMETERS MUST NOT CHANGE.	22

FIGURE 3-23. IMAGE ACQUIRED WITH CHOSEN PARAMETERS ON THE TOP. ON LEFT THE HISTOGRAM THAT SHOWS INTENSITY FREQUENCY TO THE ENTIRE ACQUIRED IMAGE. ....	23
FIGURE 4-1. GEOMETRY OF COMMERCIAL TARGET. ....	25
FIGURE 4-2. REVIEW OF MOST USED CALIBRATION TARGETS (IMAGE TAKEN FROM [3]). ....	25
FIGURE 4-3. TARGET BUILT WITH FDM PROCESS WITH LASER BEAM PROJECTED. ....	26
FIGURE 4-4. ON THE TOP, THERE IS A 3D REPRESENTATION OF A SINGLE CALIBRATION TARGET. DIMENSIONS OF THE SINGLE TOOTH OF THE TARGET ON THE LEFT, WHERE THERE IS THE POINT OBTAINED AS THE INTERSECTION GIVEN BY THE LINES OBTAINED FROM THE SIDES OF THE TOOTH. ON THE RIGHT, THERE IS A PHOTO OF THE TARGETS COUPLED TO THE CMM. ....	26
FIGURE 4-5. THE MEASURED TARGET VS ROTATED TARGET. ....	27
FIGURE 4-6. COORDINATES USED FOR FITTING. ....	28
FIGURE 4-7. REFERENCE COORDINATES. ....	28
FIGURE 4-8. IN TOP SENSOR MATRIX ROTATED (NOT ALIGNED) VS ALIGNED MATRIX. BELOW THERE IS AN IMAGE TAKEN IN THE BASE PROGRAM OF THE SENSOR. IN THIS CASE WE PERFORMED ALIGNMENT SHOOTING LASER TO THE WALL. FOR THE FOLLOWING TEST WE WILL USE A BAR THAT OLDS THE TARGET. ....	29
FIGURE 4-9. CHECKING THE CENTER IN X AXIS. ....	30
FIGURE 4-10. CHECKING THE ANGLE BETWEEN X AND Z AXES (B). IN THIS CASE THE ANGLE (IN PIXELS) IS TOO HIGH. ....	30
FIGURE 4-11. AT THE LEFT PHOTO WE CAN SEE THAT LASER BEAM DIVERGES AFTER PASSING THROUGH THE JOINT POINT. IN THE RIGHT PHOTO THE BEAM DOESN'T DIVERGE. ....	31
FIGURE 4-12. CALIBRATION SEQUENCE. ....	32
FIGURE 4-13. ACQUIRED IMAGE OF THE FIRST PROFILE AT Z = 300 [MM] USING A TARGET WITH LENGTH. ....	33
FIGURE 4-14. CALIBRATION PROCESS DIAGRAM BLOCK. ALIGNMENT PROCESS IS EXPLAINED IN 0. ....	33
FIGURE 4-15. CALIBRATION SURFACE AND REAL DATA POINTS. ....	34
FIGURE 4-16. RESIDUALS IN Z AXIS (UPPER GRAPH) AND X AXIS (LOWER GRAPH). ....	35
FIGURE 4-17. EXPLANATION OF HOW IS BUILT THE GRAPH OF RESIDUALS USING INCREMENTAL PEAK NUMBER. ....	36
FIGURE 4-18. HISTOGRAMS OF RESIDUALS FOR FORWARD MOVEMENT, BACKWARD MOVEMENT AND ALL MOVEMENT CONSIDERED SIMULTANEOUSLY. ....	36
FIGURE 4-19. NEW RESULTS WITH A NEW POLYNOMIAL MODEL. ....	37
FIGURE 4-20. IMAGE ACQUIRED FOR THE LAST PROFILE (AT Z = -300 MM) AND THE FOUND PEAKS. ....	38
FIGURE 4-21. RESULTS OF FINDING PEAKS WITH CNC MACHINED TARGET. ....	39
FIGURE 4-22. RESULTS FOR COMBINATION 1. ....	39
FIGURE 4-23. RESULTS FOR COMBINATION 2. ....	40
FIGURE 4-24. FITTING SURFACES OBTAINED BY GRADUALLY INCREASING THE NUMBER OF TEETH. ....	41
FIGURE 4-25. LAST PROFILE IN WHICH ALL 20 PEAKS ARE NOT ACQUIRED. ....	41
FIGURE 4-26. FIRST PROFILE IN WHICH ALL 20 PEAKS ARE ACQUIRED. ....	41
FIGURE 4-27. NON-RANDOM BEHAVIOUR IN X-AXIS RESIDUALS. IN THIS CASE THERE ARE RESIDUALS THAT GROW RESPECTING A STRAIGHT LINE AND OTHER THAT HAVE PARABOLIC PATTERN AS ENLIGHTENED IN RED. ....	42
FIGURE 4-28. POSSIBLE ERROR IN Z DIRECTION GIVEN BY SAMPLING FREQUENCY. IF THE FREQUENCY OF SAMPLING IS EACH TIME THE SAME, THIS WOULDN'T BE AN ERROR. BUT WITH THE OF PRESENCE OF THE DISTORTION EFFECTS AS SEEN IN FIGURE 4-13, ACQUIRING THE UPPER PART CONSIDERING THAT SAMPLING FREQUENCY IS THE SAME IN X AXIS IS SURELY AN ERROR. ....	43
FIGURE 4-29. ERROR INTRODUCED CONSIDERING LOWER PART OF TEETH. ....	43
FIGURE 4-30. THE NEW DATASET FOR Z AXIS COMPARED TO PREVIOUS ONE. ....	44
FIGURE 4-31. NEW FITTING RESULTS USING LOWER PART OF TEETH. ....	44
FIGURE 4-32. IMAGES OF INTERCEPTIONS POINT AT THE BEGINNING OF THE LINEAR STAGE AND AT THE END. FOR THIS EXAMPLE, WE IGNORED TWO POINTS AROUND PREVIOUS PEAK AND GET FITTED STRAIGHT LINE WITH POINTS RANGED TO 3TH TO 30TH FOR LEFT SIDE AND RANGED TO 3TH TO 30TH FOR RIGHT SIDE. ....	45
FIGURE 4-33. IN A) WE CAN SEE THE EFFECT FOR STRAIGHT LINES LENGTH WITH OF HYBRID METHOD: THAT LINES ARE LONGER THAN LINES IN B) (NORMAL METHOD WITH SAME NUMBER OF POINTS CHOSEN FOR BOTH SIDES OF THE TOOTH). ....	47
FIGURE 4-34. FINAL GRAPH FOR X RESIDUALS. IN THIS GRAPH THERE AREN'T PATTERNS. ....	49
FIGURE 4-35. HISTOGRAM FOR X RESIDUALS. ....	49
FIGURE 4-36. EVALUATION OF THE INFLUENCE OF NUMBER OF FRAMES ACQUIRED TO EXTRACT THE PROFILE. ....	50

FIGURE 5-1. HISTOGRAMS OF RESIDUALS. ....	51
FIGURE 5-2. FITTING SURFACES. ....	51
FIGURE 5-3. EXAMPLE OF MEASURE OBTAINED. ....	53
FIGURE 6-1. EXAMPLE OF JOINT NEEDED [19]. ....	54
FIGURE 6-2. DIFFERENCE IN DATA ACQUISITION BETWEEN LEFT AND RIGHT PART OF THE OPTICAL AXES (THERE IS MORE LIGHT IN THE LEFT PART) CAUSED BY THE EXISTING ANGLE BETWEEN CAMERA AND LASER ORIENTATION. ....	54
FIGURE 6-3. ACTUAL CALIBRATOR MEASURES ON THE LEFT AND PROPOSED CHANGE ON THE RIGHT. ....	55

## 9 Index of tables

Table 4-1. CMM coordinates of the upper part of teeth.....	27
Table 4-2. Multislope parameters. ....	41
Table 4-3. Results of calibration using points obtained as interceptions with straightened lines. When solution is not found the cell is left blank.....	47
Table 4-4. Results with hybrid method. ....	49



## 10References

- [1] “Upgrade from C5 to C6,” *AT ProductDocumentation*.  
<https://docs.automationtechnology.de/products3d/knowledgebase/upgrade/#subpixel-and-coordinate-scale> (accessed Oct. 02, 2023).
- [2] Osela, *STREAMLINE LASER*. 2016. [Online]. Available: <https://www.osela.com/wp-content/uploads/2020/10/Streamline-Laser-system-2016.pdf>
- [3] X. Zhang and J. Zhang, “Summary on calibration method of line-structured light sensor,” in *2017 IEEE International Conference on Robotics and Biomimetics (ROBIO)*, Dec. 2017. Accessed: Oct. 03, 2023. [Online]. Available: <http://dx.doi.org/10.1109/robio.2017.8324571>
- [4] CHEN Tian-fei, MA Zi, and WU Xiang, “Calibration of light plane in line structured light sensor based on active vision,” *Optics and Precision Engineering*, vol. 20, no. 2, pp. 256–263, 2012, doi: 10.3788/ope.20122002.0256.
- [5] S. Yang, X. Shi, G. Zhang, and C. Lv, “A Dual-Platform Laser Scanner for 3D Reconstruction of Dental Pieces,” *Engineering*, vol. 4, no. 6, pp. 796–805, Dec. 2018, doi: 10.1016/j.eng.2018.10.005.
- [6] P. Kienle *et al.*, “Optical Setup for Error Compensation in a Laser Triangulation System,” *Sensors*, vol. 20, no. 17, p. 4949, Sep. 2020, doi: 10.3390/s20174949.
- [7] A. Donges and R. Noll, *Laser Measurement Technology: Fundamentals and Applications*. Springer, 2014.
- [8] F. J. Brose, J. J. Aguilar, D. Guillomía, and J. Santolaria, “3D Geometrical Inspection of Complex Geometry Parts Using a Novel Laser Triangulation Sensor and a Robot,” *Sensors*, vol. 11, no. 1, pp. 90–110, Dec. 2010, doi: 10.3390/s110100090.
- [9] “Laser and Gaussian Beam Propagation and Transformation,” in *Encyclopedia of Optical and Photonic Engineering, Second Edition*, CRC Press, 2015, pp. 1–15. Accessed: Nov. 11, 2023. [Online]. Available: <http://dx.doi.org/10.1081/e-oe2-120009751>
- [10] H. Yang, W. Tao, Z. Zhang, S. Zhao, X. Yin, and H. Zhao, “Reduction of the Influence of Laser Beam Directional Dithering in a Laser Triangulation Displacement Probe,” *Sensors*, vol. 17, no. 5, p. 1126, May 2017, doi: 10.3390/s17051126.
- [11] S. Ibaraki, Y. Kitagawa, Y. Kimura, and S. Nishikawa, “On the limitation of dual-view triangulation in reducing the measurement error induced by the speckle noise in scanning operations,” *The International Journal of Advanced Manufacturing Technology*, vol. 88, no. 1–4, pp. 731–737, Apr. 2016, doi: 10.1007/s00170-016-8787-x.
- [12] S. Takushima, H. Kawano, H. Nakahara, and T. Kurokawa, “On-machine multi-directional laser displacement sensor using scanning exposure method for high-precision measurement of metal-works,” *Precision Engineering*, vol. 51, pp. 437–444, Jan. 2018, doi: 10.1016/j.precisioneng.2017.09.015.
- [13] T. Mueller, A. Poesch, and E. Reithmeier, “Measurement Uncertainty of Microscopic Laser Triangulation on Technical Surfaces,” *Microscopy and Microanalysis*, vol. 21, no. 6, pp. 1443–1454, Oct. 2015, doi: 10.1017/s1431927615015330.
- [14] R. G. Dorsch, G. Häusler, and J. M. Herrmann, “Laser triangulation: fundamental uncertainty in distance measurement,” *Applied Optics*, vol. 33, no. 7, p. 1306, Mar. 1994, doi: 10.1364/ao.33.001306.

- [15] V. N. Mahajan, *Optical Imaging and Aberrations: Ray geometrical optics*. 2001.
- [16] J. Blanc-Talon, W. Philips, D. Popescu, P. Scheunders, and R. Kleihorst, *Advanced Concepts for Intelligent Vision Systems: 13th International Conference, ACIVS 2011, Ghent, Belgium, August 22-25, 2011, Proceedings*. Springer, 2011, pp. 724–735.
- [17] D. C. Montgomery, *Introduction to Statistical Quality Control*. Wiley, 2008.
- [18] Brigham Young University, “Opticsbook.” <https://optics.byu.edu/docs/opticsbook.pdf> (accessed Nov. 17, 2023).
- [19] “autoVimation ,” *Mounting Kits*. <https://www.autovimation.com/en/mounting-accessories-en/mounting-kits-en> (accessed Nov. 22, 2023).
- [20] “Trailing arm - Weweler-Colaert,” *Colaert*. <https://colcat.weweler.eu/en/products/springs/trailing-arm> (accessed Nov. 27, 2023).
- [21] ISO, “Quality management systems — Requirements, ISO 9001, 2015”.
- [22] P. Poredoš, K. Povsic, B. Novak, and M. Jezeršek, “Three-Dimensional Measurements of Bodies in Motion Based on Multiple- Laser-Plane Triangulation,” *Corporacion Universitaria Remington*, Jan. 01, 2015. [https://www.researchgate.net/publication/281744073\\_Three-Dimensional\\_Measurements\\_of\\_Bodies\\_in\\_Motion\\_Based\\_on\\_Multiple-\\_Laser-Plane\\_Triangulation](https://www.researchgate.net/publication/281744073_Three-Dimensional_Measurements_of_Bodies_in_Motion_Based_on_Multiple-_Laser-Plane_Triangulation)
- [23] “Image Undistortion- MATLAB & Simulink- MathWorks Italia.” <https://it.mathworks.com/help/visionhdl/ug/image-undistort.html> (accessed Nov. 27, 2023).
- [24] Moment, “Superfish Distortion Correction,” *Moment Help Center*. <https://help.shopmoment.com/article/181-superfish-distortion-correction> (accessed Nov. 27, 2023).
- [25] D. Zafra, “Depth of Field in Photography Explained: The Ultimate DOF Guide!,” *Capture the Atlas*, Mar. 08, 2022. <https://capturetheatlas.com/depth-of-field-photography/> (accessed Nov. 27, 2023).
- [26] Rayleigh, “XXXI. Investigations in optics, with special reference to the spectroscope,” *The London, Edinburgh, and Dublin Philosophical Magazine and Journal of Science*, vol. 8, no. 49, pp. 261–274, Oct. 1879, doi: 10.1080/14786447908639684.
- [27] R. I. Hartley and P. Sturm, “Triangulation,” *Computer Vision and Image Understanding*, vol. 68, no. 2, pp. 146–157, Nov. 1997, doi: 10.1006/cviu.1997.0547.
- [28] A. J. P. Theuwissen, “CMOS image sensors: State-of-the-art,” *Solid-State Electronics*, vol. 52, no. 9, pp. 1401–1406, Sep. 2008, doi: 10.1016/j.sse.2008.04.012.
- [29] O. Yadid-Pecht, R. Ginosar, and Y. Shacham-Dimand, “A random access photodiode array for intelligent image capture,” in *17th Convention of Electrical and Electronics Engineers in Israel*. Accessed: Nov. 29, 2023. [Online]. Available: <http://dx.doi.org/10.1109/eeis.1991.217637>
- [30] Z. Wang, Y. Fu, K. Zhong, Y. Li, and W. Bao, “A direct calibration method for line structured light measurement system based on parallel lines,” *Optics Communications*, vol. 508, p. 127699, Apr. 2022, doi: 10.1016/j.optcom.2021.127699.
- [31] J. Landsberg and P. Sands, “Weather and Energy Balance,” in *Physiological Ecology of Forest Production*, Elsevier, 2011, pp. 13–48. Accessed: Dec. 01, 2023. [Online]. Available: <http://dx.doi.org/10.1016/b978-0-12-374460-9.00002-0>
- [32] Kowa, [https://www.kowa-lenses.com/media/pdf/ae/d5/3d/LM12HC\\_03\\_2020.pdf](https://www.kowa-lenses.com/media/pdf/ae/d5/3d/LM12HC_03_2020.pdf)

- [33] JCGM, "Guide to the expression of uncertainty in measurement - JCGM 100:2008 (GUM 1995 with minor corrections - Evaluation of measurement data".
- [34] X. Li, C. Song, S. López, Y. Li, and J. F. López, "Fast computation of bare soil surface roughness on a Fermi GPU," *Computers & Geosciences*, vol. 82, pp. 38–44, Sep. 2015, doi: 10.1016/j.cageo.2015.05.013.